Lehrstuhl für Baumechanik
Technische Universität München

Implementation of a hybrid Trefftz finite element for the analysis of elastodynamic media in the frequency domain

Bc. Michal Šmejkal

Masterarbeit im Studiengang Bauingenieurwesen
Vertiefungsrichtung Baumechanik

Referent	:	Univ.-Prof. Dr.-Ing. Gerhard Müller
Betreuer	:	M.Sc. Mirjam Lainer
Konsultant	:	Prof. Ing. Milan Jirásek, DrSc.
Eingereicht	:	November 7, 2021

Abstract

The thesis develops numerical tools for dynamic analysis of elastic media. Particularly, the hybrid-Trefftz method is applied in order to approximate the solution of the underlying differential equation expressed in the frequency domain. In addition, wave propagation in unbounded media is investigated and the absorbing boundary modelling approach is described in detail. The main purpose of the work was to develop a program enabling such analysis and implement it in MATLAB software. To validate the code, the obtained results are compared to the analytical solutions as well as to the results acquired with the wave based method, for which an already existing code has been provided. Moreover, theoretical aspects of both methods are summarized and compared.

Keywords:

- Hybrid Trefftz method
- Elastodynamics
- Finite element analysis
- Unbounded media
- Absorbing boundary condition

Declaration

Acknowledgements

I would first like to thank my supervisor, Mirjam Lainer, M.Sc., for her helpfulness and guidance during the development of this work. Moreover, I wish to express my gratitude to my advisor, Prof. Ing. Milan Jirásek, DrSc., for valuable advices and insightful comments. In addition, I would also like to thank my parents for great support, helpfulness and encouragement during my studies.

Declaration

I hereby declare that the thesis submitted is my own unaided work. All direct or indirect sources used are acknowledged as references.

Prague, November 7, 2021

Michal Šmejkal

Contents

List of Figures

List of Tables

Symbol Directory

Symbol $\widehat{(\,)}$ denotes a complex conjugate.
Symbol $\dot{(\,)}$ denotes the time derivative.

Greek Letters

γ_{xy}		Shear strain
Γ		Boundary of a body
Γ^e		Element boundary
Γ_a		Absorbing boundary
Γ_a^e		Element absorbing boundary
Γ_u		Dirichlet boundary
Γ_u^e		Element Dirichlet boundary
Γ_σ		Neumann boundary
Γ_σ^e		Element Neumann boundary
Γ_m		Mixed boundary
Γ_m^e		Element mixed boundary
Γ_I		Inter-element boundary
$\boldsymbol{\nabla}$		Gradient
$\widetilde{\boldsymbol{\nabla}}$		Curl operator
∇^2		Laplace operator
$\boldsymbol{\varepsilon}$		Strain vector
$\boldsymbol{\varepsilon_0}$		Vector of particular strain solutions
ε_x		Normal strain component in x direction
ε_y		Normal strain component in y direction
η		Loss factor
θ		Angular coordinate
λ	$\frac{\mathrm{N}}{\mathrm{m}^2}$	First Lamé coefficient
μ	$\frac{\mathrm{N}}{\mathrm{m}^2}$	Second Lamé coefficient
ν		Poisson's ratio
ξ		Normalized side coordinate
ω	$\frac{2\pi}{\mathrm{s}}$	Circular frequency
ρ	$\frac{\mathrm{kg}}{\mathrm{m}^3}$	Mass density
$\boldsymbol{\sigma}$		Stress vector
σ_x	$\frac{\mathrm{N}}{\mathrm{m}^2}$	Normal stress component in x direction

σ_y	$\frac{\mathrm{N}}{\mathrm{m}^2}$	Normal stress component in y direction
τ_{xy}	$\frac{\mathrm{N}}{\mathrm{m}^2}$	Shear stress
Φ_p		Dilatational potential
Φ_s		Shear potential

Latin Letters

$\boldsymbol{b}$		Vector of body forces	
b_x	$\frac{\mathrm{N}}{\mathrm{m}^3}$	Body force component in x direction	
b_y	$\frac{\mathrm{N}}{\mathrm{m}^3}$	Body force component in y direction	
c_p	$\frac{\mathrm{m}}{\mathrm{s}}$	Pressure wave velocity	$\sqrt{\frac{\lambda+2\mu}{\rho}}$
c_s	$\frac{\mathrm{m}}{\mathrm{s}}$	Shear wave velocity	$\sqrt{\frac{\mu}{\rho}}$
$\boldsymbol{C}$		Matrix mapping the displacements and tractions evaluated at the boundary in infinity	
$\boldsymbol{\mathcal{D}}$		Differential operator matrix	
$\tilde{E}$	$\frac{\mathrm{N}}{\mathrm{m}^2}$	Young modulus	
$\tilde{E}_s$	$\frac{\mathrm{N}}{\mathrm{m}^2}$	Storage modulus	
E		Comparison measure	
E_{FE}		Approximated comparison measure	
$\boldsymbol{E}$		Matrix of strain basis functions	
f	$\frac{1}{\mathrm{s}}$	Frequency	$f = \frac{\omega}{2\pi}$
$H_n^{(1)}$		Hankel function of the first kind and order n	
$H_n^{(2)}$		Hankel function of the second kind and order n	
i		Imaginary unit	
J		Jacobian	
J_n		Bessel function of the first kind and order n	
$\boldsymbol{k}$		Material matrix	
k_p	$\frac{1}{\mathrm{m}}$	Pressure wave number	$\frac{\omega}{c_p}$
k_s	$\frac{1}{\mathrm{m}}$	Shear wave number	$\frac{\omega}{c_s}$
$\mathcal{L}_a$		Differential operator transforming potentials Φ_p and Φ_s to field a	
M		Maximum order of a polynomial included in the boundary traction approximation basis $\boldsymbol{Z}$, order of the traction approximation basis	
n_x		Unit normal component in x direction	
n_y		Unit normal component in y direction	
n_r		Unit normal component in radial direction	
n_θ		Unit normal component in angular direction	
$\boldsymbol{N}$		Matrix of unit normals	

N		Maximum order of the Bessel solution function W included in the displacement approximation basis $\boldsymbol{U}$, order of the displacement approximation basis
$\boldsymbol{p_x}$		Vector of unknown boundary traction coefficients related to the traction component t_x
$\boldsymbol{p_y}$		Vector of unknown boundary traction coefficients related to the traction component t_y
$\boldsymbol{p}$		Vector of unknown boundary traction coefficients
$\boldsymbol{p_a}$		Vector of unknown absorbing boundary traction coefficients
$\boldsymbol{t}$		Boundary traction vector
$\boldsymbol{t_\Gamma}$		Vector of prescribed traction components
r	m	Radial coordinate
$\boldsymbol{S}$		Scaling matrix
t	s	Time
t_x	$\frac{\mathrm{N}}{\mathrm{m}^2}$	Traction component in x direction
t_y	$\frac{\mathrm{N}}{\mathrm{m}^2}$	Traction component in y direction
t_n	$\frac{\mathrm{N}}{\mathrm{m}^2}$	Traction component in normal direction
t_t	$\frac{\mathrm{N}}{\mathrm{m}^2}$	Traction component in tangential direction
$t_{\Gamma,x}$	$\frac{\mathrm{N}}{\mathrm{m}^2}$	Prescribed traction component in x direction
$t_{\Gamma,y}$	$\frac{\mathrm{N}}{\mathrm{m}^2}$	Prescribed traction component in y direction
$t_{\Gamma,n}$	$\frac{\mathrm{N}}{\mathrm{m}^2}$	Prescribed traction component in normal direction
$t_{\Gamma,t}$	$\frac{\mathrm{N}}{\mathrm{m}^2}$	Prescribed traction component in tangential direction
T	s	Period
$\boldsymbol{T}$		Transformation matrix
$\boldsymbol{T}_\varepsilon$		Strain transformation matrix
$\boldsymbol{u}$		Displacement vector
$\boldsymbol{u_0}$		Vector of particular displacement solutions
$\tilde{\boldsymbol{u}}_\mathbf{0}$		Initial displacement vector
$\boldsymbol{u_\Gamma}$		Vector of prescribed displacement components
u	m	Displacement component in x direction
u_n	m	Displacement component in normal direction
u_t	m	Displacement component in tangential direction
u_Γ	m	Prescribed displacement component in x direction
$u_{\Gamma,n}$	m	Prescribed displacement component in normal direction

$u_{\Gamma,t}$	m	Prescribed displacement component in tangential direction
$u_{0,x}$	m	x component of the vector of particular displacement solution $\boldsymbol{u_0}$
$\boldsymbol{U}$		Matrix of displacement basis functions
$\boldsymbol{U_x}$		Vector of displacement basis functions approximating the component in x direction
$\boldsymbol{U_y}$		Vector of displacement basis functions approximating the component in y direction
$\boldsymbol{U}^{r,\theta}$		Matrix of basis functions approximating displacements in radial and angular directions
$\tilde{\boldsymbol{v}}_{\boldsymbol{0}}$		Initial velocity vector
v	m	Displacement component in y direction
v_Γ	m	Prescribed displacement component in y direction
V		Domain of a body
V_{ext}		External part of infinite domain
V^e		Element domain
W		Solution function of the Bessel equation
$\boldsymbol{X}$		Vector of unknown displacement coefficients
Y_n		Bessel function of the second kind and order n
$\boldsymbol{Z}$		Matrix gathering boundary traction approximation basis
$\boldsymbol{Z_a}$		Matrix gathering absorbing boundary traction approximation basis
$\boldsymbol{Z_v}$		Vector of basis functions approximating single traction component
Z		Boundary approximation basis function

1 Introduction

The problem of dynamically loaded media is a frequently investigated process, especially in the fields of civil engineering, earthquake engineering and geotechnics. Under certain simplifications, such physical behaviour can be described by a set of coupled partial differential equations expressed in terms of unknown displacement field depending on the time and space coordinates. Unfortunately, for most of the practical cases this mathematical problem cannot be solved analytically and therefore numerical methods need to be applied to approximate the solution.

As the set of governing equations contains differentiation with respect to time and space coordinates, both dependencies need to be treated by a suitable method. By transferring all the field equations into the frequency domain, the original problem in time and space is divided into a number of subproblems, which are however formulated in terms of space coordinates only. The associated space solution is subsequently approximated. Various methods were developed to tackle such task, a widely used option is e.g. the finite element method (FEM). However, for higher excitation frequencies a fine domain discretization is required, which results in large equation systems and computationally expensive simulation. Alternative options for such analysis are Trefftz methods, which use special shape functions for the approximation of the unknown fields. The individual basis functions are required to satisfy the governing equation, therefore inside the domain the approximated field is implicitly the solution of the differential equation. However, the basis components may violate the prescribed boundary conditions and hence they need to be combined in order to decrease the resulting error on the boundary. In the thesis the so called hybrid-Trefftz method is investigated, in which the boundary traction field is additionally approximated on the boundary of the individual elements. The purpose of such field is to impose the boundary and the inter-element continuity conditions.

The main objective of this work is to implement the hybrid-Trefftz method for numerical analysis of 2D elastodynamic media. MATLAB software is used as the programming language for the code development. Besides the standard boundary conditions, also a modelling approach for the analysis of unbounded media is incorporated in the program. To validate the implemented method, the obtained results are compared to both analytical solutions as well as to the results acquired with the wave based method, for which an already existing code has been provided. Moreover, theoretical aspects of both hybrid-Trefftz and wave based methods are summarized and compared.

The thesis is structured into six chapters. The first one is dedicated to introduction of the analysed problem and to derivation of the governing differential equation. In addition, the transfer of all the fields and equations into the frequency domain is described. The resulting spectral representation forms the base for the derivation of the hybrid-Trefftz method, which is described in detail in the second chapter. Before the finite element system of equations is generated, the

solution procedure of the spectral Lamé equation is outlined, so that the basis functions satisfying the governing equation are formulated. In the next chapter, wave propagation in infinite media is studied, particularly, the absorbing boundary modelling approach is derived and described in detail. The last theoretical chapter is devoted to a brief introduction of the wave based method and to its comparison to the hybrid-Trefftz method. In the fifth chapter the implementation process of the whole program is outlined and in-depth description of all the individual subroutines is provided. In the last chapter the results of three numerical examples are discussed; for the first two the analytical solutions are available and for the third one the wave based method results are considered as the reference. Convergence process of both p- and h-refinement strategies is studied and performance of the absorbing boundary condition is investigated.

2 Problem Description

The aim of this chapter is to introduce the problem of interest and provide a theoretical background for the upcoming sections.

As was indicated in the introduction, the objective of this thesis is the numerical analysis of loaded elastodynamic media. To enable a reasonable description of such problem, certain assumptions regarding the material, loading and geometry need to be adopted, which is discussed in the first sections. Afterwards, the governing differential equation is derived. It turns out that not only derivatives with respect to space coordinates but as well with respect to time appear, which makes the solution procedure more complex. The so called frequency domain analysis method is applied, which allows to transfer the original problem in space and time into a number of problems dependent on space coordinates only. The solution procedure of the resulting system of partial differential equations in space is the main purpose of this work and a single chapter is devoted to it.

2.1 Assumptions and Hypotheses

The analysis of dynamically loaded medium is a complex problem. The following assumptions are considered through this thesis so that the solution of such task is simplified:

- The matter inside the body is continuously distributed with no empty spaces, hence the structure may be analysed as a continuum.
- The material is isotropic. This statement indicates that the material response and its properties are identical in all directions.
- The relation between the stresses and strains is assumed to be linear.
- The strains and displacements are assumed to be small. This implies the deformation caused by the loading has a negligible effect on the equilibrium of forces, which can therefore be evaluated on the undeformed structure. Such assumption is referred to as geometrical linearity.
- The loading of the structure is assumed to be a periodic function in time. Some comments regarding arbitrary transient functions are placed in the end of the chapter.

2.2 Domain and Geometry

To make the modelling procedure and the visualization of the results more convenient, certain assumptions regarding the geometry are considered. It is assumed that a 2D shape placed in xy-plane

is extruded in the direction of z-axis, in which the dimension of the object tends to infinity. Furthermore, the material properties, prescribed boundary conditions and the loading remain constant in this longitudinal direction. In addition, both displacement and traction boundary conditions have zero component in the z-direction. Under such presumptions the body can be modelled as a 2D domain.

In fig. 2.1 a general scheme of a possible structure of interest is depicted. The domain is represented by symbol V and Γ stands for the boundary of such body. It can be partitioned into two nonoverlapping complementary sections, Γ_u and Γ_σ, which are called Dirichlet and Neumann boundaries respectively. Boundary displacements are prescribed on the former one while boundary tractions are given on the latter one.

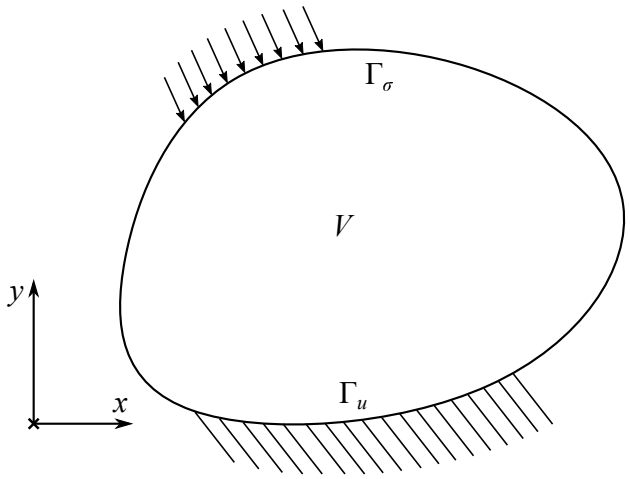

Figure 2.1: Domain and boundary

2.3 Governing Equation in Time Domain

The behaviour of a loaded structure can be described using three main sets of equations, which are equilibrium equations, kinematic equations and material law. These need to be supplied with boundary and initial conditions so that the problem is well defined. Afterwards, the relations are combined to form a governing system of equations.

All the relations are expressed using a matrix notation and a Cartesian reference frame is adopted. The mentioned equations and formulas can be found in [Poruchikov 2012] and [Gonzalez and Stuart 2008].

2.3.1 Stress and Strain Measure

The assumption of small strains and displacements was briefly discussed in section 2.1. As a result of geometrical linearity, small strain tensor is adopted as the strain measure. Using Voigt notation, it can be expressed as a strain vector $\boldsymbol{\varepsilon}(x,y,t)$ with six independent components. For the 2D case

of interest, the number of components reduces to three and are ordered as

$$\boldsymbol{\varepsilon} = \begin{bmatrix} \varepsilon_x & \varepsilon_y & \gamma_{xy} \end{bmatrix}^T, \tag{2.1}$$

where $\varepsilon_x(x,y,t)$ and $\varepsilon_y(x,y,t)$ are the normal strain components while $\gamma_{xy}(x,y,t)$ is the shear strain component.

As the stress and strain tensors need to form a work conjugate pair, engineering stress tensor is chosen as the valid stress measure. Similarly to the strain counterpart, its components can be restructured into the engineering stress vector $\boldsymbol{\sigma}(x,y,t)$. For the 2D case the vector is expressed as

$$\boldsymbol{\sigma} = \begin{bmatrix} \sigma_x & \sigma_y & \tau_{xy} \end{bmatrix}^T, \tag{2.2}$$

with $\sigma_x(x,y,t)$ and $\sigma_y(x,y,t)$ being the normal stress components and $\tau_{xy}(x,y,t)$ the shear stress component.

2.3.2 Equilibrium Equations

The equilibrium equations describe an equilibrium of forces on an infinitesimal volume and can be derived using the law of conservation of momentum. Since the loading and therefore all the field quantities may vary in time, also inertia forces need to be included. In a matrix notation, the relations can be expressed as

$$\boldsymbol{\mathcal{D}\sigma} + \boldsymbol{b} = \rho\ddot{\boldsymbol{u}} \text{ in } V, \tag{2.3}$$

where $\boldsymbol{u}(x,y,t)$ is a vector collecting displacement components, vector $\boldsymbol{b}(x,y,t)$ contains body forces and $\rho(x,y)$ is the mass density. Matrix $\boldsymbol{\mathcal{D}}$ is a differential operator matrix. The symbol $\ddot{(\cdot)}$ represents the second time derivative.

For the particular case of 2D elastodynamic continuum the vectors and matrices are formed as

$$\boldsymbol{u} = \begin{bmatrix} u & v \end{bmatrix}^T, \ \boldsymbol{b} = \begin{bmatrix} b_x & b_y \end{bmatrix}^T, \ \boldsymbol{\mathcal{D}} = \begin{bmatrix} \dfrac{\partial}{\partial x} & 0 & \dfrac{\partial}{\partial y} \\ 0 & \dfrac{\partial}{\partial y} & \dfrac{\partial}{\partial x} \end{bmatrix}, \tag{2.4}$$

where $u(x,y,t)$ and $v(x,y,t)$ are the displacement components in x and y direction and $b_x(x,y,t)$ and $b_y(x,y,t)$ are the individual body forces components.

2.3.3 Kinematic Equations

Kinematic equations describe the relation between displacements and strains. The small strain vector $\boldsymbol{\varepsilon}$ can be expressed in terms of displacements as

$$\boldsymbol{\varepsilon} = \boldsymbol{\mathcal{D}}^* \boldsymbol{u} \text{ in } V. \tag{2.5}$$

Matrix $\boldsymbol{\mathcal{D}}^*$ is the differential kinematic operator which is the adjoint of $\boldsymbol{\mathcal{D}}$. Such property is a consequence of the geometrically linearized theory. As a Cartesian reference frame is considered, $\boldsymbol{\mathcal{D}}^*$ can be replaced by $\boldsymbol{\mathcal{D}}^T$.

2.3.4 Material Law

The material equations express the relation between the strains and stresses. For simplicity, the linear elastic material law

$$\boldsymbol{\sigma} = \boldsymbol{k}\boldsymbol{\varepsilon} \text{ in } V \tag{2.6}$$

is considered, where $\boldsymbol{k}(x,y)$ denotes the material matrix. As the material is considered to by isotropic, only two constants are necessary to form the matrix $\boldsymbol{k}$. These can either be the Lamé coefficients $\lambda(x,y)$ and $\mu(x,y)$ or the Young modulus $\tilde{E}(x,y)$ and Poisson's ratio $\nu(x,y)$. The relation between both possible descriptions reads [Malvern 1969]

$$\lambda = \frac{\nu\tilde{E}}{(1+\nu)(1-2\nu)}, \tag{2.7}$$

$$\mu = \frac{\tilde{E}}{2(1+\nu)}. \tag{2.8}$$

When the 2D case is of interest, one has to distinguish between plane strain and plane stress case. The assumptions regarding the geometry were described in section 2.1. Such situation indicates that the displacement as well as the normal strain in z-direction are zero and therefore plane strain case is of interest. The material matrix has then the form [Bauchau and Craig 2009]

$$\boldsymbol{k} = \begin{bmatrix} \lambda+2\mu & \lambda & 0 \\ \lambda & \lambda+2\mu & 0 \\ 0 & 0 & \mu \end{bmatrix}. \tag{2.9}$$

In reality, the applicability of linear elasticity is strongly limited and more complex theories need to be considered in order to approximate the real behaviour more accurately. Some comments regarding the incorporation of damping into the formulation are mentioned in section 2.4.4.

2.3.5 Boundary Conditions

To pose a valid problem, boundary conditions must be introduced. The first type of boundary condition are prescribed displacements on the Dirichlet part of boundary Γ_u,

$$\boldsymbol{u} = \boldsymbol{u}_{\boldsymbol{\Gamma}} \text{ on } \Gamma_u, \tag{2.10}$$

where $\boldsymbol{u}_{\boldsymbol{\Gamma}}(x,y,t) = \begin{bmatrix} u_\Gamma & v_\Gamma \end{bmatrix}^T$ denotes the vector of prescribed displacement components $u_\Gamma(x,y,t)$ and $v_\Gamma(x,y,t)$ in Cartesian directions. This type of boundary condition is also called Dirichlet boundary condition.

The second type of boundary condition, also called Neumann boundary condition, is in terms of prescribed tractions on a portion of boundary Γ_σ. Symbolically it can be expressed as

$$\boldsymbol{t} = \boldsymbol{t_\Gamma} \text{ on } \Gamma_\sigma, \tag{2.11}$$

where

$$\boldsymbol{t_\Gamma}(x,y,t) = \begin{bmatrix} t_{\Gamma,x} & t_{\Gamma,y} \end{bmatrix}^T \tag{2.12}$$

stands for vector of prescribed traction components $t_{\Gamma,x}(x,y,t)$ and $t_{\Gamma,y}(x,y,t)$ in the individual directions. The boundary traction vector $\boldsymbol{t}(x,y,t) = \begin{bmatrix} t_x & t_y \end{bmatrix}^T$ collecting traction components $t_x(x,y,t)$ and $t_y(x,y,t)$ is calculated based on the equilibrium at a boundary Γ as

$$\boldsymbol{t} = \boldsymbol{N}\boldsymbol{\sigma} \text{ on } \Gamma. \tag{2.13}$$

Matrix

$$\boldsymbol{N} = \begin{bmatrix} n_x & 0 & n_y \\ 0 & n_y & n_x \end{bmatrix} \tag{2.14}$$

collects components of the outward normal at the boundary.

2.3.6 Initial Conditions

For a general type of excitation, it is necessary to provide information regarding the initial state of the structure, such as initial displacement shape $\tilde{\boldsymbol{u}}_\mathbf{0}(x,y)$ and initial velocity state $\tilde{\boldsymbol{v}}_\mathbf{0}(x,y)$ in the beginning of an observation when $t = 0$. Such condition can be formulated as

$$\begin{aligned} \boldsymbol{u} &= \tilde{\boldsymbol{u}}_\mathbf{0} \text{ at } t = 0, \\ \dot{\boldsymbol{u}} &= \tilde{\boldsymbol{v}}_\mathbf{0} \text{ at } t = 0, \end{aligned} \tag{2.15}$$

where symbol $\dot{(\cdot)}$ denotes the time derivative.

However, it was mentioned in section 2.1 that the loading is assumed to be a periodic function in time. Due to the damping of the structure, which always occurs in reality, the oscillations caused by the initial conditions reduce significantly with increasing time. After a certain period they will have negligible effect and only the oscillations caused by the periodic loading will play a role. Therefore, the free vibration part of the solution is neglected and only the steady state solution is of interest.

2.3.7 Governing Differential Equation

To form the governing differential equation, previously mentioned sets of equations are combined together. In particular, kinematic equations (2.5) are substituted into the material law (2.6), which

is then inserted into equilibrium equations (2.3). The resulting equation is then expressed as

$$\boldsymbol{\mathcal{D}k\mathcal{D}}^{*}\boldsymbol{u} - \rho\ddot{\boldsymbol{u}} + \boldsymbol{b} = \boldsymbol{0} \text{ in } V. \tag{2.16}$$

Substituting all the already defined matrices and vectors into eq. (2.16) and assuming the Lamé parameters are constant in the domain V, one obtains

$$(\lambda + \mu)\boldsymbol{\nabla}\boldsymbol{\nabla}^{T}\boldsymbol{u} + \mu\nabla^{2}\boldsymbol{u} - \rho\ddot{\boldsymbol{u}} + \boldsymbol{b} = \boldsymbol{0}, \tag{2.17}$$

where $\boldsymbol{\nabla} = [\partial/\partial x \ \partial/\partial y]^{T}$ is the gradient and $\nabla^{2} = \boldsymbol{\nabla}^{T}\boldsymbol{\nabla} = \partial^{2}/\partial x^{2} + \partial^{2}/\partial y^{2}$ is the Laplace operator. Eq. (2.16) expresses a system of two second order partial differential equations in time and space and is referred to as the Lamé equation.

2.4 Frequency Domain Analysis

In the previous section, the governing system of partial differential equations was derived. As the problem of interest is of dynamic nature, not only derivatives with respect to space coordinates but also with respect to time coordinate appear, which makes the solution procedure even more complex. Various numerical techniques and methods to deal with the time dependency are available, e.g. modal analysis, explicit and implicit time integration methods or frequency domain analysis. Depending on the analysed problem and type of excitation, some methods are more suitable than others. In the scope of this thesis, the frequency domain analysis method will be adopted.

An essence of frequency domain analysis [Clough and Penzien 2003] is to transfer the problem depending on space and time coordinates into a number of sub problems which however depend on the space coordinates only. A mathematical procedure enabling such decomposition is named Fourier series expansion. With its help the governing differential equation as well as all the field equations and boundary conditions can be transformed into the frequency domain. The resulting formulation becomes a starting point for the space discretization procedure.

2.4.1 Fourier Series Expansion

Any periodic function $f(t)$ with period T can be decomposed into a sum of harmonic functions with discrete frequencies, such decomposition is referred to as Fourier series. Using a complex representation, it is expressed as [Serov et al 2017]

$$f(t) = \sum_{k=-\infty}^{\infty} c_k \exp(i\omega_k t), \tag{2.18}$$

where $\omega_k = k\omega_1$ are the discrete circular frequencies and $\omega_1 = 2\pi/T$ is the circular frequency of function $f(t)$. The coefficients c_k can be calculated as

$$c_k = \frac{1}{T}\int_0^T f(t)\exp(-i\omega_k t)\mathrm{d}t. \tag{2.19}$$

2.4.2 Transfer to Frequency Domain

An excitation of a structure is driven by the prescribed boundary tractions $\boldsymbol{t}_{\boldsymbol{\Gamma}}(x,y,t)$, boundary displacements $\boldsymbol{u}_{\boldsymbol{\Gamma}}(x,y,t)$ and body forces $\boldsymbol{b}(x,y,t)$, which are all for simplicity assumed to be periodic functions in time. Due to this property, it is possible to perform a Fourier series expansion of the related fields in a similar way as was described in eq. (2.18). However, in practice it is not feasible to keep the infinite number of terms of the expansion, therefore only a finite number of terms $2K-1$ is included in the series. This results in an approximation

$$\boldsymbol{t}_{\boldsymbol{\Gamma}}(x,y,t) \approx \sum_{k=1-K}^{K-1} \boldsymbol{t}_{\boldsymbol{\Gamma},\boldsymbol{k}}(x,y)\exp(i\omega_k t), \tag{2.20}$$

$$\boldsymbol{u}_{\boldsymbol{\Gamma}}(x,y,t) \approx \sum_{k=1-K}^{K-1} \boldsymbol{u}_{\boldsymbol{\Gamma},\boldsymbol{k}}(x,y)\exp(i\omega_k t), \tag{2.21}$$

$$\boldsymbol{b}(x,y,t) \approx \sum_{k=1-K}^{K-1} \boldsymbol{b}_{\boldsymbol{k}}(x,y)\exp(i\omega_k t), \tag{2.22}$$

where the coefficients $\boldsymbol{t}_{\boldsymbol{\Gamma},\boldsymbol{k}}$, $\boldsymbol{u}_{\boldsymbol{\Gamma},\boldsymbol{k}}$ and $\boldsymbol{b}_{\boldsymbol{k}}$ are computed based on eq. (2.19) as

$$\boldsymbol{t}_{\boldsymbol{\Gamma},\boldsymbol{k}}(x,y) = \frac{1}{T}\int_0^T \boldsymbol{t}_{\boldsymbol{\Gamma}}(x,y,t)\exp(-i\omega_k t)\mathrm{d}t, \tag{2.23}$$

$$\boldsymbol{u}_{\boldsymbol{\Gamma},\boldsymbol{k}}(x,y) = \frac{1}{T}\int_0^T \boldsymbol{u}_{\boldsymbol{\Gamma}}(x,y,t)\exp(-i\omega_k t)\mathrm{d}t, \tag{2.24}$$

$$\boldsymbol{b}_{\boldsymbol{k}}(x,y) = \frac{1}{T}\int_0^T \boldsymbol{b}(x,y,t)\exp(-i\omega_k t)\mathrm{d}t. \tag{2.25}$$

Note that these coefficients are known, since the prescribed boundary values and body forces are given.

As the loading and boundary conditions are periodic functions in time, one can assume that also the response is periodic. This allows to perform a Fourier expansion of the unknown displacement, traction, stress and strain fields, expressed as

$$\boldsymbol{u}(x,y,t) \approx \sum_{k=1-K}^{K-1} \boldsymbol{u}_{\boldsymbol{k}}(x,y)\exp(i\omega_k t), \tag{2.26}$$

$$\boldsymbol{t}(x,y,t) \approx \sum_{k=1-K}^{K-1} \boldsymbol{t}_{\boldsymbol{k}}(x,y)\exp(i\omega_k t), \tag{2.27}$$

$$\boldsymbol{\sigma}(x,y,t) \approx \sum_{k=1-K}^{K-1} \boldsymbol{\sigma}_{\boldsymbol{k}}(x,y)\exp(i\omega_k t), \tag{2.28}$$

$$\boldsymbol{\varepsilon}(x,y,t) \approx \sum_{k=1-K}^{K-1} \boldsymbol{\varepsilon}_{\boldsymbol{k}}(x,y)\exp(i\omega_k t). \tag{2.29}$$

Coefficients $\boldsymbol{u}_{\boldsymbol{k}}(x,y)$, $\boldsymbol{t}_{\boldsymbol{k}}(x,y)$, $\boldsymbol{\sigma}_{\boldsymbol{k}}(x,y)$ and $\boldsymbol{\varepsilon}_{\boldsymbol{k}}(x,y)$ are however unknown.

Due to the linearity of the problem, principle of superposition can be applied. This allows to

calculate the response for each term in the sum separately and superpose the contribution of each frequency afterwards. Substituting $\boldsymbol{u} = \boldsymbol{u_k}(x,y)\exp(i\omega_k t)$ and $\boldsymbol{b} = \boldsymbol{b_k}(x,y)\exp(i\omega_k t)$ into eq. (2.16) and cancelling the exponential terms yields

$$\boldsymbol{\mathcal{D}k\mathcal{D}^*u_k} + \omega_k^2\rho\boldsymbol{u_k} + \boldsymbol{b_k} = \boldsymbol{0} \text{ for } k = \{1-K,2-K,\ldots,K-1\}. \tag{2.30}$$

Inserting the particular definitions of the matrices $\boldsymbol{\mathcal{D}}$ and $\boldsymbol{k}$, the previous equation can be reformulated

$$(\lambda+\mu)\boldsymbol{\nabla\nabla}^T\boldsymbol{u_k} + \mu\nabla^2\boldsymbol{u_k} + \omega_k^2\rho\boldsymbol{u_k} + \boldsymbol{b_k} = \boldsymbol{0} \text{ for } k = \{1-K,2-K,\ldots,K-1\}. \tag{2.31}$$

Eq. (2.31) is the governing differential equation of the system in the frequency domain, also named spectral form of Lamé equation. For each k it represents a system of two coupled partial differential equations depending on the space coordinates only.

Similarly, also equilibrium, kinematic and constitutive equations as well as the boundary conditions can be expressed for a single harmonic excitation as

$$\boldsymbol{\mathcal{D}\sigma_k} + \omega_k^2\rho\boldsymbol{u_k} + \boldsymbol{b_k} = \boldsymbol{0} \text{ in } V, \tag{2.32}$$

$$\boldsymbol{\varepsilon_k} = \boldsymbol{\mathcal{D}^*u_k} \text{ in } V, \tag{2.33}$$

$$\boldsymbol{\sigma_k} = \boldsymbol{k\varepsilon_k} \text{ in } V, \tag{2.34}$$

$$\boldsymbol{t_k} = \boldsymbol{N\sigma_k} \text{ on } \Gamma, \tag{2.35}$$

$$\boldsymbol{u_k} = \boldsymbol{u_{\Gamma,k}} \text{ on } \Gamma_u, \tag{2.36}$$

$$\boldsymbol{t_k} = \boldsymbol{t_{\Gamma,k}} \text{ on } \Gamma_\sigma. \tag{2.37}$$

By the previously described procedure, a periodic elastodynamic problem can be decomposed into $2K-1$ uncoupled sets of partial differential equations (2.30) with dependency on the space coordinates only. After the solution is obtained for each of $2K-1$ circular frequencies ω_k, the final response can be calculated based on eqs. (2.26) to (2.29). The solution procedure of eq. (2.30) is the main objective of this thesis and will be described in detail in chapter 3. For clarity, the subscript k in eqs. (2.30) to (2.37) is omitted in the derivations presented in the subsequent chapters, however, the individual symbols still denote the spectral representation of the related fields.

2.4.3 Arbitrary Excitation

So far the transformation of the equations into the frequency domain was discussed for periodic functions in time. When an arbitrary excitation is to be analysed, the previously mentioned procedure needs to be modified. It is no longer possible to express a function $f(t)$ in eq. (2.18) as a series of harmonic oscillations with discrete circular frequencies, however, the frequency spectrum becomes continuous in such case. To perform the transfer of the field variables to the frequency domain, the Fourier transformation [Serov et al 2017] needs to be applied. Similarly, to reconstruct the results in the time domain, the inverse Fourier transformation is used. Both of these procedures

require solution of an integral which for most of the practical cases cannot be computed analytically. Therefore, a numerical procedure named discrete Fourier transform was invented to approximate the Fourier transform and the inverse Fourier transform. In the end, a finite number of equations of similar form as eq. (2.30) is obtained. However, when discrete Fourier transform is used, certain numerical issues, such as leakage, can occur, which one has to be aware of. As this goes beyond the scope of this thesis, more detailed explanation is skipped.

2.4.4 Damping

Until now the relation between the stresses and strains was assumed to be linear elastic and in the frequency domain it is described by eq. (2.34). Since the material matrix $\boldsymbol{k}$ contains real constants, both stresses and strains oscillate in phase. However, in real situations this is usually not the case and a phase shift between the stress and strain fields can be observed. This is a consequence of the fact, that during the loading process, a portion of the mechanical energy is converted into thermal energy and hence dissipated, which always occurs in reality.

In the scope of the frequency domain analysis, such behaviour can be modelled by assuming the material constants contained in the material matrix $\boldsymbol{k}$ are complex numbers. The original definitions (2.9), (2.7) and (2.8) of the material matrix and the Lamé coefficients remain valid, only the Young modulus $\tilde{E}$ is considered to be complex value defined as

$$\tilde{E} = \tilde{E}_s(1 + i\,\mathrm{sgn}(\omega)\eta), \tag{2.38}$$

where η denotes the loss factor and $\tilde{E}_s$ stands for the so called storage modulus [Meyers and Chawla 2008], which represents the real part of the Young modulus.

3 Hybrid-Trefftz Method

In the previous chapter the elastodynamic problem was introduced and the governing differential equation in the frequency domain (2.30) was derived. As was already mentioned, eq. (2.30) is a set of coupled partial differential equations depending on space coordinates only. For general boundary conditions it is not possible to solve the system analytically and therefore numerical methods need to be applied instead. This chapter discusses how an approximation of the solution of such equation is obtained.

There is a wide range of numerical techniques designed to estimate the solution of such problem, e.g. finite element method, boundary element method or a family of Trefftz methods. The main focus of this thesis is placed on the so called hybrid-Trefftz method, which offers some significant advantages compared to the standard FEM.

Similarly to FEM, also in the case of Trefftz methods the domain is discretized into a number of finite elements, where a certain field is approximated by shape functions multiplied by unknown coefficients. In standard FEM, these shape functions are polynomials. On the other hand, in the case of Trefftz methods, the basis functions are restricted to satisfy the homogeneous part of the governing differential equation. This requirement is also called the Trefftz constraint. As will be discussed later, it is possible to obtain an infinite series of functions which fulfil such constraint, but they violate the prescribed boundary conditions and therefore cannot directly be considered as a solution of the whole problem. However, since the functions are linearly independent, they form a complete basis. This implies that under certain restrictions, any function can be represented as a linear combination of these basis functions and since they all satisfy the homogeneous differential equation, also the linear combination will have this property. The idea of Trefftz methods is to combine a finite number of such basis functions so that the boundary values of the resulting function get closer to the prescribed boundary conditions.

The adjective hybrid indicates that more than one field is approximated simultaneously and independently. There are various options regarding the choice of approximated fields. In the scope of this thesis, the displacement field is approximated in the domain and the boundary traction field is approximated on the Dirichlet boundary. In literature, when an element is formulated using such approach, it is referred to as a displacement element. An alternative would be a stress element, for which the stress field is approximated in the domain and displacements are approximated on the boundary. However, only the former option is considered in this work. The purpose of the boundary field approximation is to enforce the boundary conditions and the continuity between adjacent elements.

The idea of restricting the basis functions to satisfy the governing differential equations was firstly proposed in [Trefftz 1926] as an alternative to the Rayleigh-Ritz method. A formulation of

general Trefftz elements was then reported in [Jirousek 1978], where four possibilities regarding the enforcement of the inter-element continuity between hybrid-Trefftz elements were presented. Mathematical fundamentals related to the construction of the complete bases were formulated by I. Herrera and published in e.g. [Herrera 1980], [Gourgeon and Herrera 1981] and [Herrera and Gourgeon 1982]. Subsequently, the method was applied to various engineering problems, such as bending of plates, 3D solid mechanics, potential problems or heat conduction problems. An overview of the individual formulations can be found e.g. in [Qin 2005]. Application of hybrid-Trefftz method to analysis of elastodynamic media was mainly studied by the group of J. A. T. Freitas. A formulation of the displacement element is presented e.g. in [Freitas 1997] or [Cismaşiu and Freitast 1998]. The approach is then extended for analysis of unbounded media in [Cismaşiu 2000], [Freitas and Cismaşiu 2003] and [Moldovan and Freitas 2006]. Furthermore, in [Moldovan 2008] a propagation in saturated porous media for bounded and unbounded domains in analysed using the hybrid-Trefftz models.

It is important to note that the concept of nodal interpolation known from FEM is completely omitted in subsequent derivations. The bases used to approximate both displacement field in the domain and the traction field on the boundary are hierarchical and the coefficients correspond no longer to nodal values but are rather called generalized quantities.

The chapter is structured in the following way. Firstly, a discretization of the complete domain is introduced. Afterwards, an approximation of the domain displacement field is presented and the basis is derived. This procedure involves a solution of the spectral Lamé equation. Subsequently, the boundary traction approximation is mentioned and the finite element governing system of equations is derived. The equilibrium equations, Dirichlet boundary condition and displacement inter-element continuity conditions are enforced in a weak sense using the Galerkin weighted residual method. On the other hand, the kinematic equations, material equations and traction boundary condition are implicitly satisfied. At the end of the chapter a mixed boundary condition is discussed.

Equations (2.30) to (2.37) form a theoretical basis for the subsequent derivations. For clarity the subscript k will be omitted.

3.1 Finite Element Discretization

The complete domain V is discretized into finite elements with domain V^e and boundary Γ^e as is illustrated in fig. 3.1. The element boundary is split into nonoverlapping parts, Γ_u^e and Γ_σ^e, which are the Dirichlet and Neumann boundaries respectively.

It was mentioned in the introduction of the chapter that the approximated fields are the displacement field in the element domain and the boundary tractions on the Dirichlet boundary. To be more precise, the boundary tractions need to be approximated also on the part of the boundary shared by neighbouring elements. This is necessary for the enforcement of the continuity condition between adjacent elements, which will be explained in section 3.4.6. As a result, the inter-element section of the boundary will be considered as a part of the Dirichlet boundary Γ_u^e, as is also displayed in fig. 3.1.

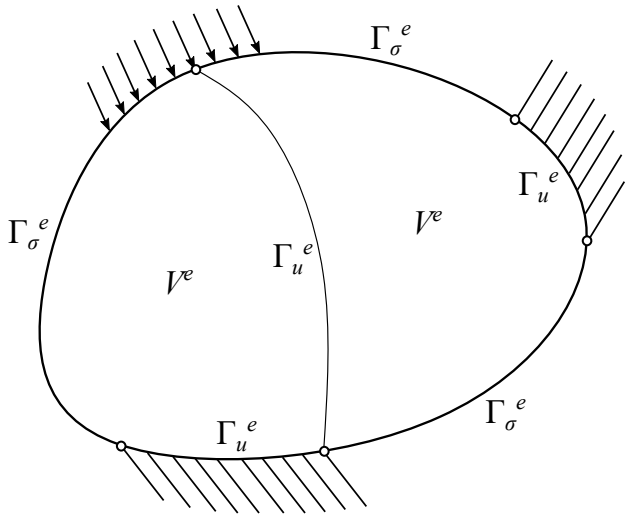

Figure 3.1: Discretization of the domain into finite elements

The individual elements can be of arbitrary shape and also no restrictions are placed on the number or edges of the individual elements.

3.2 Domain Approximation

As was stated in the introduction of the chapter, the first approximated field is the displacement field in the element domain V^e, expressed as

$$\boldsymbol{u} = \boldsymbol{U}\boldsymbol{X} + \boldsymbol{u_0} \text{ in } V^e. \tag{3.1}$$

Matrix $\boldsymbol{U}$ collects the basis functions, $\boldsymbol{X}$ is vector of unknown coefficients, also called generalized displacements and $\boldsymbol{u_0}$ is a vector of particular solutions.

The basis collected in matrix $\boldsymbol{U}$ is restricted to satisfy the homogeneous part of the spectral Lamé equation (2.30), such constraint is expressed as

$$\boldsymbol{\mathcal{D}k\mathcal{D}^*U} + \omega^2\rho\boldsymbol{U} = \boldsymbol{0} \text{ in } V^e. \tag{3.2}$$

Vector $\boldsymbol{u_0}$ is constructed as a particular solution to the prescribed body forces, hence relation

$$\boldsymbol{\mathcal{D}k\mathcal{D}^*u_0} + \omega^2\rho\boldsymbol{u_0} + \boldsymbol{b} = \boldsymbol{0} \text{ in } V^e \tag{3.3}$$

must hold.

In the case of the hybrid-Trefftz method, the strain field is restricted to directly satisfy the kinematic equations. Applying eq. (2.5) on (3.1) yields

$$\boldsymbol{\varepsilon} = \boldsymbol{\mathcal{D}^*u} = \boldsymbol{E}\boldsymbol{X} + \boldsymbol{\varepsilon_0}, \tag{3.4}$$

with the strain approximation basis $\boldsymbol{E} = \boldsymbol{\mathcal{D}^*U}$ and $\boldsymbol{\varepsilon_0} = \boldsymbol{\mathcal{D}^*u_0}$. Note that $\boldsymbol{E}$ is not an independent

basis, it is rather derived from basis $\boldsymbol{U}$ and therefore strain $\boldsymbol{\varepsilon}$ is not an independently approximated field.

To construct the displacement basis $\boldsymbol{U}$ and subsequently the strain basis $\boldsymbol{E}$, it is necessary to solve the homogeneous part of the spectral Lamé equation, which will be discussed in the following subsection.

3.2.1 Solution of the Homogeneous Spectral Lamé Equation

The spectral Lamé equation for the considered 2D case was derived in the previous chapter and is represented by eq. (2.31). Neglecting the body forces, a homogeneous part is recovered, which results in

$$(\lambda+\mu)\boldsymbol{\nabla}\boldsymbol{\nabla}^T\boldsymbol{u}+\mu\nabla^2\boldsymbol{u}+\omega^2\rho\boldsymbol{u}=\boldsymbol{0}. \tag{3.5}$$

This equation is expressed in terms of the displacement field $\boldsymbol{u}$ and represents two coupled partial differential equations. By the application of the Helmholtz decomposition, the previous equation can be reformulated in terms of different unknown fields and decoupled into two independent equations, which simplifies the solution procedure significantly.

The Helmholtz theorem [Arfken et al 2013c] states that any sufficiently smooth vector field can be expressed in terms of a scalar dilatational potential Φ_p and a vector potential $\boldsymbol{\Phi_s}$. For the 2-dimensional case, it can be shown that the vector potential reduces to one component only, therefore it becomes a scalar shear potential Φ_s. The relation can be expressed in matrix notation as

$$\boldsymbol{u}=\boldsymbol{\nabla}\Phi_p+\widetilde{\boldsymbol{\nabla}}\Phi_s, \tag{3.6}$$

where $\widetilde{\boldsymbol{\nabla}}=\begin{bmatrix}\partial/\partial y & -\partial/\partial x\end{bmatrix}^T$ is the curl operator in 2D.

Due to the linearity of the differential operators appearing in eq. (3.5), it is possible to investigate contributions of each term in relation (3.6) separately.

Dilatational Part

Taking the dilatational part of the displacement vector, that is substituting $\boldsymbol{u}=\boldsymbol{\nabla}\Phi_p$ into eq. (3.5), one obtains

$$(\lambda+\mu)\boldsymbol{\nabla}\boldsymbol{\nabla}^T(\boldsymbol{\nabla}\Phi_p)+\mu\nabla^2(\boldsymbol{\nabla}\Phi_p)+\omega^2\rho(\boldsymbol{\nabla}\Phi_p)=\boldsymbol{0}. \tag{3.7}$$

Using identities $\nabla^2\boldsymbol{\nabla}=\boldsymbol{\nabla}\nabla^2$ and $\boldsymbol{\nabla}^T\boldsymbol{\nabla}=\nabla^2$, equation (3.7) is rearranged as

$$\begin{aligned}(\lambda+\mu)\boldsymbol{\nabla}\nabla^2\Phi_p+\mu\boldsymbol{\nabla}\nabla^2\Phi_p+\omega^2\rho\boldsymbol{\nabla}\Phi_p&=\boldsymbol{0}\\ \boldsymbol{\nabla}\left[(\lambda+\mu)\nabla^2\Phi_p+\mu\nabla^2\Phi_p+\omega^2\rho\Phi_p\right]&=\boldsymbol{0}\\ \boldsymbol{\nabla}\left[(\lambda+2\mu)\nabla^2\Phi_p+\omega^2\rho\Phi_p\right]&=\boldsymbol{0},\end{aligned} \tag{3.8}$$

which implies that

$$\begin{aligned}(\lambda+2\mu)\nabla^2\Phi_p+\omega^2\rho\Phi_p =&C_1\\ \nabla^2\Phi_p+\omega^2\frac{\rho}{\lambda+2\mu}\Phi_p =&\frac{C_1}{\lambda+2\mu},\end{aligned} \tag{3.9}$$

where C_1 denotes an arbitrary constant. The particular solution of eq. (3.9)

$$\Phi_{p,p}=\frac{C_1}{\omega^2\rho} \tag{3.10}$$

is also constant and as the displacement field is obtained as gradient of the dilatational potential, contribution of $\Phi_{p,p}$ to the displacement field vanishes. Therefore, in the upcoming derivations only the homogeneous part of eq. (3.9) is studied.

Defining the pressure wave (p-wave) velocity as

$$c_p=\sqrt{\frac{\lambda+2\mu}{\rho}} \tag{3.11}$$

and the wave number related to p-waves as $k_p=\omega/c_p$, eq. (3.9) is reformulated

$$\nabla^2\Phi_p+k_p^2\Phi_p=0. \tag{3.12}$$

Shear Part

In this section the part of the displacement related to shear potential is examined. The relation $\boldsymbol{u}=\widetilde{\boldsymbol{\nabla}}\Phi_s$ is substituted into eq. (3.5)

$$(\lambda+\mu)\boldsymbol{\nabla}\boldsymbol{\nabla}^T(\widetilde{\boldsymbol{\nabla}}\Phi_s)+\mu\nabla^2\left(\widetilde{\boldsymbol{\nabla}}\Phi_s\right)+\omega^2\rho(\widetilde{\boldsymbol{\nabla}}\Phi_s)=\mathbf{0}. \tag{3.13}$$

As identities $\boldsymbol{\nabla}^T\widetilde{\boldsymbol{\nabla}}=0$ and $\nabla^2\widetilde{\boldsymbol{\nabla}}=\widetilde{\boldsymbol{\nabla}}\nabla^2$ hold, the previous equation results in

$$\begin{aligned}\mu\nabla^2\widetilde{\boldsymbol{\nabla}}\Phi_s+\omega^2\rho\widetilde{\boldsymbol{\nabla}}\Phi_s =&\mathbf{0}\\ \widetilde{\boldsymbol{\nabla}}(\mu\nabla^2\Phi_s+\omega^2\rho\Phi_s) =&\mathbf{0}.\end{aligned} \tag{3.14}$$

Using the relation for a shear wave (s-wave) velocity

$$c_s=\sqrt{\frac{\mu}{\rho}} \tag{3.15}$$

and the definition of the shear wave number $k_s=\omega/c_s$, eq. (3.14) implies that

$$\nabla^2\Phi_s+k_s^2\Phi_s=\frac{C_2}{\mu}, \tag{3.16}$$

with C_2 being an arbitrary constant. Similarly to the p-wave case, the particular solution of eq. (3.16) can be neglected and only the homogeneous part is of interest.

By the use of the Helmholtz decomposition, system of two coupled partial differential equations (3.5) in terms of displacement components u and v was transformed into two independent partial differential equations (3.12) and (3.16) in terms of the dilatational potential Φ_p and the shear potential Φ_s. Both equations have a similar form and are denoted as the Helmholtz equation [Arfken et al 2013d]. In the next section, a solution procedure of such equation is explained. Afterwards, when the potentials are known, the displacement field can be recovered by the application of eq. (3.6).

Solution of Helmholtz Equation

The solution of the previously derived Helmholtz equation will now be discussed. Consider a general form of the homogeneous part of eqs. (3.12) and (3.16)

$$\begin{aligned} \nabla^2\Phi_\alpha + k_\alpha^2\Phi_\alpha =&0 \\ \frac{\partial^2\Phi_\alpha}{\partial x^2} + \frac{\partial^2\Phi_\alpha}{\partial y^2} + k_\alpha^2\Phi_\alpha =&0, \end{aligned} \tag{3.17}$$

where $\alpha = \{p,s\}$. Eq. (3.17) can be solved both in Cartesian and polar reference frame, however, only the latter will be explained in this section. In the polar coordinates, eq. (3.17) is expressed as [Arfken et al 2013d]

$$\frac{\partial^2\Phi_\alpha}{\partial r^2} + \frac{1}{r}\frac{\partial\Phi_\alpha}{\partial r} + \frac{1}{r^2}\frac{\partial^2\Phi_\alpha}{\partial\theta^2} + k_\alpha^2\Phi_\alpha = 0, \tag{3.18}$$

where r and θ are the radial and angular coordinates respectively. Adopting the separation approach, the solution is sought in the form

$$\Phi_{\alpha,n} = W_n(k_\alpha r)\exp(in\theta), \tag{3.19}$$

where $W_n(k_\alpha r)$ is so far unknown function defined in the radial direction and n is an integer. Substituting the previous ansatz into eq. (3.18) yields

$$\begin{aligned} \frac{\partial^2 W_n(k_\alpha r)}{\partial r^2}\exp(in\theta) + \frac{1}{r}\frac{\partial W_n(k_\alpha r)}{\partial r}\exp(in\theta) - \frac{n^2}{r^2}W_n(k_\alpha r)\exp(in\theta) + k_\alpha^2 W_n(k_\alpha r)\exp(in\theta) =&0 \\ \frac{\partial^2 W_n(k_\alpha r)}{\partial r^2} + \frac{1}{r}\frac{\partial W_n(k_\alpha r)}{\partial r} + (k_\alpha^2 - \frac{n^2}{r^2})W_n(k_\alpha r) =&0 \\ \frac{1}{k_\alpha^2}\frac{\partial^2 W_n(k_\alpha r)}{\partial r^2} + \frac{1}{k_\alpha^2}\frac{1}{r}\frac{\partial W_n(k_\alpha r)}{\partial r} + (1 - \frac{n^2}{(k_\alpha r)^2})W_n(k_\alpha r) =&0. \end{aligned} \tag{3.20}$$

Using a coordinate substitution $\zeta = k_\alpha r$, the previous equation can be reformulated as

$$\frac{\partial^2 W_n(\zeta)}{\partial\zeta^2} + \frac{1}{\zeta}\frac{\partial W_n(\zeta)}{\partial\zeta} + (1 - \frac{n^2}{\zeta^2})W_n(\zeta) = 0. \tag{3.21}$$

Eq. (3.21) is known as the Bessel equation [Arfken et al 2013a]. Since it is a second order linear differential equation, for each integer n there must exist two linearly independent solutions. In addition, depending on the analysed problem, various formulations of these linearly independent pairs may be adopted. In this thesis the following representations of the solutions $W_n(\zeta)$ are considered:

- Bessel function of the first and second kind $J_n(\zeta)$ and $Y_n(\zeta)$
- Hankel function of the first and second kind $H_n^{(1)}(\zeta)$ and $H_n^{(2)}(\zeta)$

The Hankel functions can be expressed in terms of the Bessel functions as

$$\begin{aligned} H_n^{(1)}(\zeta) =& J_n(\zeta) + iY_n(\zeta), \\ H_n^{(2)}(\zeta) =& J_n(\zeta) - iY_n(\zeta). \end{aligned} \tag{3.22}$$

For n being an integer, Bessel functions of the first kind take finite values at the origin, while Bessel functions of the second kind are singular at $\zeta = 0$, therefore are suited for modelling of singular stress fields. However, if non singular fields are of interest, the origin needs to be placed outside of the element. Since the Hankel functions are constructed as a linear combination of two of the Bessel function kinds, also these are singular at the origin. It can be shown that under certain restrictions the Hankel functions satisfy the Sommerfeld radiation condition. This property is advantageous when unbounded media are analysed, which is discussed in chapter 4. Bessel functions of the first and second kind and orders $n = 0,1,2$ are plotted in fig. 3.2.

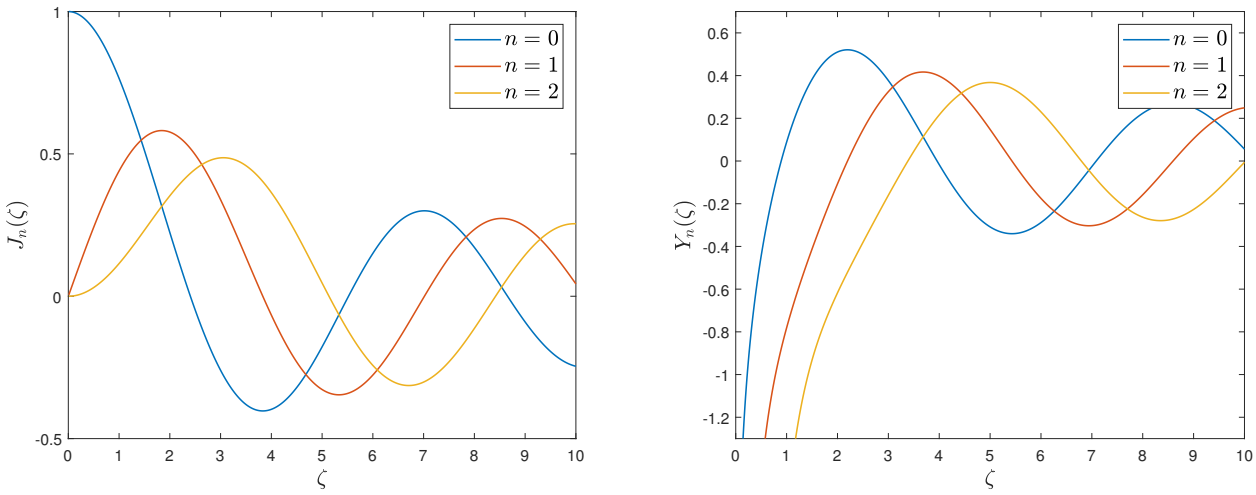

Figure 3.2: Bessel functions of the first and second kind

The unknown dilatational and shear potentials $\Phi_{p,n}$ and $\Phi_{s,n}$ for a single order n were found as a solution of the underlying Helmholtz equations (3.12) and (3.16) and are expressed by eq. (3.19). Substituting the individual wave numbers, the relations are rephrased

$$\Phi_{p,n} = W_n(k_p r)\exp(in\theta), \tag{3.23}$$

$$\Phi_{s,n} = W_n(k_s r)\exp(in\theta). \tag{3.24}$$

Any of the previously mentioned solutions of the Bessel equation can be adopted for the radial component W_n. Note that in general $n \in \mathbb{Z}$, therefore there is an infinite number of functions satisfying the Helmholtz equations (3.12) and (3.16). The complete solution is then expressed as a linear combination of all the terms

$$\Phi_p = \sum_{n=-\infty}^{\infty} c_{p,n}\Phi_{p,n}, \tag{3.25}$$

$$\Phi_s = \sum_{n=-\infty}^{\infty} c_{s,n}\Phi_{s,n}, \tag{3.26}$$

where $c_{p,n}$ and $c_{s,n}$ are unknown coefficients. Using eq. (3.6), the displacement field can be recovered

$$\boldsymbol{u} = \boldsymbol{\nabla}\Phi_p + \widetilde{\boldsymbol{\nabla}}\Phi_s = \sum_{n=-\infty}^{\infty} \left(c_{p,n}\boldsymbol{\nabla}\Phi_{p,n} + c_{s,n}\widetilde{\boldsymbol{\nabla}}\Phi_{s,n} \right). \tag{3.27}$$

The coefficients $c_{p,n}$ and $c_{s,n}$ are found based on the given boundary conditions, but for most of the practical cases it is an infeasible task. However, the individual parts $\boldsymbol{\nabla}\Phi_{p,n}$ and $\widetilde{\boldsymbol{\nabla}}\Phi_{s,n}$ are constructed to satisfy the differential equation and in addition, form a complete basis for $n \in \mathbb{Z}$, therefore they are suitable for construction of the displacement approximation matrix $\boldsymbol{U}$.

3.2.2 Domain Approximation Basis

In this subsection, previously derived solutions of the homogeneous Lamé equation are used to form the displacement approximation basis $\boldsymbol{U}$ and consequently the strain basis $\boldsymbol{E}$.

The displacement field was decomposed into dilatational and shear potentials based on the eq. (3.6). This motivates to also separate the contributions of individual modes in the basis $\boldsymbol{U}$. Therefore, for a single order n, a submatrix $\boldsymbol{U_n}$ collecting two basis functions for each displacement component (one for each mode) has the following form:

$$\boldsymbol{U_n} = \begin{bmatrix} \boldsymbol{\nabla}\Phi_{p,n} & \widetilde{\boldsymbol{\nabla}}\Phi_{s,n} \end{bmatrix} = \begin{bmatrix} \boldsymbol{\nabla}[W_n(k_p r)\exp(in\theta)] & \widetilde{\boldsymbol{\nabla}}[W_n(k_s r)\exp(in\theta)] \end{bmatrix}. \tag{3.28}$$

The first column includes the dilatational mode and the second column represents the shear mode. To form the complete basis $\boldsymbol{U}$, orders $-N < n < N$ are considered and the submatrices are combined as

$$\boldsymbol{U} = \left[\begin{array}{c:c:c:c} \boldsymbol{U_{-N}} & \cdots & \boldsymbol{U_n} & \cdots & \boldsymbol{U_N} \end{array} \right], \tag{3.29}$$

where N is the chosen maximum order of the function W_n, also called the maximum degree of p-refinement. Using this structure, there are $2N+1$ submatrices $\boldsymbol{U_n}$ included in the complete matrix $\boldsymbol{U}$, each having two columns, one related to the dilatational mode and the other to the shear mode. Therefore, the basis matrix $\boldsymbol{U}$ overall collects $2(2N+1)$ approximation functions (for each displacement component). The more terms are included in the basis the richer the element gets. However, this comes with the cost of numerical issues, since high order Bessel functions take

much smaller values compared to the lower order ones, when evaluated in the vicinity of the origin. To a certain extent, this problem can be reduced by adopting a scaling procedure, which will be explained in detail in chapter 6.

In the following, eq. (3.28) will be investigated in more detail and the exact form of matrix $\boldsymbol{U_n}$ will be derived. One can note the differential operators in eq. (3.28) are defined in the Cartesian coordinates, however, the functions $\Phi_{p,n}$ and $\Phi_{s,n}$ depend on polar coordinates r and θ. One could express the polar coordinates in terms of the Cartesian ones, substitute the expressions and perform the differentiation in a software for symbolic calculations. However, a more elegant way is to perform the differentiation in the polar reference system and afterwards transform the matrix back to the Cartesian one, which can be illustrated as

$$\boldsymbol{U_n} = \begin{bmatrix} \boldsymbol{\nabla}\Phi_{p,n} & \widetilde{\boldsymbol{\nabla}}\Phi_{s,n} \end{bmatrix} = \begin{bmatrix} \dfrac{\partial \Phi_{p,n}}{\partial x} & \dfrac{\partial \Phi_{s,n}}{\partial y} \\ \dfrac{\partial \Phi_{p,n}}{\partial y} & -\dfrac{\partial \Phi_{s,n}}{\partial x} \end{bmatrix} = \begin{bmatrix} \cos\theta & -\sin\theta \\ \sin\theta & \cos\theta \end{bmatrix} \begin{bmatrix} \dfrac{\partial \Phi_{p,n}}{\partial r} & \dfrac{1}{r}\dfrac{\partial \Phi_{s,n}}{\partial \theta} \\ \dfrac{1}{r}\dfrac{\partial \Phi_{p,n}}{\partial \theta} & -\dfrac{\partial \Phi_{s,n}}{\partial r} \end{bmatrix} = \boldsymbol{T}\boldsymbol{U}_{\boldsymbol{n}}^{r,\theta}. \tag{3.30}$$

The transformation matrix is denoted by $\boldsymbol{T}$. As was already discussed, matrix $\boldsymbol{U_n}$ collects approximation functions of the displacement components in x and y direction. Similarly, matrix $\boldsymbol{U}_{\boldsymbol{n}}^{r,\theta}$ also contains basis functions, which now approximate the displacement components in r and θ direction. It can be further developed as

$$\begin{aligned} \boldsymbol{U}_{\boldsymbol{n}}^{r,\theta} &= \begin{bmatrix} \dfrac{\partial W_n(k_p r)}{\partial r} & \dfrac{in}{r} W_n(k_s r) \\ \dfrac{in}{r} W_n(k_p r) & -\dfrac{\partial W_n(k_s r)}{\partial r} \end{bmatrix} \exp(in\theta) = \\ &= \frac{1}{2} \begin{bmatrix} k_p(W_{n-1} - W_{n+1}) & ik_s \dfrac{2n}{k_s r} W_n \\ ik_p \dfrac{2n}{k_p r} W_n & k_s(W_{n+1} - W_{n-1}) \end{bmatrix} \exp(in\theta) = \\ &= \frac{1}{2} \begin{bmatrix} k_p(W_{n-1} - W_{n+1}) & ik_s(W_{n-1} + W_{n+1}) \\ ik_p(W_{n-1} + W_{n+1}) & k_s(W_{n+1} - W_{n-1}) \end{bmatrix} \exp(in\theta). \end{aligned} \tag{3.31}$$

In the previous manipulations, the relations

$$2\frac{\partial W_n(\zeta)}{\partial \zeta} = W_{n-1}(\zeta) - W_{n+1}(\zeta),$$

$$\frac{2n}{\zeta} W_n(\zeta) = W_{n-1}(\zeta) + W_{n+1}(\zeta)$$

between the solutions of the Bessel equation for various orders n were used [Arfken et al 2013a].

The individual functions contained in the basis $\boldsymbol{U_n}$ are plotted in figures 3.3 and 3.4. The Bessel functions of the first kind and of orders $n = 0,1,2$ are considered as the function W_n. They are evaluated on a circular region centred at origin, the particular values of the wave numbers were chosen as $k_p = 0.475$ 1/m and $k_s = 0.889$ 1/m. Fig. 3.3 displays the real part of the displacement

components related to the p-wave solution for various orders n, therefore for a fixed n it represents the evaluation of the first column of matrix $\boldsymbol{U_n}$. On the other hand, fig. 3.4 depicts the real part of the displacement components associated to s-waves, hence these functions are contained in the second column of basis $\boldsymbol{U_n}$.

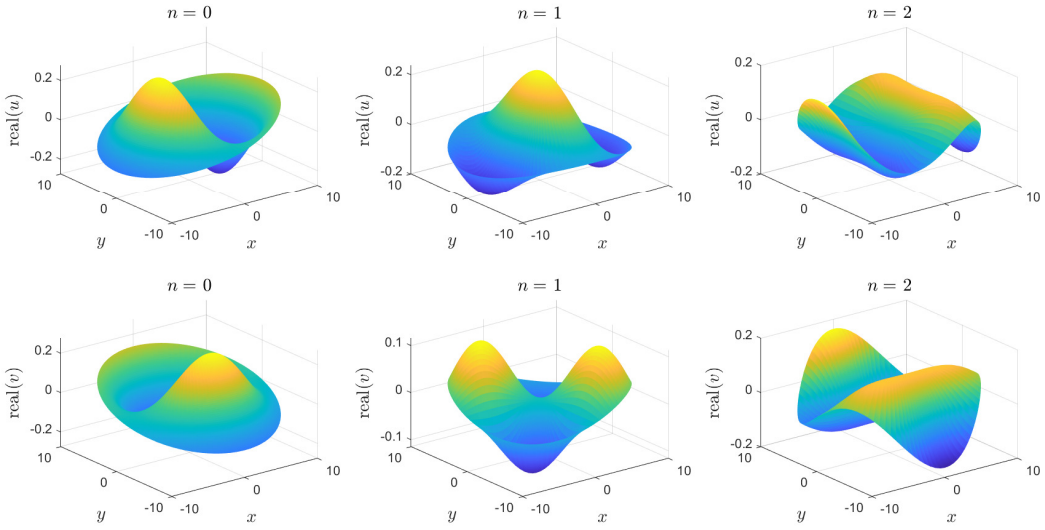

Figure 3.3: P-wave part of the displacement basis

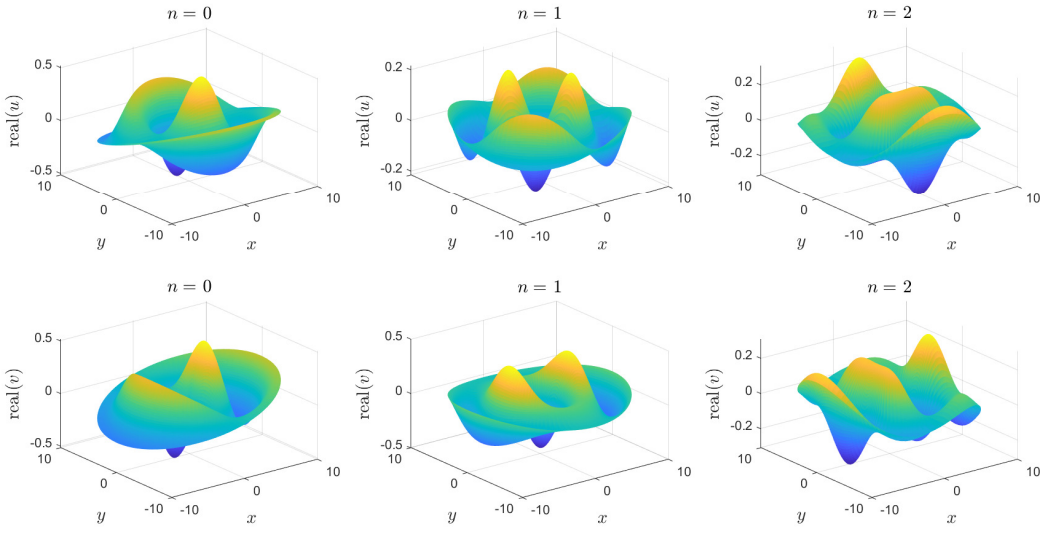

Figure 3.4: S-wave part of the displacement basis

Similar idea can now be applied for the derivation of the strain field basis $\boldsymbol{E}$. In eq. (3.4) it is defined as

$$\boldsymbol{E} = \boldsymbol{\mathcal{D}}^{*}\boldsymbol{U} = \left[\begin{array}{c:c:c:c:c} \boldsymbol{E_{-N}} & \cdots & \boldsymbol{E_n} & \cdots & \boldsymbol{E_N} \end{array} \right]. \tag{3.32}$$

Analogously to the displacement basis ordering, also the strain basis can be built up from the submatrices $\boldsymbol{E_n}$, which carry the basis functions approximating individual strain components in Cartesian coordinate system for a single order n. To compute it, firstly matrix $\boldsymbol{E_n^{r,\theta}}$ collecting functions approximating the strains in the radial and angular directions is calculated and afterwards it is transformed to the original reference frame using strain transformation matrix $\boldsymbol{T_\varepsilon}$.

$$\begin{aligned}\boldsymbol{E_n} = \boldsymbol{\mathcal{D}}^* \boldsymbol{U_n} &= \begin{bmatrix} \dfrac{\partial}{\partial x} & 0 \\ 0 & \dfrac{\partial}{\partial y} \\ \dfrac{\partial}{\partial y} & \dfrac{\partial}{\partial x} \end{bmatrix} \begin{bmatrix} \dfrac{\partial \Phi_{p,n}}{\partial x} & \dfrac{\partial \Phi_{s,n}}{\partial y} \\ \dfrac{\partial \Phi_{p,n}}{\partial y} & -\dfrac{\partial \Phi_{s,n}}{\partial x} \end{bmatrix} = \\ &= \underbrace{\begin{bmatrix} \cos^2\theta & \sin^2\theta & \cos\theta\sin\theta \\ \sin^2\theta & \cos^2\theta & -\cos\theta\sin\theta \\ -2\cos\theta\sin\theta & 2\cos\theta\sin\theta & \cos^2\theta - \sin^2\theta \end{bmatrix}}_{\boldsymbol{T_\varepsilon}} \underbrace{\begin{bmatrix} \dfrac{\partial}{\partial r} & 0 \\ 0 & \dfrac{1}{r}\dfrac{\partial}{\partial \theta} \\ \dfrac{1}{r}\dfrac{\partial}{\partial \theta} & \dfrac{\partial}{\partial r} \end{bmatrix} \begin{bmatrix} \dfrac{\partial \Phi_p}{\partial r} & \dfrac{1}{r}\dfrac{\partial \Phi_s}{\partial \theta} \\ \dfrac{1}{r}\dfrac{\partial \Phi_p}{\partial \theta} & -\dfrac{\partial \Phi_s}{\partial r} \end{bmatrix}}_{\boldsymbol{E_n^{r,\theta}}} = \\ &= \boldsymbol{T_\varepsilon} \boldsymbol{E_n^{r,\theta}}.\end{aligned} \tag{3.33}$$

This way, the formulas contained in the matrix $\boldsymbol{E_n^{r,\theta}}$ can be easily computed analytically and displayed in one line

$$\begin{aligned}\boldsymbol{E_n^{r,\theta}} &= \begin{bmatrix} \dfrac{\partial^2 \Phi_p}{\partial r^2} & \dfrac{1}{r}\dfrac{\partial^2 \Phi_s}{\partial \theta \partial r} \\ \dfrac{1}{r^2}\dfrac{\partial^2 \Phi_p}{\partial \theta^2} & -\dfrac{1}{r}\dfrac{\partial^2 \Phi_s}{\partial r \partial \theta} \\ 2\dfrac{1}{r}\dfrac{\partial^2 \Phi_p}{\partial r \partial \theta} & \dfrac{1}{r^2}\dfrac{\partial^2 \Phi_s}{\partial \theta^2} - \dfrac{\partial^2 \Phi_s}{\partial r^2} \end{bmatrix} = \\ &= \frac{1}{4} \begin{bmatrix} k_p^2(W_{n-2} - 2W_n + W_{n+2}) & ik_s^2(W_{n-2} - W_{n+2}) \\ -k_p^2(W_{n-2} + 2W_n + W_{n+2}) & -ik_s^2(W_{n-2} - W_{n+2}) \\ 2ik_p^2(W_{n-2} - W_{n+2}) & -2k_s^2(W_{n-2} + W_{n+2}) \end{bmatrix} \exp(in\theta).\end{aligned} \tag{3.34}$$

From the ordering of the bases $\boldsymbol{U}$ and $\boldsymbol{E}$ also layout of the vector of unknown coefficients $\boldsymbol{X}$ can be deduced. It can be visualized as

$$\boldsymbol{X} = \left[\begin{array}{c:c:c:c} \boldsymbol{X}_{-N} & \cdots & \boldsymbol{X}_n & \cdots & \boldsymbol{X}_N \end{array} \right]^T = \left[\begin{array}{c:c:c:c:c} X^p_{-N} \quad X^s_{-N} & \cdots & X^p_n \quad X^s_n & \cdots & X^p_N \quad X^s_N \end{array} \right]^T, \tag{3.35}$$

where the superscript p or s indicates if the component multiplies function related to the dilatational or shear potential and the subscript specifies the order of the associated basis function. For a specified maximum order N, there are $2(2N+1)$ unknown coefficients collected in the vector $\boldsymbol{X}$.

3.3 Boundary Approximation

The second field to be approximated are the tractions on the Dirichlet boundary Γ_u^e, which contains not only the external part of boundary, where the displacements are prescribed, but also the inter-element edges, where displacement continuity needs to be enforced. The relation reads

$$\boldsymbol{t} = \boldsymbol{Z}\boldsymbol{p} \text{ on } \Gamma_u^e, \tag{3.36}$$

where $\boldsymbol{Z}$ is the matrix gathering the boundary approximation basis and $\boldsymbol{p}$ stands for vector of unknown coefficients, also referred to as generalized tractions. The only restrictions placed upon basis $\boldsymbol{Z}$ are linear independence and completeness. Note that if the Dirichlet boundary consists of more parts (e.g. various edges with different displacement boundary condition or a connection of more elements), the tractions on each part are approximated independently. In such case, eq. (3.36) can be reformulated to

$$\boldsymbol{t} = \boldsymbol{Z}\boldsymbol{p}_i \text{ on } \Gamma_{u_i}^e, \tag{3.37}$$

where $i = 1,2,\ldots,n_D$ with n_D being the total number of Dirichlet edges.

In this work the Chebyshev polynomials of type I are adopted for the basis $\boldsymbol{Z}$. They are defined for a side coordinate $\xi \in \langle -1,1 \rangle$ as [Arfken et al 2013b]

$$Z_m(\xi) = \cos\left(m \cos^{-1} \xi\right), \tag{3.38}$$

where $m = 0,1,2,\ldots,M$ denotes the order of the polynomial. The first four basis functions are depicted in fig. 3.5.

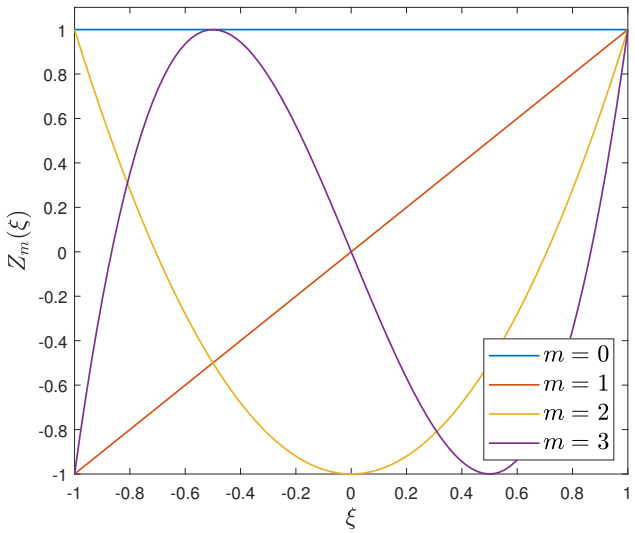

Figure 3.5: Traction approximation basis functions

The individual components are then ordered in the complete matrix $\boldsymbol{Z}$

$$\boldsymbol{Z} = \begin{bmatrix} \boldsymbol{Z_v} & \boldsymbol{0} \\ \boldsymbol{0} & \boldsymbol{Z_v} \end{bmatrix} = \left[\begin{array}{cccc:cccc} Z_0 & Z_1 & \cdots & Z_M & 0 & 0 & \cdots & 0 \\ 0 & 0 & \cdots & 0 & Z_0 & Z_1 & \cdots & Z_M \end{array}\right], \tag{3.39}$$

where $\boldsymbol{Z_v} = \begin{bmatrix} Z_0 & Z_1 & \cdots & Z_M \end{bmatrix}$ is the basis approximating a single traction component. Therefore, there are $2(M+1)$ columns contained in the complete $\boldsymbol{Z}$ matrix. Consequently, the vector of generalized tractions $\boldsymbol{p}$ can be expressed as

$$\boldsymbol{p} = \begin{bmatrix} \boldsymbol{p_x}^T & \boldsymbol{p_y}^T \end{bmatrix}^T, \tag{3.40}$$

where the subvectors $\boldsymbol{p_x}$ and $\boldsymbol{p_y}$ collect the unknown coefficients related to the individual traction components t_x and t_y respectively.

From the layout of matrix $\boldsymbol{Z}$ and vector $\boldsymbol{p}$ one can note that the traction components t_x and t_y are approximated independently using the same basis $\boldsymbol{Z_v}$. Such relation can be expressed as

$$t_x = \boldsymbol{Z_v p_x}, \tag{3.41}$$

$$t_y = \boldsymbol{Z_v p_y}. \tag{3.42}$$

The traction vector $\boldsymbol{t}(x,y)$ is a function of Cartesian coordinates, however, the approximation basis $\boldsymbol{Z}(\xi)$ is a function of the local edge coordinate $\xi \in \langle -1,1 \rangle$. Therefore, for every Dirichlet edge, there must exist a function $\boldsymbol{h}(\xi)$ mapping the coordinate ξ to Cartesian coordinates $\begin{bmatrix} x & y \end{bmatrix}^T$.

3.4 Finite Element System of Equations

Until this point, the approximation bases of both displacement field and boundary traction field were introduced. In the following section the finite element system of equations is derived using the Galerkin weighted residual method. Firstly, the equilibrium equations are weakly imposed, by substitution of the material law and the kinematic relations the first set of finite element equations can be formulated. Afterwards, Dirichlet boundary conditions and continuity equations are forced to hold in a weak sense and combined to form the second set of the finite element system of equations.

The governing system is firstly derived for a single finite element. To start with, it is assumed that the displacement boundary condition is applied on a single continuous portion of the complete boundary. Afterwards, generalizations including non continuous displacement boundary conditions and domains discretized with multiple elements are discussed.

3.4.1 Equilibrium Equations

The equilibrium equation in the frequency domain was derived in eq. (2.32). It is required that its residual form weighted by the domain displacement approximation basis $\widehat{\boldsymbol{U}}$ and integrated over

the domain of the element is equal to zero

$$\int \widehat{\boldsymbol{U}}^T \left(\boldsymbol{\mathcal{D}}\boldsymbol{\sigma} + \omega^2 \rho \boldsymbol{u} + \boldsymbol{b}\right) \mathrm{d}V^e = \boldsymbol{0}. \tag{3.43}$$

The symbol $\widehat{(\cdot)}$ denotes the complex conjugate. Plugging in the displacement approximation (3.1) and splitting the integral yields

$$\int \widehat{\boldsymbol{U}}^T \boldsymbol{\mathcal{D}}\boldsymbol{\sigma}\, dV^e + \omega^2 \int \rho \widehat{\boldsymbol{U}}^T \boldsymbol{U}\, \mathrm{d}V^e\, \boldsymbol{X} + \omega^2 \int \rho \widehat{\boldsymbol{U}}^T \boldsymbol{u_0}\, \mathrm{d}V^e + \int \widehat{\boldsymbol{U}}^T \boldsymbol{b}\, \mathrm{d}V^e = \boldsymbol{0}. \tag{3.44}$$

The first integral can be modified by applying integration by parts technique

$$\int \widehat{\boldsymbol{U}}^T \boldsymbol{\mathcal{D}}\boldsymbol{\sigma}\, \mathrm{d}V^e = \int \widehat{\boldsymbol{U}}^T \boldsymbol{N}\boldsymbol{\sigma}\, \mathrm{d}\Gamma^e - \int \left(\boldsymbol{\mathcal{D}}^* \widehat{\boldsymbol{U}}\right)^T \boldsymbol{\sigma}\, \mathrm{d}V^e. \tag{3.45}$$

Subsequently, the first term on the right hand side is reformulated by the substitution of the boundary equilibrium equation (2.35)

$$\int \widehat{\boldsymbol{U}}^T \boldsymbol{\mathcal{D}}\boldsymbol{\sigma}\, \mathrm{d}V^e = \int \widehat{\boldsymbol{U}}^T \boldsymbol{t}\, \mathrm{d}\Gamma^e - \int \left(\boldsymbol{\mathcal{D}}^* \widehat{\boldsymbol{U}}\right)^T \boldsymbol{\sigma}\, \mathrm{d}V^e. \tag{3.46}$$

The boundary integral can now be split into two integrals, one performed over the Dirichlet boundary Γ_u^e and the other over the Neumann boundary Γ_σ^e. Afterwards, on Γ_σ^e the boundary traction condition (2.37) can directly be inserted and on Γ_u^e the boundary traction approximation based on eq. (3.36) is substituted. The previous equation then results in

$$\int \widehat{\boldsymbol{U}}^T \boldsymbol{\mathcal{D}}\boldsymbol{\sigma}\, \mathrm{d}V^e = \int \widehat{\boldsymbol{U}}^T \boldsymbol{t_\Gamma}\, \mathrm{d}\Gamma_\sigma^e + \int \widehat{\boldsymbol{U}}^T \boldsymbol{Z}\, \mathrm{d}\Gamma_u^e\, \boldsymbol{p} - \int \left(\boldsymbol{\mathcal{D}}^* \widehat{\boldsymbol{U}}\right)^T \boldsymbol{\sigma}\, \mathrm{d}V^e. \tag{3.47}$$

Eq. (3.47) in now inserted back into eq. (3.44) and the terms are rearranged

$$\begin{aligned} \int \left(\boldsymbol{\mathcal{D}}^* \widehat{\boldsymbol{U}}\right)^T \boldsymbol{\sigma}\, \mathrm{d}V^e = \int \widehat{\boldsymbol{U}}^T \boldsymbol{t_\Gamma}\, \mathrm{d}\Gamma_\sigma^e + \int \widehat{\boldsymbol{U}}^T \boldsymbol{Z}\, \mathrm{d}\Gamma_u^e\, \boldsymbol{p} + \omega^2 \int \rho \widehat{\boldsymbol{U}}^T \boldsymbol{U}\, \mathrm{d}V^e\, \boldsymbol{X} + \\ + \omega^2 \int \rho \widehat{\boldsymbol{U}}^T \boldsymbol{u_0}\, \mathrm{d}V^e + \int \widehat{\boldsymbol{U}}^T \boldsymbol{b}\, \mathrm{d}V^e. \end{aligned} \tag{3.48}$$

3.4.2 Elasticity and Kinematic Equations

In this section the material law and the kinematic equations are substituted into eq. (3.48). Firstly, the integral on the left hand side of eq. (3.48) is developed and afterwards the resulting expression is back substituted.

Inserting the material law into the first integral of the previous equation and expanding the strain vector based on eq. (3.4) results in

$$\int (\boldsymbol{\mathcal{D}}^* \widehat{\boldsymbol{U}})^T \boldsymbol{\sigma}\, \mathrm{d}V^e = \int (\boldsymbol{\mathcal{D}}^* \widehat{\boldsymbol{U}})^T \boldsymbol{k}\boldsymbol{\varepsilon}\, \mathrm{d}V^e = \int (\boldsymbol{\mathcal{D}}^* \widehat{\boldsymbol{U}})^T \boldsymbol{k}\boldsymbol{E}\, \mathrm{d}V^e\, \boldsymbol{X} + \int (\boldsymbol{\mathcal{D}}^* \widehat{\boldsymbol{U}})^T \boldsymbol{k}\boldsymbol{\varepsilon_0}\, \mathrm{d}V^e. \tag{3.49}$$

Subsequently, both integrals on the right hand side are individually integrated by parts and modi-

fied. Starting with the first one

$$\begin{aligned}\int (\boldsymbol{\mathcal{D}}^*\widehat{\boldsymbol{U}})^T \boldsymbol{k}\boldsymbol{E}\,\mathrm{d}V^e\,\boldsymbol{X} &= \int \widehat{\boldsymbol{U}}^T \boldsymbol{N}\boldsymbol{k}\boldsymbol{E}\,\mathrm{d}\Gamma^e\,\boldsymbol{X} - \int \widehat{\boldsymbol{U}}^T \boldsymbol{\mathcal{D}}\boldsymbol{k}\boldsymbol{E}\,\mathrm{d}V^e\,\boldsymbol{X} = \\ &= \int \widehat{\boldsymbol{U}}^T \boldsymbol{N}\boldsymbol{k}\boldsymbol{E}\,\mathrm{d}\Gamma^e\,\boldsymbol{X} - \int \widehat{\boldsymbol{U}}^T \underbrace{\boldsymbol{\mathcal{D}}\boldsymbol{k}\boldsymbol{\mathcal{D}}^*\boldsymbol{U}}\,\mathrm{d}V^e\,\boldsymbol{X}.\end{aligned} \tag{3.50}$$

In section 3.2, it is explained that the domain approximation basis $\boldsymbol{U}$ has to satisfy the homogeneous part of the governing Lamé equation, expressed by means of eq. (3.2). This equation can be reformulated as

$$\boldsymbol{\mathcal{D}}\boldsymbol{k}\boldsymbol{\mathcal{D}}^*\boldsymbol{U} = -\omega^2\rho\boldsymbol{U} \text{ in } V^e. \tag{3.51}$$

One can note the the term on the left hand side of the previous equation can also be spotted in eq. (3.50). Therefore, eq. (3.51) is substituted into eq. (3.50), which yields

$$\int (\boldsymbol{\mathcal{D}}^*\widehat{\boldsymbol{U}})^T \boldsymbol{k}\boldsymbol{E}\,\mathrm{d}V^e\,\boldsymbol{X} = \int \widehat{\boldsymbol{U}}^T \boldsymbol{N}\boldsymbol{k}\boldsymbol{E}\,\mathrm{d}\Gamma^e\,\boldsymbol{X} + \omega^2 \int \rho\widehat{\boldsymbol{U}}^T \boldsymbol{U}\,\mathrm{d}V^e\,\boldsymbol{X}. \tag{3.52}$$

Similar approach is also applied to the second integral on the right hand side of eq. (3.49), firstly it is integrated by parts

$$\begin{aligned}\int (\boldsymbol{\mathcal{D}}^*\widehat{\boldsymbol{U}})^T \boldsymbol{k}\boldsymbol{\varepsilon_0}\,\mathrm{d}V^e &= \int \widehat{\boldsymbol{U}}^T \boldsymbol{N}\boldsymbol{k}\boldsymbol{\varepsilon_0}\,\mathrm{d}\Gamma^e - \int \widehat{\boldsymbol{U}}^T \boldsymbol{\mathcal{D}}\boldsymbol{k}\boldsymbol{\varepsilon_0}\,\mathrm{d}V^e = \\ &= \int \widehat{\boldsymbol{U}}^T \boldsymbol{N}\boldsymbol{k}\boldsymbol{\varepsilon_0}\,\mathrm{d}\Gamma^e - \int \widehat{\boldsymbol{U}}^T \underbrace{\boldsymbol{\mathcal{D}}\boldsymbol{k}\boldsymbol{\mathcal{D}}^*\boldsymbol{u_0}}\,\mathrm{d}V^e.\end{aligned} \tag{3.53}$$

Vector $\boldsymbol{u_0}$ is constructed as a particular solution to certain body forces $\boldsymbol{b}$, therefore it directly satisfies the particular part of the Lamé equation described by eq. (3.3). Reformulating this relation as

$$\boldsymbol{\mathcal{D}}\boldsymbol{k}\boldsymbol{\mathcal{D}}^*\boldsymbol{u_0} = -\omega^2\rho\boldsymbol{u_0} - \boldsymbol{b} \text{ in } V^e \tag{3.54}$$

allows a direct substitution to eq. (3.53), where the same term appears. This procedure results in

$$\int (\boldsymbol{\mathcal{D}}^*\widehat{\boldsymbol{U}})^T \boldsymbol{k}\boldsymbol{\varepsilon_0}\,\mathrm{d}V^e = \int \widehat{\boldsymbol{U}}^T \boldsymbol{N}\boldsymbol{k}\boldsymbol{\varepsilon_0}\,\mathrm{d}\Gamma^e + \omega^2 \int \rho\widehat{\boldsymbol{U}}^T \boldsymbol{u_0}\,\mathrm{d}V^e + \int \widehat{\boldsymbol{U}}^T \boldsymbol{b}\,\mathrm{d}V^e. \tag{3.55}$$

Finally, eqs. (3.52) and (3.55) can be inserted back into eq. (3.49), which yields

$$\begin{aligned}\int (\boldsymbol{\mathcal{D}}^*\widehat{\boldsymbol{U}})^T \boldsymbol{\sigma}\,\mathrm{d}V^e = &\int \widehat{\boldsymbol{U}}^T \boldsymbol{N}\boldsymbol{k}\boldsymbol{E}\,\mathrm{d}\Gamma^e\,\boldsymbol{X} + \omega^2 \int \rho\widehat{\boldsymbol{U}}^T \boldsymbol{U}\,\mathrm{d}V^e\,\boldsymbol{X} + \\ &+ \int \widehat{\boldsymbol{U}}^T \boldsymbol{N}\boldsymbol{k}\boldsymbol{\varepsilon_0}\,\mathrm{d}\Gamma^e + \omega^2 \int \rho\widehat{\boldsymbol{U}}^T \boldsymbol{u_0}\,\mathrm{d}V^e + \int \widehat{\boldsymbol{U}}^T \boldsymbol{b}\,\mathrm{d}V^e.\end{aligned} \tag{3.56}$$

The previous expression can then be substituted back into the left hand side of eq. (3.48). It turns out that all the terms involving domain integrals cancel each other on both sides and only integrals over the element boundary remain. This is a great advantage of Trefftz methods and a result of the specific requirements placed on the domain approximation basis $\boldsymbol{U}$ and the vector of

particular solution $\boldsymbol{u_0}$. The resulting equation develops as

$$\int \widehat{\boldsymbol{U}}^T \boldsymbol{N}\boldsymbol{k}\boldsymbol{E}\,\mathrm{d}\Gamma^e\,\boldsymbol{X} - \int \widehat{\boldsymbol{U}}^T \boldsymbol{Z}\,\mathrm{d}\Gamma_u^e\,\boldsymbol{p} = \int \widehat{\boldsymbol{U}}^T \boldsymbol{t_\Gamma}\,\mathrm{d}\Gamma_\sigma^e - \int \widehat{\boldsymbol{U}}^T \boldsymbol{N}\boldsymbol{k}\boldsymbol{\varepsilon_0}\,\mathrm{d}\Gamma^e. \tag{3.57}$$

Using definitions

$$\boldsymbol{D} = \int \widehat{\boldsymbol{U}}^T \boldsymbol{N}\boldsymbol{k}\boldsymbol{E}\,\mathrm{d}\Gamma^e, \tag{3.58}$$

$$\boldsymbol{B} = \int \widehat{\boldsymbol{U}}^T \boldsymbol{Z}\,\mathrm{d}\Gamma_u^e, \tag{3.59}$$

$$\overline{\boldsymbol{t_\Gamma}} = \int \widehat{\boldsymbol{U}}^T \boldsymbol{t_\Gamma}\,\mathrm{d}\Gamma_\sigma^e, \tag{3.60}$$

$$\overline{\boldsymbol{t_{\Gamma_0}}} = \int \widehat{\boldsymbol{U}}^T \boldsymbol{N}\boldsymbol{k}\boldsymbol{\varepsilon_0}\,\mathrm{d}\Gamma^e, \tag{3.61}$$

eq. (3.57) can be abbreviated to a compact form

$$\boldsymbol{D}\,\boldsymbol{X} - \boldsymbol{B}\,\boldsymbol{p} = \overline{\boldsymbol{t_\Gamma}} - \overline{\boldsymbol{t_{\Gamma_0}}}. \tag{3.62}$$

Note that in the previous equation the unknown quantities are collected in vectors $\boldsymbol{X}$ and $\boldsymbol{p}$ and all the other vectors and matrices are known and can be computed. It is worth the effort to check the dimensions of the individual matrices and vectors to compare the number of equations and the number of unknowns. One can show that the dimensions of matrix $\boldsymbol{D}$ are $2(2N+1) \times 2(2N+1)$, dimensions of matrix $\boldsymbol{B}$ are $2(2N+1)\times 2(M+1)$, dimensions of vectors $\boldsymbol{X}$ and $\boldsymbol{p}$ are $2(2N+1)\times 1$ and $2(M+1)\times 1$ respectively and dimensions of both vectors $\overline{\boldsymbol{t_\Gamma}}$ and $\overline{\boldsymbol{t_{\Gamma_0}}}$ are $2(2N+1)\times 1$. This indicates that eq. (3.62) represents a system of $2(2N+1)$ algebraic equations with $2(2N+1)+2(M+1)$ unknowns. Therefore, there are still $2(M+1)$ equations necessary so that the system can be solved. These are obtained by enforcement of displacement boundary conditions, which will be described in the following section.

3.4.3 Displacement Boundary Condition

The Dirichlet displacement boundary condition is as well enforced in a weak sense. The condition (2.36) is weighted by the matrix $\boldsymbol{Z}$ collecting the boundary approximation basis and integrated over the related portion of the boundary Γ_u^e

$$\int \boldsymbol{Z}^T\,(\boldsymbol{u} - \boldsymbol{u_\Gamma})\,\mathrm{d}\Gamma_u^e = \boldsymbol{0}. \tag{3.63}$$

Afterwards, the integral is split and the displacement approximation basis is inserted

$$\int \boldsymbol{Z}^T \boldsymbol{U}\,\mathrm{d}\Gamma_u^e\,\boldsymbol{X} = \int \boldsymbol{Z}^T \boldsymbol{u_\Gamma}\,\mathrm{d}\Gamma_u^e - \int \boldsymbol{Z}^T \boldsymbol{u_0}\,\mathrm{d}\Gamma_u^e. \tag{3.64}$$

Using definitions

$$\overline{\boldsymbol{u}_{\boldsymbol{\Gamma}}} = \int \boldsymbol{Z}^T \boldsymbol{u}_{\boldsymbol{\Gamma}} \, \mathrm{d}\Gamma_u^e, \tag{3.65}$$

$$\overline{\boldsymbol{u}_{\boldsymbol{\Gamma_0}}} = \int \boldsymbol{Z}^T \boldsymbol{u}_{\boldsymbol{0}} \, \mathrm{d}\Gamma_u^e \tag{3.66}$$

and already existing relation (3.59), eq. (3.64) can be rewritten in compact notation

$$-\widehat{\boldsymbol{B}}^T \boldsymbol{X} = \overline{\boldsymbol{u}_{\boldsymbol{\Gamma_0}}} - \overline{\boldsymbol{u}_{\boldsymbol{\Gamma}}}. \tag{3.67}$$

Eq. (3.67) represents $2(M+1)$ algebraic equations with $2(2N+1)$ unknown coefficients, which were however introduced already in the first matrix equation (3.62).

3.4.4 Governing System of Equations

Combining eqs. (3.62) and (3.67) results in the governing system of equations

$$\begin{bmatrix} \boldsymbol{D} & -\boldsymbol{B} \\ -\widehat{\boldsymbol{B}}^T & \boldsymbol{0} \end{bmatrix} \begin{bmatrix} \boldsymbol{X} \\ \boldsymbol{p} \end{bmatrix} = \begin{bmatrix} \overline{\boldsymbol{t}_{\boldsymbol{\Gamma}}} - \overline{\boldsymbol{t}_{\boldsymbol{\Gamma_0}}} \\ \overline{\boldsymbol{u}_{\boldsymbol{\Gamma_0}}} - \overline{\boldsymbol{u}_{\boldsymbol{\Gamma}}} \end{bmatrix}. \tag{3.68}$$

Based on the previous discussions, it can be concluded the system contains the same number of equations as unknowns. As the material matrix $\boldsymbol{k}$ is symmetric, the matrix $\boldsymbol{D}$ and the complete system (3.68) are Hermitian, which is an advantageous property when iterative solvers are applied.

The previous system was derived for a single element and assuming only one continuous boundary Γ_u^e and a single boundary Γ_σ^e. In the next section a generalization regarding the complexity of boundary conditions is introduced. To start with, one element is still assumed. Afterwards, continuity conditions are enforced and modelling using more elements is described.

3.4.5 Generalization: Multiple Boundary Conditions

Assume the Dirichlet boundary of a single element Γ_u^e is now partitioned into n_D nonoverlapping parts $\Gamma_{u_i}^e$, where $i = 1,2,\ldots,n_D$. Since only one element is still assumed, all the parts of the Dirichlet boundary are related to prescribed displacements, because no inter-element edges appear in such case. The displacement boundary condition is then expressed as

$$\boldsymbol{u} = \boldsymbol{u}_{\boldsymbol{\Gamma}i} \text{ on } \Gamma_{u_i}^e. \tag{3.69}$$

As was described in section 3.3, an independent traction approximation

$$\boldsymbol{t} = \boldsymbol{Z}\boldsymbol{p}_i \text{ on } \Gamma_{u_i}^e \tag{3.70}$$

is assumed on each of the related parts of the Dirichlet boundary.

Similarly, also the Neumann boundary is divided into n_N sections $\Gamma_{\sigma_j}^e$, where $j = 1,2,\ldots,n_N$.

The traction boundary condition then reads

$$\boldsymbol{t} = \boldsymbol{t}_{\boldsymbol{\Gamma}j} \text{ on } \Gamma^e_{\sigma_j}. \tag{3.71}$$

Most of the previous derivations remain valid, only some modifications need to be performed. The first difference can be spotted in eq. (3.47), where the integrals over the boundaries Γ^e_u and Γ^e_σ need to be split into the individual sub boundaries. In this sense the equation is modified as

$$\begin{aligned}\int \widehat{\boldsymbol{U}}^T \boldsymbol{\mathcal{D}}\boldsymbol{\sigma}\,\mathrm{d}V^e = \int \widehat{\boldsymbol{U}}^T \boldsymbol{t}_{\boldsymbol{\Gamma}1}\,\mathrm{d}\Gamma^e_{\sigma_1} + \cdots + \int \widehat{\boldsymbol{U}}^T \boldsymbol{t}_{\boldsymbol{\Gamma}n_N}\,\mathrm{d}\Gamma^e_{\sigma_{n_N}} + \\ + \int \widehat{\boldsymbol{U}}^T \boldsymbol{Z}\,\mathrm{d}\Gamma^e_{u_1}\,\boldsymbol{p}_1 + \cdots + \int \widehat{\boldsymbol{U}}^T \boldsymbol{Z}\,\mathrm{d}\Gamma^e_{u_{n_D}}\,\boldsymbol{p}_{n_D} \\ - \int \left(\boldsymbol{\mathcal{D}}^* \widehat{\boldsymbol{U}}\right)^T \boldsymbol{\sigma}\,\mathrm{d}V^e.\end{aligned} \tag{3.72}$$

This results in the modification of the first of the governing equations (3.62)

$$\boldsymbol{D}\,\boldsymbol{X} - \boldsymbol{B}_1\,\boldsymbol{p}_1 - \cdots - \boldsymbol{B}_{n_D}\,\boldsymbol{p}_{n_D} = \overline{\boldsymbol{t}_{\boldsymbol{\Gamma}}}_1 + \cdots + \overline{\boldsymbol{t}_{\boldsymbol{\Gamma}}}_{n_N} - \overline{\boldsymbol{t}_{\boldsymbol{\Gamma}_0}}, \tag{3.73}$$

where definitions

$$\overline{\boldsymbol{t}_{\boldsymbol{\Gamma}}}_j = \int \widehat{\boldsymbol{U}}^T \boldsymbol{t}_{\boldsymbol{\Gamma}j}\,\mathrm{d}\Gamma^e_{\sigma_j} \tag{3.74}$$

$$\boldsymbol{B}_i = \int \widehat{\boldsymbol{U}}^T \boldsymbol{Z}\,\mathrm{d}\Gamma^e_{u_i} \tag{3.75}$$

were used.

Another modification results from the fact that the displacement boundary condition needs to be imposed separately for each portion of the Dirichlet boundary $\Gamma^e_{u_i}$. Therefore, eq. (3.67) turns into n_D equations of the similar form

$$-\widehat{\boldsymbol{B}}_i^T\,\boldsymbol{X} = \overline{\boldsymbol{u}_{\boldsymbol{\Gamma}_0}}_i - \overline{\boldsymbol{u}_{\boldsymbol{\Gamma}}}_i \text{ for } i = 1,2,\ldots,n_D, \tag{3.76}$$

where

$$\overline{\boldsymbol{u}_{\boldsymbol{\Gamma}_0}}_i = \int \boldsymbol{Z}^T \boldsymbol{u}_{\boldsymbol{0}}\,\mathrm{d}\Gamma^e_{u_i}, \tag{3.77}$$

$$\overline{\boldsymbol{u}_{\boldsymbol{\Gamma}}}_i = \int \boldsymbol{Z}^T \boldsymbol{u}_{\boldsymbol{\Gamma}i}\,\mathrm{d}\Gamma^e_{u_i}. \tag{3.78}$$

The finite element governing system of equations (3.68) can be symbolically expressed in a very similar form

$$\begin{bmatrix} \boldsymbol{D} & -\boldsymbol{B}_g \\ -\widehat{\boldsymbol{B}_g}^T & \boldsymbol{0} \end{bmatrix} \begin{bmatrix} \boldsymbol{X} \\ \boldsymbol{p}_g \end{bmatrix} = \begin{bmatrix} \overline{\boldsymbol{t}_{\boldsymbol{\Gamma}}} - \overline{\boldsymbol{t}_{\boldsymbol{\Gamma}_0}} \\ \overline{\boldsymbol{u}_{\boldsymbol{\Gamma}_{0,g}}} - \overline{\boldsymbol{u}_{\boldsymbol{\Gamma}_g}} \end{bmatrix}, \tag{3.79}$$

where the global matrices are defined by

$$\boldsymbol{B_g} = \begin{bmatrix} \boldsymbol{B}_1 & \boldsymbol{B}_2 & \dots & \boldsymbol{B}_{n_D} \end{bmatrix}, \tag{3.80}$$

$$\boldsymbol{p_g} = \begin{bmatrix} \boldsymbol{p}_1^T & \boldsymbol{p}_2^T & \dots & \boldsymbol{p}_{n_D}^T \end{bmatrix}^T, \tag{3.81}$$

$$\overline{\boldsymbol{u}_{\boldsymbol{\Gamma}_g}} = \begin{bmatrix} \overline{\boldsymbol{u}_{\boldsymbol{\Gamma}}}_1^T & \overline{\boldsymbol{u}_{\boldsymbol{\Gamma}}}_2^T & \dots & \overline{\boldsymbol{u}_{\boldsymbol{\Gamma}}}_{n_D}^T \end{bmatrix}^T, \tag{3.82}$$

$$\overline{\boldsymbol{u}_{\boldsymbol{\Gamma}_{0,g}}} = \begin{bmatrix} \overline{\boldsymbol{u}_{\boldsymbol{\Gamma}_0}}_1^T & \overline{\boldsymbol{u}_{\boldsymbol{\Gamma}_0}}_2^T & \dots & \overline{\boldsymbol{u}_{\boldsymbol{\Gamma}_0}}_{n_D}^T \end{bmatrix}^T, \tag{3.83}$$

$$\overline{\boldsymbol{t}_{\boldsymbol{\Gamma}}} = \overline{\boldsymbol{t}_{\boldsymbol{\Gamma}}}_1 + \overline{\boldsymbol{t}_{\boldsymbol{\Gamma}}}_2 + \dots + \overline{\boldsymbol{t}_{\boldsymbol{\Gamma}}}_{n_N}. \tag{3.84}$$

Note that splitting the Neumann boundary into multiple sections was not necessary. The integral $\int \boldsymbol{U}^T \boldsymbol{t} \, \mathrm{d}\Gamma_\sigma^e$ was just split into n_N integrals which were computed separately and summed up afterwards, which is described by eq. (3.84). On the other hand, splitting the integral $\int \boldsymbol{U}^T \boldsymbol{t} \, \mathrm{d}\Gamma_u^e$ over the Dirichlet boundary into multiple integrals was crucial, since the tractions are approximated independently on each of these sub boundaries.

3.4.6 Generalization: Multiple Finite Elements

The procedure is now generalized for the case of more connected elements. Firstly, consider a hypothetical example where no connection between elements is introduced. For such case, the first matrix equation of the finite element system of equations (3.79) could be independently imposed for each element $i_{el} = 1,2,\dots,n_{el}$, where n_{el} is the number of finite elements. This can be expressed in matrix notation as

$$\begin{bmatrix} \boldsymbol{D_G} & -\boldsymbol{B'_G} \end{bmatrix} \begin{bmatrix} \boldsymbol{X_G} \\ \boldsymbol{p'_G} \end{bmatrix} = \begin{bmatrix} \overline{\boldsymbol{t}_{\boldsymbol{\Gamma}_G}} - \overline{\boldsymbol{t}_{\boldsymbol{\Gamma}_{0,G}}} \end{bmatrix}, \tag{3.85}$$

where relations

$$\boldsymbol{D_G} = \begin{bmatrix} \boldsymbol{D}^{(1)} & \mathbf{0} & \dots & \mathbf{0} \\ \mathbf{0} & \boldsymbol{D}^{(2)} & \dots & \mathbf{0} \\ \vdots & \vdots & \ddots & \mathbf{0} \\ \mathbf{0} & \mathbf{0} & \mathbf{0} & \boldsymbol{D}^{(n_{el})} \end{bmatrix}, \tag{3.86}$$

$$\boldsymbol{B'_G} = \begin{bmatrix} \boldsymbol{B_g}^{(1)} & \mathbf{0} & \dots & \mathbf{0} \\ \mathbf{0} & \boldsymbol{B_g}^{(2)} & \dots & \mathbf{0} \\ \vdots & \vdots & \ddots & \mathbf{0} \\ \mathbf{0} & \mathbf{0} & \mathbf{0} & \boldsymbol{B_g}^{(n_{el})} \end{bmatrix}, \tag{3.87}$$

$$\boldsymbol{p'_G} = \begin{bmatrix} \boldsymbol{p_g}^{(1)^T} & \boldsymbol{p_g}^{(2)^T} & \dots & \boldsymbol{p_g}^{(n_{el})^T} \end{bmatrix}^T, \tag{3.88}$$

$$\boldsymbol{X_G} = \begin{bmatrix} \boldsymbol{X}^{(1)^T} & \boldsymbol{X}^{(2)^T} & \dots & \boldsymbol{X}^{(n_{el})^T} \end{bmatrix}^T, \tag{3.89}$$

$$\overline{\boldsymbol{t_{\Gamma_G}}} = \begin{bmatrix} \overline{\boldsymbol{t_\Gamma}}^{(1)^T} & \overline{\boldsymbol{t_\Gamma}}^{(2)^T} & \dots & \overline{\boldsymbol{t_\Gamma}}^{(n_{el})^T} \end{bmatrix}^T, \tag{3.90}$$

$$\overline{\boldsymbol{t_{\Gamma_{0,G}}}} = \begin{bmatrix} \overline{\boldsymbol{t_{\Gamma_0}}}^{(1)^T} & \overline{\boldsymbol{t_{\Gamma_0}}}^{(2)^T} & \dots & \overline{\boldsymbol{t_{\Gamma_0}}}^{(n_{el})^T} \end{bmatrix}^T \tag{3.91}$$

hold. The superscript indicates belonging to a certain element. Note that some of the sub matrices of the individual $\boldsymbol{B_g}^{(i_{el})}$ matrices result from an integration over the inter-element part of the boundary Γ_u^e, since also on this portion the boundary the tractions are approximated.

Until this point, all the elements are separated and have no connection between each other. To correct this statement, one needs to consider the traction continuity requirement on the inter-element boundary. When an edge lies between two elements, the traction approximation is shared by both elements. This implies that the unknown $\boldsymbol{p}$ coefficients related to this inter-element edge are common for both elements. However, this was not considered in the above definition. The way $\boldsymbol{p'_G}$ vector was defined, it contains some additional unknowns, since for the inter-element edges the unknown $\boldsymbol{p}$ vector related to that edge is contained in more $\boldsymbol{p_g}^{(i_{el})}$ vectors.

Discussion made in the previous paragraph is now explained in more detail. Assume all the inter-element edges are labelled with index $h = 1,2,\dots,n_I$, where n_I stands for the overall number of inter-element edges. For every h there is a pair of adjacent elements k and l sharing the common edge. The traction continuity

$$\boldsymbol{t}^{(k)} + \boldsymbol{t}^{(l)} = \mathbf{0} \text{ on } \Gamma_{u_h}^e \tag{3.92}$$

between the two elements is strongly satisfied. Substituting the traction approximation and manipulating the expression, the previous equation results in

$$\begin{aligned} \boldsymbol{Z}\boldsymbol{p}_h^{(k)} + \boldsymbol{Z}\boldsymbol{p}_h^{(l)} &= \mathbf{0} \\ \boldsymbol{Z}(\boldsymbol{p}_h^{(k)} + \boldsymbol{p}_h^{(l)}) &= \mathbf{0}. \end{aligned} \tag{3.93}$$

From eq. (3.93) the relation

$$\boldsymbol{p}_h^{(k)} = -\boldsymbol{p}_h^{(l)} \tag{3.94}$$

between the vectors of generalized tractions can be deduced.

The previous formula can be substituted into definitions of the individual $\boldsymbol{p}_{\boldsymbol{g}}^{(i_{el})}$ vectors contained in eq. (3.88). As a consequence, the number of unknown generalized tractions is reduced and the $\boldsymbol{B}'_{\boldsymbol{G}}$ matrix is modified. In the end, the individual $\boldsymbol{B}$ matrices related to the common edge will appear in the same column in the global matrix $\boldsymbol{B}'_{\boldsymbol{G}}$, however, with different sign. As a result, the block-diagonal structure of $\boldsymbol{B}'_{\boldsymbol{G}}$ is lost, which makes the system of equations coupled.

So far only the first equation of the complete finite element system of equations was discussed for the case of multiple elements. The second equation results from an imposition of the displacement boundary condition, which could be performed in a similar manner as was discussed in section 3.4.5. However, this will not generate final system with enough equations as unknowns. The reason is that these equations are by definition only enforced on the outer part of the Dirichlet boundary Γ_u^e, where the displacement boundary condition is prescribed, not on the inter-element edges. On the other hand, as was discussed in the first part of this subsection, in the first equation (3.85), there appear unknown vectors $\boldsymbol{p}$ and matrices $\boldsymbol{B}$ which result from an integration over the inter-element boundary. To counteract this mismatch, the displacement continuity condition needs to be enforced additionally.

Displacement Inter-element Continuity Condition

Again assume h is an index running over the inter-element edges and superscripts k and l represent two neighbouring elements to that edge. The displacement inter-element continuity equation

$$\boldsymbol{u}^{(k)} - \boldsymbol{u}^{(l)} = \boldsymbol{0} \text{ on } \Gamma_{u_h}^e \tag{3.95}$$

between these two elements is weakly imposed in a similar way as the Dirichlet boundary condition. Also it this case the boundary traction basis is used as a weighting matrix, however, this time the product is integrated over the inter-element part of the boundary only

$$\int \boldsymbol{Z}^T \left(\boldsymbol{u}^{(k)} - \boldsymbol{u}^{(l)}\right) \mathrm{d}\Gamma_{u_h}^e = \boldsymbol{0}. \tag{3.96}$$

Introducing the displacement approximation, the previous equation is modified

$$\int \boldsymbol{Z}^T \boldsymbol{U}^{(k)} \,\mathrm{d}\Gamma_{u_h}^e \, \boldsymbol{X}^{(k)} - \int \boldsymbol{Z}^T \boldsymbol{U}^{(l)} \,\mathrm{d}\Gamma_{u_h}^e \, \boldsymbol{X}^{(l)} = \int \boldsymbol{Z}^T \boldsymbol{u}_{\boldsymbol{0}}^{(l)} \,\mathrm{d}\Gamma_{u_h}^e - \int \boldsymbol{Z}^T \boldsymbol{u}_{\boldsymbol{0}}^{(k)} \,\mathrm{d}\Gamma_{u_h}^e. \tag{3.97}$$

Using the already stated definitions, eq. (3.97) can be abbreviated as

$$\widehat{\boldsymbol{B}_h^{(k)}}^T \boldsymbol{X}^{(k)} - \widehat{\boldsymbol{B}_h^{(l)}}^T \boldsymbol{X}^{(l)} = \overline{\boldsymbol{u}_{\boldsymbol{\Gamma_0}}}_h^{(l)} - \overline{\boldsymbol{u}_{\boldsymbol{\Gamma_0}}}_h^{(k)}. \tag{3.98}$$

Eq. (3.98) needs to hold for every inter-element edge h.

For completeness, also the equations (3.76) resulting from an imposition of the displacement boundary condition are introduced once more with slight modification. For every element $i_{el} = 1,2,\ldots,n_{el}$ there are $n_D^{(i_{el})}$ prescribed displacement boundary conditions, therefore, equation

$$-\widehat{\boldsymbol{B}_i^{(i_{el})}}^T \boldsymbol{X}^{(i_{el})} = \overline{\boldsymbol{u}_{\boldsymbol{\Gamma}_0}}_i^{(i_{el})} - \overline{\boldsymbol{u}_{\boldsymbol{\Gamma}}}_i^{(i_{el})} \text{ for } i = 1,2,\ldots,n_D^{(i_{el})}. \tag{3.99}$$

must hold for every i_{el} and i (i being the index running over individual displacement boundary conditions within element).

Complete Governing System of Equations

Finally, the complete governing system of equations can be formed. Modified eq. (3.85) is combined with eqs. (3.98) and (3.99), resulting in

$$\begin{bmatrix} \boldsymbol{D_G} & -\boldsymbol{B_G} \\ -\widehat{\boldsymbol{B_G}}^T & \boldsymbol{0} \end{bmatrix} \begin{bmatrix} \boldsymbol{X_G} \\ \boldsymbol{p_G} \end{bmatrix} = \begin{bmatrix} \overline{\boldsymbol{t}_{\boldsymbol{\Gamma_G}}} - \overline{\boldsymbol{t}_{\boldsymbol{\Gamma}_{\mathbf{0},\boldsymbol{G}}}} \\ \overline{\boldsymbol{u}_{\boldsymbol{\Gamma_G}}} \end{bmatrix}. \tag{3.100}$$

Definitions (3.86), (3.89), (3.90) and (3.91) for $\boldsymbol{D_G}$, $\boldsymbol{X_G}$, $\overline{\boldsymbol{t}_{\boldsymbol{\Gamma_G}}}$ and $\overline{\boldsymbol{t}_{\boldsymbol{\Gamma}_{\mathbf{0},\boldsymbol{G}}}}$, respectively, remain still valid. Defining the $\boldsymbol{B_G}$ matrix for a general case is rather complex task, therefore, guidelines of the construction will be provided instead.

Consider a general matrix $\boldsymbol{B}_i^{(j)}$ evaluated at an edge i and belonging to an element j. The matrices are evaluated at all Dirichlet edges, including both outer edges where displacement boundary condition is applied as well as the inter-element edges. Note that if the edge is an inter-element one, two matrices are evaluated, sharing the same index i but differing with index j. The individual matrices $\boldsymbol{B}_i^{(j)}$ are ordered in the following way into the complete $\boldsymbol{B_G}$ matrix: j index corresponds to the row in which the matrix is located and the i index corresponds to the column. Therefore, in the case of an inter-element edge, individual matrices will be located in the same column, since both share the same index i, however, both will appear in a different row since the element index j varies. What is more, to fulfil the continuity condition (3.98), the sign of both matrices need to be opposite.

The formation of the global vector of generalized tractions $\boldsymbol{p_G}$ can be explained in a similar manner. As was discussed in the previous sections, for every Dirichlet edge i (including the inter-element edges) there exists an associated vector of unknown generalized tractions $\boldsymbol{p}_i$. The index i corresponds to the row in the global vector of generalized tractions $\boldsymbol{p_G}$.

The last undefined quantity is the vector $\overline{\boldsymbol{u}_{\boldsymbol{\Gamma_G}}}$. It needs to collect the right hand sides of eqs. (3.98) and (3.99). If the edge of interest i is part of the Dirichlet boundary where the displacement boundary condition is applied, the component of the vector $\overline{\boldsymbol{u}_{\boldsymbol{\Gamma_G}}}$ at position i will be the right hand side of eq. (3.99), meaning term

$$\overline{\boldsymbol{u}_{\boldsymbol{\Gamma}_0}}_i^{(j)} - \overline{\boldsymbol{u}_{\boldsymbol{\Gamma}}}_i^{(j)}.$$

On the other hand, if the edge i is part of the inter-element boundary, the ith component of the

global vector $\overline{\boldsymbol{u}_{\boldsymbol{\Gamma}_{\boldsymbol{G}}}}$ is the right hand side of eq. (3.98), that is

$$\overline{\boldsymbol{u}_{\boldsymbol{\Gamma}_{\mathbf{0}}}}_i^{(l)} - \overline{\boldsymbol{u}_{\boldsymbol{\Gamma}_{\mathbf{0}}}}_i^{(k)},$$

where $k \subset j$ and $l \subset j$ are the adjacent elements to the common edge i.

In the following, some comments regarding the number of equations and unknowns in the system (3.100) are made. The unknown generalized displacements are collected in global vector $\boldsymbol{X}_{\boldsymbol{G}}$. The individual unknown vectors $\boldsymbol{X}^{(i_{el})}$ corresponding to each element are strictly element dependent, therefore the matrix $\boldsymbol{D}_{\boldsymbol{G}}$ preserves the block diagonal structure. Following the discussion from the previous sections, for each element, there are $2(2N+1)$ unknown coefficients collected in vector $\boldsymbol{X}^{(i_{el})}$, where N is the maximum degree of p-refinement. Therefore, for all elements the overall number of displacement degrees of freedom is $2n_{el}(2N+1)$.

From the previous derivations it turned out that the length of the global vector of unknown generalized tractions $\boldsymbol{p}_{\boldsymbol{G}}$, and therefore the number of related static degrees of freedom, is proportional to the overall number of Dirichlet edges rather then to number of elements. In addition, as was also stated before, tractions on each edge belonging to the Dirichlet boundary are approximated separately. Each vector $\boldsymbol{p}_i$ stores $2(M+1)$ unknown coefficients, which indicates that the overall number of unknown generalized tractions is $2n_D(M+1)$, with n_D being the number of Dirichlet edges and M the maximum polynomial order of the boundary approximation basis.

The single matrix $\boldsymbol{D}^{(i_{el})}$ is of size $2(2N+1) \times 2(2N+1)$. Due to the block diagonal structure of the global matrix, size of $\boldsymbol{D}_{\boldsymbol{G}}$ is therefore $2n_{el}(2N+1) \times 2n_{el}(2N+1)$. Furthermore, dimensions of the single $\boldsymbol{B}_i$ matrix are $2(2N+1) \times 2(M+1)$. Following the guidelines for construction of the global matrix $\boldsymbol{B}_{\boldsymbol{G}}$, its size results $2n_{el}(2N+1) \times 2n_D(M+1)$. To conclude, there is the same number of equations as number of unknown components in the final finite element system of equations.

3.4.7 Mixed Boundary Conditions

Until this point it was assumed that the boundary conditions were strictly of displacement or traction character, respectively. It means that both of the components of the related fields were assumed to be prescribed simultaneously on the corresponding portion of the boundary. However, to simulate wider range of problems, it is desired to model also mixed type of boundary conditions, where certain displacement component is prescribed while the other one is unknown. To be more precise, mixed boundary condition means that on a certain portion of boundary Γ_m, displacement component is prescribed in a certain direction, while in the perpendicular direction a traction component is given. The modification of the system equations is described for the case of a single element with a single Dirichlet boundary. This set up is modified and a continuous mixed boundary Γ_m^e is added. A generalization for multiple elements is straightforward. To start with, simplified situation where the prescribed components are strictly in x or y direction is considered. An example of such support can be horizontal or vertical sliders. Afterwards, a more general case, in which the components tangential and normal to the boundary are prescribed, is investigated.

Simplified Case

Firstly, assume that components u and t_y are prescribed on Γ_m^e. The opposite case can be directly deduced from the following one. The mixed boundary condition then reads

$$\begin{aligned} u =& u_\Gamma, \\ t_y =& t_{\Gamma,y}. \end{aligned} \quad \text{on } \Gamma_m^e \tag{3.101}$$

First modification arises in eq. (3.47), where also integral over the mixed boundary pops up

$$\int \widehat{\boldsymbol{U}}^T \boldsymbol{\mathcal{D}\sigma}\, \mathrm{d}V^e = \int \widehat{\boldsymbol{U}}^T \boldsymbol{t_\Gamma}\, \mathrm{d}\Gamma_\sigma^e + \int \widehat{\boldsymbol{U}}^T \boldsymbol{Z}\, \mathrm{d}\Gamma_u^e\, \boldsymbol{p} + \int \widehat{\boldsymbol{U}}^T \boldsymbol{t}\, \mathrm{d}\Gamma_m^e - \int \left(\boldsymbol{\mathcal{D}}^* \widehat{\boldsymbol{U}}\right)^T \boldsymbol{\sigma}\, \mathrm{d}V^e. \tag{3.102}$$

The displacement basis consists of two rows

$$\boldsymbol{U} = \begin{bmatrix} \boldsymbol{U_x}^T & \boldsymbol{U_y}^T \end{bmatrix}^T,$$

each approximating one displacement component. The size of vectors $\boldsymbol{U_x}$ and $\boldsymbol{U_y}$ is $1 \times 2(2N+1)$. Furthermore, the traction vector $\boldsymbol{t}$ on the mixed boundary Γ_m^e has components

$$\boldsymbol{t} = \begin{bmatrix} t_x & t_y \end{bmatrix}^T = \begin{bmatrix} t_x & t_{\Gamma,y} \end{bmatrix}^T,$$

where the traction part of the boundary condition (3.101) was inserted. The complete traction approximation was introduced in eq. (3.36).

In section 3.3 it was also mentioned that the individual traction components are approximated independently and can be expressed by relations (3.41) and (3.42). As a reminder, they are also reproduced here

$$t_x = \boldsymbol{Z_v p_x}, \tag{3.103}$$

$$t_y = \boldsymbol{Z_v p_y}. \tag{3.104}$$

Using the provided equations, the integral over the mixed boundary appearing in eq. (3.102) can be reformulated

$$\int \widehat{\boldsymbol{U}}^T \boldsymbol{t}\, \mathrm{d}\Gamma_m^e = \int \widehat{\boldsymbol{U_x}}^T t_x\, \mathrm{d}\Gamma_m^e + \int \widehat{\boldsymbol{U_y}}^T t_{\Gamma,y}\, \mathrm{d}\Gamma_m^e = \int \widehat{\boldsymbol{U_x}}^T \boldsymbol{Z_v}\, \mathrm{d}\Gamma_m^e\, \boldsymbol{p_x} + \int t_{\Gamma,y} \widehat{\boldsymbol{U_y}}^T\, \mathrm{d}\Gamma_m^e. \tag{3.105}$$

Therefore, the first equation of the governing system of equations (3.57) results in

$$\begin{aligned} \int \widehat{\boldsymbol{U}}^T \boldsymbol{NkE}\, \mathrm{d}\Gamma^e\, \boldsymbol{X} - \int \widehat{\boldsymbol{U}}^T \boldsymbol{Z}\, \mathrm{d}\Gamma_u^e\, \boldsymbol{p} - \int \widehat{\boldsymbol{U_x}}^T \boldsymbol{Z_v}\, \mathrm{d}\Gamma_m^e\, \boldsymbol{p_m} = \int \widehat{\boldsymbol{U}}^T \boldsymbol{t_\Gamma}\, \mathrm{d}\Gamma_\sigma^e + \\ - \int \widehat{\boldsymbol{U}}^T \boldsymbol{N k \varepsilon_0}\, \mathrm{d}\Gamma^e + \int t_{\Gamma,y} \widehat{\boldsymbol{U_y}}^T\, \mathrm{d}\Gamma_m^e. \end{aligned} \tag{3.106}$$

The symbol for the the unknown vector $\boldsymbol{p_x}$ was replaced with $\boldsymbol{p_m}$ to stress the belonging to the

mixed boundary condition. In an abbreviated notation the previous equation reads

$$\boldsymbol{D}\,\boldsymbol{X} - \boldsymbol{B}\,\boldsymbol{p} - \boldsymbol{B_m}\,\boldsymbol{p_m} = \overline{\boldsymbol{t_\Gamma}} - \overline{\boldsymbol{t_{\Gamma_0}}} + \overline{\boldsymbol{t_{\Gamma m}}}, \tag{3.107}$$

where

$$\boldsymbol{B_m} = \int \widehat{\boldsymbol{U_x}}^T \boldsymbol{Z_v}\,\mathrm{d}\Gamma_m^e \tag{3.108}$$

$$\overline{\boldsymbol{t_{\Gamma m}}} = \int t_{\Gamma,y}\widehat{\boldsymbol{U_y}}^T\,\mathrm{d}\Gamma_m^e. \tag{3.109}$$

Note that the dimensions of the matrix $\boldsymbol{B_m}$ are $2(2N+1)\times(M+1)$ and the length of the vector of unknown generalized tractions related to the mixed boundary condition is $(M+1)$. This implies that the number of unknown coefficients related to the mixed boundary condition is half of the unknowns of the usual displacement boundary, since only tractions in one direction need to be approximated.

To obtain a solvable system, besides the standard displacement boundary condition also the displacement part related to the mixed boundary condition (3.101) needs to be imposed. Since the condition is enforced for a single component, only the related part of the basis $\boldsymbol{Z}$ is used as the weighting function. Following the discussion in the first part of this subsection the basis of interest is $\boldsymbol{Z_v}$. The weakly imposed equation reads

$$\int \boldsymbol{Z_v}^T\,(u_x - u_\Gamma)\,\mathrm{d}\Gamma_m^e = \boldsymbol{0}. \tag{3.110}$$

The displacement approximation of the single component

$$u_x = \boldsymbol{U_x}\boldsymbol{X} + u_{0,x}$$

is inserted into eq. (3.110) and the expression is rearranged

$$-\int \boldsymbol{Z_v}^T\boldsymbol{U_x}\,\mathrm{d}\Gamma_m^e\,\boldsymbol{X} = \int \boldsymbol{Z_v}^T u_{0,x}\,\mathrm{d}\Gamma_m^e - \int \boldsymbol{Z_v}^T u_\Gamma\,\mathrm{d}\Gamma_m^e. \tag{3.111}$$

Symbol $u_{0,x}$ denotes the component of the vector of particular solutions $\boldsymbol{u_0}$. Using the stated definitions and relations

$$\overline{\boldsymbol{u_{\Gamma m_0}}} = \int \boldsymbol{Z_v}^T u_{0,x}\,\mathrm{d}\Gamma_m^e \tag{3.112}$$

$$\overline{\boldsymbol{u_{\Gamma m}}} = \int \boldsymbol{Z_v}^T u_\Gamma\,\mathrm{d}\Gamma_m^e, \tag{3.113}$$

eq. (3.111) can be written in compact notation

$$-\widehat{\boldsymbol{B_m}}^T\,\boldsymbol{X} = \overline{\boldsymbol{u_{\Gamma m_0}}} - \overline{\boldsymbol{u_{\Gamma m}}}. \tag{3.114}$$

Equations (3.107) and (3.114) combined with the displacement boundary condition, expressed by eq. (3.67), form the set of equations describing the problem of mixed boundary condition. In the

case when the prescribed components are v and t_x the only differences are that in definitions (3.108) and (3.109) $\boldsymbol{U_y}$ is used instead of $\boldsymbol{U_x}$ and vice versa, in eq. (3.112) $u_{0,x}$ is replaced by $u_{0,y}$ and in eq. (3.113) u_Γ is replaced by v_Γ.

A generalization for the case of multiple boundary conditions and multiple elements can be derived in a similar way as before. Edges belonging to the mixed boundary Γ_m^e are in a way treated as both Dirichlet and Neumann ones. In the procedure of assembling of the $\boldsymbol{B_G}$ matrix, individual $\boldsymbol{B}_i^{(j)}$ matrices are ordered into the global one. If the edge i belongs to the mixed boundary, $\boldsymbol{B}_i^{(j)}$ is only replaced by $\boldsymbol{B}_{\boldsymbol{m}_i}^{(j)}$. Similarly, in such case a component of the global $\boldsymbol{p_G}$ vector is replaced by $\boldsymbol{p}_{\boldsymbol{m}i}$ and the component of the vector $\overline{\boldsymbol{u}_{\boldsymbol{\Gamma_G}}}$ is changed to $\overline{\boldsymbol{u}_{\boldsymbol{\Gamma m_0}i}} - \overline{\boldsymbol{u}_{\boldsymbol{\Gamma m}i}}$. Formation of the global vector $\overline{\boldsymbol{t}_{\boldsymbol{\Gamma_G}}}$ is described by eqs. (3.90) and (3.84). Modification appears only in the latter one, where vector $\overline{\boldsymbol{t}_{\boldsymbol{\Gamma m}i}}$ needs to be added for every mixed boundary.

General Case

As a general case of the mixed boundary condition it is assumed that the displacement component is prescribed in the direction normal to the boundary and the traction component is given in the tangential direction or vice versa. This formulation allows to consider meaningful mixed boundaries of arbitrary curved shape. An example of such boundary can be fixed zero displacement in normal direction and zero tractions in the tangential direction, a slider of arbitrary shape.

On the boundary of the domain, the Cartesian components of the displacement and traction vectors can be transformed into components normal and tangential to the boundary. The transformed vectors $\boldsymbol{u'} = \begin{bmatrix} u_n & u_t \end{bmatrix}^T$ and $\boldsymbol{t'} = \begin{bmatrix} t_n & t_t \end{bmatrix}^T$ are obtained as

$$\boldsymbol{u'} = \boldsymbol{T}^T \boldsymbol{u}, \tag{3.115}$$

$$\boldsymbol{t'} = \boldsymbol{T}^T \boldsymbol{t}, \tag{3.116}$$

where

$$\boldsymbol{T} = \begin{bmatrix} \cos\alpha & -\sin\alpha \\ \sin\alpha & \cos\alpha \end{bmatrix} \tag{3.117}$$

is the transformation matrix and α is the angle between x axis and the normal vector to the boundary. Due to the orthogonality of the $\boldsymbol{T}$ matrix, the inverse transformation reads

$$\boldsymbol{u} = \boldsymbol{T}\boldsymbol{u'}, \tag{3.118}$$

$$\boldsymbol{t} = \boldsymbol{T}\boldsymbol{t'}. \tag{3.119}$$

For further development it is worth the effort to substitute the displacement approximation (3.1) into eq. (3.115)

$$\boldsymbol{u'} = \boldsymbol{T}^T\boldsymbol{u} = \boldsymbol{T}^T\boldsymbol{U}\boldsymbol{X} + \boldsymbol{T}^T\boldsymbol{u_0} = \boldsymbol{U'}\boldsymbol{X} + \boldsymbol{u'_0}. \tag{3.120}$$

Matrix $\boldsymbol{U'} = \boldsymbol{T}^T\boldsymbol{U}$ can be viewed as the approximation basis of the displacements normal and

tangential to the boundary and vector $\boldsymbol{u_0'} = \boldsymbol{T}^T\boldsymbol{u_0}$ as the particular solution for the body forces expressed in normal and tangential components. Similarly as was discussed in the previous section, also basis $\boldsymbol{U'}$ consists of two rows

$$\boldsymbol{U'} = \begin{bmatrix} \boldsymbol{U_n'}^T & \boldsymbol{U_t'}^T \end{bmatrix}^T,$$

each approximating the normal or the tangential displacement components respectively.

The boundary condition for the general case is then expressed as

$$\begin{aligned} u_n &= u_{\Gamma,n}, \\ t_t &= t_{\Gamma,t}. \end{aligned} \quad \text{on } \Gamma_m^e \tag{3.121}$$

The key concept is that on the mixed boundary of this type, normal and tangential tractions are approximated instead of the tractions in Cartesian directions. Therefore, the traction approximation is modified for the mixed boundary and reads as

$$\boldsymbol{t'} = \boldsymbol{Z}\boldsymbol{p} \text{ on } \Gamma_m^e. \tag{3.122}$$

All the properties and form of the basis $\boldsymbol{Z}$ remain unchanged, therefore also in this case, individual components can be expressed independently as $\boldsymbol{Z_v}\boldsymbol{p_m}$. Using the previously stated relations, the integral over the mixed boundary popping up in eq. (3.102) can be reformulated

$$\int \widehat{\boldsymbol{U}}^T\boldsymbol{t}\,\mathrm{d}\Gamma_m^e = \int \widehat{\boldsymbol{U}}^T\boldsymbol{T}\boldsymbol{t'}\,\mathrm{d}\Gamma_m^e = \int \widehat{\boldsymbol{U'}}^T\boldsymbol{t'}\,\mathrm{d}\Gamma_m^e = \int \widehat{\boldsymbol{U_n'}}^T t_n\,\mathrm{d}\Gamma_m^e + \int \widehat{\boldsymbol{U_t'}}^T t_t\,\mathrm{d}\Gamma_m^e. \tag{3.123}$$

Furthermore, the traction part of the boundary condition (3.121) and the approximation of the normal traction component is inserted

$$\int \widehat{\boldsymbol{U_n'}}^T t_n\,\mathrm{d}\Gamma_m^e + \int \widehat{\boldsymbol{U_t'}}^T t_t\,\mathrm{d}\Gamma_m^e = \int \widehat{\boldsymbol{U_n'}}^T\boldsymbol{Z_v}\,\mathrm{d}\Gamma_m^e\,\boldsymbol{p_m} + \int t_{\Gamma,t}\widehat{\boldsymbol{U_t'}}^T\,\mathrm{d}\Gamma_m^e. \tag{3.124}$$

Defining

$$\boldsymbol{B_m'} = \int \widehat{\boldsymbol{U_n'}}^T\boldsymbol{Z_v}\,\mathrm{d}\Gamma_m^e, \tag{3.125}$$

$$\overline{\boldsymbol{t_{\Gamma m}'}} = \int t_{\Gamma,t}\widehat{\boldsymbol{U_t'}}^T\,\mathrm{d}\Gamma_m^e, \tag{3.126}$$

eq. (3.107) is modified as

$$\boldsymbol{D}\,\boldsymbol{X} - \boldsymbol{B}\,\boldsymbol{p} - \boldsymbol{B_m'}\,\boldsymbol{p_m} = \overline{\boldsymbol{t_\Gamma}} - \overline{\boldsymbol{t_{\Gamma_0}}} + \overline{\boldsymbol{t_{\Gamma m}'}}. \tag{3.127}$$

In the following, the displacement part of the boundary condition (3.121) is imposed. As it contains only one component, vector $\boldsymbol{Z_v}$ is used as the weighting function

$$\int \boldsymbol{Z_v}^T\,(u_n - u_{\Gamma,n})\,\mathrm{d}\Gamma_m^e = \boldsymbol{0}. \tag{3.128}$$

The normal component of the displacement vector can now be expressed as

$$u_n = \boldsymbol{U'_n} \boldsymbol{X} + u'_{0,n},$$

where $u'_{0,n}$ is the normal component of the vector of particular solution $\boldsymbol{u'_0}$. Substituting the previous definition into eq. (3.128) yields

$$-\int \boldsymbol{Z_v^T U'_n} \, \mathrm{d}\Gamma_m^e \, \boldsymbol{X} = \int \boldsymbol{Z_v^T} u'_{0,n} \, \mathrm{d}\Gamma_m^e - \int \boldsymbol{Z_v^T} u_{\Gamma,n} \, \mathrm{d}\Gamma_m^e. \tag{3.129}$$

Using the abbreviations

$$\overline{\boldsymbol{u'_{\Gamma m}}} = \int \boldsymbol{Z_v^T} u_{\Gamma,n} \, \mathrm{d}\Gamma_m^e, \tag{3.130}$$

$$\overline{\boldsymbol{u'_{\Gamma m_0}}} = \int \boldsymbol{Z_v^T} u'_{0,n} \, \mathrm{d}\Gamma_m^e \tag{3.131}$$

and already mentioned definitions, eq. (3.129) can be reformulated as

$$-\widehat{\boldsymbol{B'_m}}^T \boldsymbol{X} = \overline{\boldsymbol{u'_{\Gamma m_0}}} - \overline{\boldsymbol{u'_{\Gamma m}}}. \tag{3.132}$$

Comparing the final equations (3.127) and (3.132) of the general case with eqs. (3.107) and (3.114) derived for the simplified one, the only difference arises in definitions of the matrix $\boldsymbol{B'_m}$ and vectors $\overline{\boldsymbol{t'_{\Gamma m}}}$, $\overline{\boldsymbol{u'_{\Gamma m}}}$ and $\overline{\boldsymbol{u'_{\Gamma m_0}}}$. For the general case, the rows of the displacement approximation basis and of the vector of particular solution are transformed into the normal and tangential components. One also needs to keep in mind that on the mixed boundary, normal and tangential tractions are approximated instead of the original traction vector in Cartesian coordinates. The procedure of generalization for the case, when multiple elements are used, is completely the same as for the simplified case.

3.5 Post-processing

In the previous section the finite element system of algebraic equations (3.100) was derived. The unknown coefficients related to the domain displacement and boundary traction approximations are collected in vectors $\boldsymbol{X_G}$ and $\boldsymbol{p_G}$, respectively. As both approximation bases are hierarchical, the coefficients no longer have the meaning of nodal values of the corresponding field. After the system is solved, a post-processing phase is necessary so that the displacement, stress and strain fields are recovered.

Firstly, coefficients $\boldsymbol{X}^{(i_{el})}$ for each element i_{el} are extracted from the global vector $\boldsymbol{X_G}$. Afterwards, the displacement field evaluated at a certain position (x,y) within element i_{el} is obtained with the use of eq. (3.1). The basis functions collected in $\boldsymbol{U}(x,y)$ and vector of particular solution $\boldsymbol{u_0}(x,y)$ are also evaluated at position (x,y).

The strain field is evaluated in a similar way. The coefficients $\boldsymbol{X}^{(i_{el})}$ are plugged into eq. (3.4), where the approximation of the strain field is introduced. Again, the basis $\boldsymbol{E}(x,y)$ and vector

$\boldsymbol{\varepsilon_0}(x,y)$ are evaluated at the desired location (x,y). The stress field is then obtained by application of eq. (2.34), which means that the previously evaluated strain field is just multiplied by the material matrix $\boldsymbol{k}$.

The tractions on the boundary are computed based on the boundary equilibrium (2.35). This indicates that firstly, the stress field at the location $(x,y) \in \Gamma^{i_{el}}$ is evaluated as was discussed in the previous paragraph. Subsequently, the matrix of unit normals $\boldsymbol{N}(x,y)$ at the investigated location at the boundary is computed and inserted into eq. (2.35). Note that the boundary tractions are not evaluated based on the boundary traction approximation stated in eq. (3.36). Therefore, the coefficients collected in vector $\boldsymbol{p_G}$ are not directly used in the post-processing phase. However, eq. (3.36) can serve as a measure of quality of the results. On the Dirichlet boundary $\Gamma_u^{i_{el}}$, the boundary tractions can be evaluated using both the domain stress field as well as the boundary traction approximation basis and compared afterwards.

The previous section concludes the chapter dedicated to the hybrid-Trefftz method. As the basis functions are required to satisfy the homogeneous governing differential equation, the submatrices and subvectors appearing in the final system of equations are computed based on integrals over the element boundary. Therefore, on the element level the dimensionality of the problem is reduced, which makes the integration procedure computationally faster. This property also enables usage of elements with arbitrary shape and number of edges. Both domain and boundary approximation bases are constructed hierarchically, therefore an optional number of terms can be included in the individual bases. Combination of both previous properties allows modelling using very few but rich elements.

4 Unbounded Media

In many practical situations the domain of the investigated problem may be very large, in some cases it may even extend to infinity. An often considered example of such structure is a loaded half space. Applying the so far explained method, it is not possible to model an infinite structure. Therefore the domain must be truncated at a certain distance from the source and artificial boundary conditions need to be introduced. However, such approach would result in spurious reflections of the travelling waves and consequently in a meaningless solution. To limit such undesired behaviour, few techniques [Tsynkov 1998] were developed so that the analysis of unbounded media can be performed. These consist of e.g. modelling using infinite elements or introduction of absorbing boundary condition.

It was briefly mentioned in section 3.2 that if the Hankel function is chosen as the radial component W_n of the solution of the underlying Helmholtz equation, not only that the resulting displacement basis satisfies the governing differential equation but also the Sommerfeld radiation condition is implicitly fulfilled. This property is a key concept in both of the aformentioned methods. In the case infinite elements are used, the principle is that the displacement approximation basis is constructed using the Hankel functions as the radial component W_n. This ensures the Sommerfeld radiation condition is satisfied. As a consequence of such formulation, integrals over a boundary placed at infinite distance from the origin need to be computed, which however can be performed analytically. In this thesis only the absorbing boundary condition was investigated and implemented, therefore, details regarding the infinite elements are not discussed any more.

Various techniques regarding the formulation of the absorbing boundary condition were developed over the years. The one applied in this thesis in referred to as the Dirichlet-to-Neumann mapping method [Keller and Givoli 1989]. It can be shown that if the displacement basis functions satisfy the Sommerfeld radiation condition, a linear mapping between the displacement and traction vectors exists at infinite distance from the source. The essence of absorbing boundary condition is to enforce such relation at a finite distance. In such case, the previous imposition results in an approximation. An advantage of this approach is that any of the solution of the Bessel equation can be adopted for the radial component W_n. In the following sections the procedure is described in detail.

4.1 Domain Modification

Assume the structure to be analysed is a loaded quarter-space depicted in fig. 4.1. As can be seen, the domain extends to infinity in the direction of positive x-axis and negative y-axis. When the absorbing boundary condition is applied for the analysis of unbounded medium, the domain is divided into an internal region V and an external part V_{ext}. All the loading and geometrical

irregularities need to be placed in the internal region. The external domain is discarded from the analysis and only the internal sector is considered. The borderline between the sectors is named absorbing boundary on which the absorbing boundary condition is imposed. The rest of the boundary of the internal domain is partitioned in the same way as was described in the previous chapters.

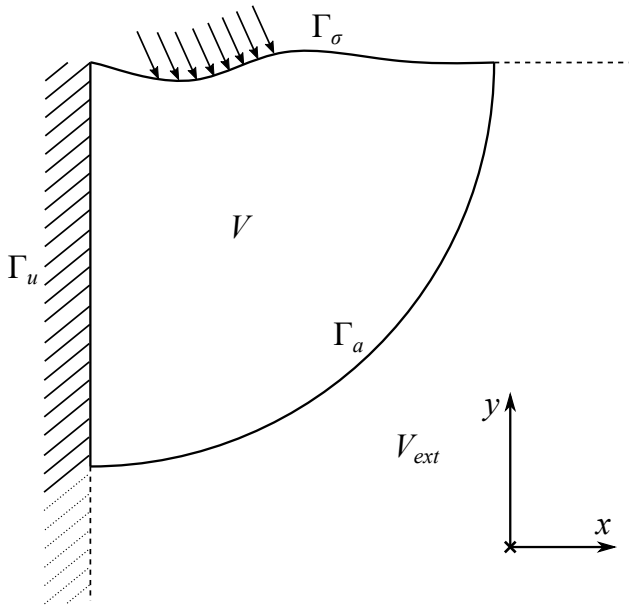

Figure 4.1: Domain modification

In the process of discretization, the internal domain V is divided into finite elements similarly as was done for bounded domains. The boundary Γ^e of the element located in the vicinity of the absorbing boundary will additionally contain part Γ_a^e, which stands for a portion of the absorbing boundary Γ_a.

4.2 Absorbing Boundary Condition

It was already indicated in the introduction of the chapter, that there exists a linear relation between the Sommerfeld-compliant displacement field $\boldsymbol{u}^{r,\theta}$ and the corresponding traction vector $\boldsymbol{t}^{r,\theta}$ when the radius r tends to infinity. The superscripts r,θ indicate the components are expressed in radial and angular directions. Generally, such Dirichlet-to-Neumann mapping can be expressed as

$$\boldsymbol{t}^{r,\theta} = \boldsymbol{C}\boldsymbol{u}^{r,\theta} \text{ for } r \to \infty, \tag{4.1}$$

where $\boldsymbol{C}$ denotes matrix of constants.

The previous equation represents the actual absorbing boundary condition, which is subsequently weakly imposed on the absorbing boundary Γ_a^e. Note that eq. (4.1) holds only infinitely far from the origin, when enforced in the finite distances, it results in an approximation and some reflections occur.

In the following sections the Sommerfeld radiation condition is introduced and the exact form of eq. (4.1) is derived.

4.2.1 Sommerfeld Radiation Condition

The Sommerfeld radiation condition states that energy must be radiated from a source towards infinity and no waves are allowed to come from infinity. The condition is expressed for the solutions of the Helmholtz equation. It was described in section 3.2 that the Lamé equation expressed in terms unknown displacement components can be decomposed into two uncoupled Helmholtz equations in terms of potentials Φ_p and Φ_s. The radiation condition then reads [Sommerfeld 1912]

$$\lim_{r\to\infty} \sqrt{r}\left(\frac{\partial \Phi_\alpha}{\partial r} - ik_\alpha \Phi_\alpha\right) = 0, \tag{4.2}$$

where $\alpha = \{p,s\}$. Therefore, the solutions expressed by eqs. (3.23) and (3.24) of the underlying Helmholtz equation are now restricted by eq. (4.2). It was already mentioned that the radiation condition is satisfied only if the Hankel functions are chosen as the radial component W_n of the solution for Φ_α. This statement is now explained in detail.

For a general argument $k_\alpha r$, Hankel functions (as well as all the solutions of the Bessel equation) are defined by a series expansion. However, for large arguments, an asymptotic form of Hankel function is found [Arfken et al 2013a]

$$H_n^{(h)}(k_\alpha r) = \sqrt{\frac{2}{\pi k_\alpha r}} \exp\left((-1)^{h+1} i \left(k_\alpha r - (2n+1)\frac{\pi}{4}\right)\right), \tag{4.3}$$

where $h = \{1,2\}$ denotes the kind of the Hankel function and n stands for its order. The first two derivatives with respect to r are then expressed as

$$\begin{aligned}\frac{\partial H_n^{(h)}}{\partial r} =& \sqrt{\frac{2}{\pi k_\alpha r}} \exp\left((-1)^{h+1} i \left(k_\alpha r - (2n+1)\frac{\pi}{4}\right)\right)\left((-1)^{h+1} k_\alpha i - \frac{1}{2r}\right) = \\ =& H_n^{(h)}\left((-1)^{h+1} k_\alpha i - \frac{1}{2r}\right), \end{aligned} \tag{4.4}$$

$$\frac{\partial^2 H_n^{(h)}}{\partial r^2} = H_n^{(h)}\left(-k_\alpha^2 - (-1)^{h+1}\frac{k_\alpha i}{r} + \frac{3}{4r^2}\right). \tag{4.5}$$

The solutions (3.23) and (3.24) of the Helmholtz equation for a single order n

$$\Phi_{\alpha,n} = W_n(k_\alpha r)\exp(in\theta) \tag{4.6}$$

are now inserted into eq. (4.2). The asymptotic form (4.3) of the Hankel function is considered as the radial component W_n. Since the radiation condition is expressed for $r \to \infty$, this approach is

valid. The limit is then reformulated

$$\begin{aligned}
\lim_{r\to\infty}\sqrt{r}\left(\frac{\partial(W_n\exp(in\theta))}{\partial r}-ik_\alpha W_n\exp(in\theta)\right)&=0\\
\lim_{r\to\infty}\sqrt{r}\left(\frac{\partial H_n^{(h)}}{\partial r}-ik_\alpha H_n^{(h)}\right)&=0\\
\lim_{r\to\infty}\sqrt{r}\left(H_n^{(h)}\left((-1)^{h+1}k_\alpha i-\frac{1}{2r}\right)-ik_\alpha H_n^{(h)}\right)&=0\\
\lim_{r\to\infty}\sqrt{r}H_n^{(h)}\left((-1)^{h+1}k_\alpha i-\frac{1}{2r}-k_\alpha i\right)&=0\\
\lim_{r\to\infty}\sqrt{r}H_n^{(h)}\left((-1)^{h+1}-1\right)k_\alpha i-\lim_{r\to\infty}\frac{1}{2\sqrt{r}}H_n^{(h)}&=0.
\end{aligned}\tag{4.7}$$

Note that the exponential term in the asymptotic expression (4.3) for the Hankel function can be split as

$$H_n^{(h)}=\sqrt{\frac{2}{\pi k_\alpha r}}\exp\left((-1)^{h+1}ik_\alpha r\right)\exp\left(-(-1)^{h+1}i(2n+1)\frac{\pi}{4}\right),\tag{4.8}$$

where the second exponential is a constant. With the use of this property the second limit in eq. (4.7) can be reformulated

$$\begin{aligned}
\lim_{r\to\infty}\frac{1}{2\sqrt{r}}H_n^{(h)}&=\lim_{r\to\infty}\frac{1}{2\sqrt{r}}\sqrt{\frac{2}{\pi k_\alpha r}}\exp\left((-1)^{h+1}ik_\alpha r\right)\exp\left(-(-1)^{h+1}i(2n+1)\frac{\pi}{4}\right)=\\
&=\frac{1}{2}\sqrt{\frac{2}{\pi k_\alpha}}\exp\left(-(-1)^{h+1}i(2n+1)\frac{\pi}{4}\right)\lim_{r\to\infty}\frac{1}{r}\exp\left((-1)^{h+1}ik_\alpha r\right).
\end{aligned}\tag{4.9}$$

In general, the wave number k_α is a complex number and can be expressed as

$$k_\alpha=\mathrm{Re}(k_\alpha)+i\,\mathrm{Im}(k_\alpha).\tag{4.10}$$

The limit appearing in the second row of eq. (4.9) is analysed next

$$\begin{aligned}
\lim_{r\to\infty}\frac{1}{r}\exp\left((-1)^{h+1}ik_\alpha r\right)&=\lim_{r\to\infty}\frac{1}{r}\exp\left((-1)^{h+1}i\left(\mathrm{Re}(k_\alpha)+i\,\mathrm{Im}(k_\alpha)\right)r\right)=\\
&=\lim_{r\to\infty}\frac{1}{r}\exp\left((-1)^{h+1}i\,\mathrm{Re}(k_\alpha)r\right)\exp\left(-(-1)^{h+1}\,\mathrm{Im}(k_\alpha)r\right).
\end{aligned}\tag{4.11}$$

The first exponential term in the previous relation represents a harmonic function, since an imaginary unit appears in the exponent. On the other hand, the second term is exponentially increasing or decaying function, depending on the sign of the imaginary part $\mathrm{Im}(k_\alpha)$ of the wave number and the kind of the Hankel function, which is represented by symbol h. In the case of Hankel function of the first kind ($h=1$), the imaginary part of the wave number needs to be positive ($\mathrm{Im}(k_\alpha)>0$) so that the exponential term is a decaying function and the limit is zero. Contrary, if the Hankel function is of second kind ($h=2$), imaginary part of the wave number needs to be negative ($\mathrm{Im}(k_\alpha)<0$) so that the limit is finite and zero. If the imaginary part of the wave number is zero,

only the harmonic part remains in the expression. However, due to the hyperbolic factor $1/r$ the limit is zero any way. For all these cases, the limit in eq. (4.11) is zero and therefore the limit in eq. (4.9) is also zero.

In the following, the first term in eq. (4.7) is investigated. It can be developed as

$$\begin{aligned}
&\lim_{r\to\infty}\sqrt{r}H_n^{(h)}\left((-1)^{h+1}-1\right)k_\alpha i = \\
&=\sqrt{r}\sqrt{\frac{2}{\pi k_\alpha r}}\exp\left((-1)^{h+1}ik_\alpha r\right)\exp\left(-(-1)^{h+1}i(2n+1)\frac{\pi}{4}\right)\left((-1)^{h+1}-1\right)k_\alpha i = \\
&=\left((-1)^{h+1}-1\right)k_\alpha i\sqrt{\frac{2}{\pi k_\alpha}}\exp\left(-(-1)^{h+1}i(2n+1)\frac{\pi}{4}\right)\lim_{r\to\infty}\exp\left((-1)^{h+1}ik_\alpha r\right).
\end{aligned} \tag{4.12}$$

The previous expression is always equal to zero if Hankel function of the first kind is adopted, since the relation

$$(-1)^{h+1}-1=0 \text{ for } h=1 \tag{4.13}$$

holds. For the Hankel function of the second kind, it is necessary that the imaginary part of the wave number is negative ($\mathrm{Im}(k_\alpha)<0$) so that the limit in the previous equation is zero. This could be derived in the same way as was described in the previous paragraph. However, if the wave number is real ($\mathrm{Im}(k_\alpha)=0$), the limit in the last row of eq. (4.12) does not exist and the whole expression is zero only for the Hankel functions of the first kind due to eq. (4.13).

For convenience the previous derivations are now summarized. It was shown that the asymptotic form of the Hankel function for large arguments satisfies the Sommerfeld radiation condition, however, under constraint placed on the chosen Hankel function kind. This restriction is ensured for the following cases: If the imaginary part of the wave number is positive, Hankel function of the first kind must be chosen. On the other hand, if the imaginary part of the wave number is negative, Hankel function of the second kind must be adopted. If the wave number is real, only Hankel function of the first kind satisfies the radiation condition.

4.2.2 Far-field Propagation

In the previous section, it was shown that under some restrictions, the asymptotic form of Hankel functions for large arguments fulfil the Sommerfeld radiation condition. This motivates to also use the asymptotic expression for the derivation of the exact form of the displacement, strain, stress and traction fields in the large distances from the origin.

To start with, the displacement field approximation was defined in eq. (3.1), considering only the homogeneous part, it may be expanded as

$$\boldsymbol{u}=\boldsymbol{U}\boldsymbol{X}=\sum_{n=-N}^{N}\boldsymbol{U_n}\boldsymbol{X_n}=\sum_{n=-N}^{N}\boldsymbol{u_n}. \tag{4.14}$$

In the previous equation the layout of the basis $\boldsymbol{U}$ and vector $\boldsymbol{X}$ introduced in eqs. (3.29) and (3.35) was inserted, which allows to represent the matrix-vector product as a sum of sub products

$\boldsymbol{u_n} = \boldsymbol{U_n X_n}$. If the basis $\boldsymbol{U}$ contains functions for all orders n, meaning $N = \infty$, eq. (4.14) represents the exact solution for arbitrary boundary conditions. Vector $\boldsymbol{u_n}$ denotes a part of the complete homogeneous solution related to a single order n. Components of the vector $\boldsymbol{u_n}$ are displacements in Cartesian directions, however, for further derivations it is more convenient to work with vector $\boldsymbol{u_n^{r,\theta}}$, whose components are displacements in radial and angular directions. The relation between both vectors reads

$$\boldsymbol{u_n^{r,\theta}} = \boldsymbol{T}^T \boldsymbol{u_n} = \boldsymbol{T}^T \boldsymbol{U_n X_n} = \boldsymbol{U_n^{r,\theta} X_n}, \tag{4.15}$$

where $\boldsymbol{T}$ is the transformation matrix and $\boldsymbol{U_n^{r,\theta}}$ is the matrix collecting basis functions approximating displacements in radial and angular direction, which were defined in eqs. (3.30) and (3.31) respectively. The definition of the matrix $\boldsymbol{U_n^{r,\theta}}$ is developed next considering the asymptotic expression of the Hankel function as the radial component W_n

$$\begin{aligned}
\boldsymbol{U_n^{r,\theta}} &= \begin{bmatrix} \dfrac{\partial W_n(k_p r)}{\partial r} & \dfrac{in}{r} W_n(k_s r) \\ \dfrac{in}{r} W_n(k_p r) & -\dfrac{\partial W_n(k_s r)}{\partial r} \end{bmatrix} \exp(in\theta) = \begin{bmatrix} \dfrac{\partial H_n^{(h)}(k_p r)}{\partial r} & \dfrac{in}{r} H_n^{(h)}(k_s r) \\ \dfrac{in}{r} H_n^{(h)}(k_p r) & -\dfrac{\partial H_n^{(h)}(k_s r)}{\partial r} \end{bmatrix} \exp(in\theta) = \\
&= \begin{bmatrix} H_n^{(h)}(k_p r)\left((-1)^{h+1} k_p i - \dfrac{1}{2r}\right) & \dfrac{in}{r} H_n^{(h)}(k_s r) \\ \dfrac{in}{r} H_n^{(h)}(k_p r) & -H_n^{(h)}(k_s r)\left((-1)^{h+1} k_s i - \dfrac{1}{2r}\right) \end{bmatrix} \exp(in\theta) = \\
&= \begin{bmatrix} \left((-1)^{h+1} k_p i - \dfrac{1}{2r}\right) & \dfrac{in}{r} \\ \dfrac{in}{r} & -\left((-1)^{h+1} k_s i - \dfrac{1}{2r}\right) \end{bmatrix} \begin{bmatrix} H_n^{(h)}(k_p r) & 0 \\ 0 & H_n^{(h)}(k_s r) \end{bmatrix} \exp(in\theta).
\end{aligned} \tag{4.16}$$

For large radius r, the terms including $1/r$ can be neglected since their contribution is much smaller compared to the other parts. With this assumption, the previous equation yields

$$\boldsymbol{U_n^{r,\theta}} = i(-1)^{h+1} \begin{bmatrix} k_p & 0 \\ 0 & -k_s \end{bmatrix} \begin{bmatrix} H_n^{(h)}(k_p r) & 0 \\ 0 & H_n^{(h)}(k_s r) \end{bmatrix} \exp(in\theta) = \boldsymbol{U_* H_n} \exp(in\theta), \tag{4.17}$$

where

$$\boldsymbol{U_*} = i(-1)^{h+1} \begin{bmatrix} k_p & 0 \\ 0 & -k_s \end{bmatrix}, \tag{4.18}$$

$$\boldsymbol{H_n} = \begin{bmatrix} H_n^{(h)}(k_p r) & 0 \\ 0 & H_n^{(h)}(k_s r) \end{bmatrix}. \tag{4.19}$$

In figures 4.2 and 4.3 the components of the displacement basis $\boldsymbol{U_n^{r,\theta}}$ are plotted considering the original definition of the basis as in eq. (3.31) or in the first line of eq. (4.16). The Hankel function of the first kind and order $n = 1$ was adopted for the function W_n. Note that the original form of the Hankel function is used in the mentioned plots, not the asymptotic simplification. The basis functions are evaluated on a circular domain centred at origin. However, a portion of the

region in the vicinity of the center is excluded, since the derived displacement shapes are singular when $r \to 0$. The particular values of the wave numbers were chosen as $k_p = 0.475$ 1/m and $k_s = 0.889$ 1/m.

In fig. 4.2 the real parts of the displacements in radial and angular direction are visualized considering the p-wave part of the solution. It can be seen that for large radii, the displacement component in angular direction tends to zero much faster compared to the radial one. In fig. 4.3 the s-wave part of the displacement solution is plotted. On the other hand, in latter figure the radial component of the displacement field tends to zero for large radii. Both of the previous findings correspond to the diagonal form of the simplified basis $\boldsymbol{U}_{\boldsymbol{n}}^{\boldsymbol{r},\boldsymbol{\theta}}$ defined in eq. (4.17), where the part associated to p-waves has only displacement contribution in radial direction and the s-wave part generates displacement in angular direction only.

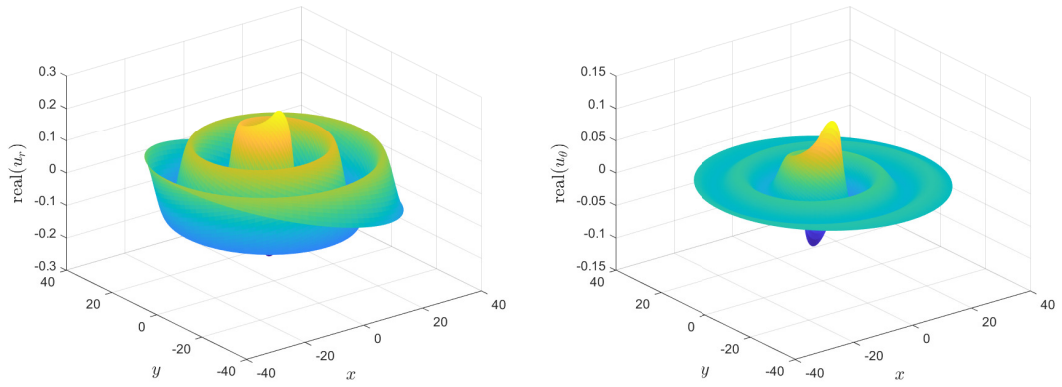

Figure 4.2: P-wave part of the displacement basis $\boldsymbol{U}_{\mathbf{1}}^{r,\theta}$

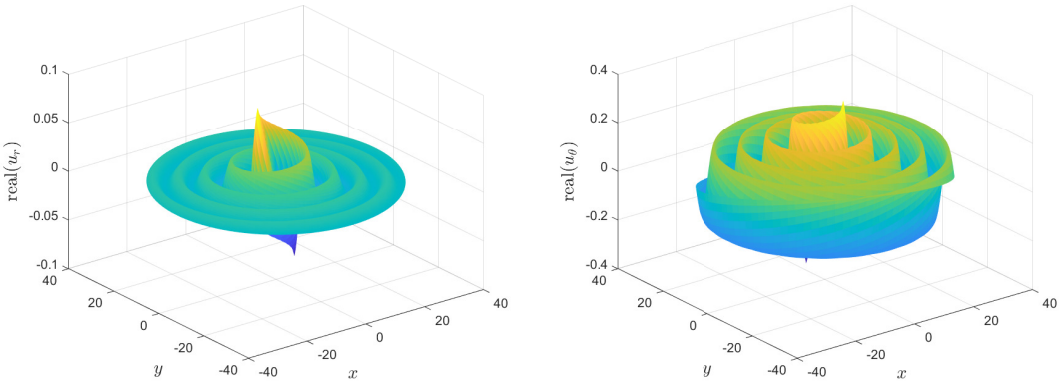

Figure 4.3: S-wave part of the displacement basis $\boldsymbol{U}_{\mathbf{1}}^{r,\theta}$

Similar ideas can now be applied also for the derivation of the strain far field. The strain solution expressed in the polar reference frame for a single order n is given as

$$\boldsymbol{\varepsilon}_{\boldsymbol{n}}^{\boldsymbol{r},\boldsymbol{\theta}} = \boldsymbol{E}_{\boldsymbol{n}}^{\boldsymbol{r},\boldsymbol{\theta}} \boldsymbol{X}_{\boldsymbol{n}}, \tag{4.20}$$

where matrix $\boldsymbol{E}_{\boldsymbol{n}}^{\boldsymbol{r},\boldsymbol{\theta}}$, collecting the strain basis functions for a single order n, is defined in eq. (3.34). Inserting the asymptotic form of the Hankel function for the radial component W_n, eq. (3.34) is modified

$$
\begin{aligned}
\boldsymbol{E}_{\boldsymbol{n}}^{\boldsymbol{r},\boldsymbol{\theta}} &= \begin{bmatrix} \dfrac{\partial^2\Phi_p}{\partial r^2} & \dfrac{1}{r}\dfrac{\partial^2\Phi_s}{\partial\theta\partial r} \\ \dfrac{1}{r^2}\dfrac{\partial^2\Phi_p}{\partial\theta^2} & -\dfrac{1}{r}\dfrac{\partial^2\Phi_s}{\partial r\partial\theta} \\ 2\dfrac{1}{r}\dfrac{\partial^2\Phi_p}{\partial r\partial\theta} & \dfrac{1}{r^2}\dfrac{\partial^2\Phi_s}{\partial\theta^2} - \dfrac{\partial^2\Phi_s}{\partial r^2} \end{bmatrix} = \\
&= \begin{bmatrix} \dfrac{\partial^2 H_n^{(h)}(k_p r)}{\partial r^2} & \dfrac{in}{r}\dfrac{\partial H_n^{(h)}(k_s r)}{\partial r} \\ -\dfrac{n^2}{r^2}H_n^{(h)}(k_p r) & -\dfrac{in}{r}\dfrac{\partial H_n^{(h)}(k_s r)}{\partial r} \\ 2\dfrac{in}{r}\dfrac{\partial H_n^{(h)}(k_p r)}{\partial r} & -\dfrac{n^2}{r^2}H_n^{(h)}(k_s r) - \dfrac{\partial^2 H_n^{(h)}(k_s r)}{\partial r^2} \end{bmatrix} \exp(in\theta) = \\
&= \begin{bmatrix} H_n^{(h)}(k_p r)\left(-k_p^2 - (-1)^{h+1}\dfrac{k_p i}{r} + \dfrac{3}{4r^2}\right) & \dfrac{in}{r}H_n^{(h)}(k_s r)\left((-1)^{h+1}k_s i - \dfrac{1}{2r}\right) \\ -\dfrac{n^2}{r^2}H_n^{(h)}(k_p r) & -\dfrac{in}{r}H_n^{(h)}(k_s r)\left((-1)^{h+1}k_s i - \dfrac{1}{2r}\right) \\ 2\dfrac{in}{r}H_n^{(h)}(k_p r)\left((-1)^{h+1}k_p i - \dfrac{1}{2r}\right) & -H_n^{(h)}(k_s r)\left(\dfrac{n^2}{r^2} - k_s^2 - (-1)^{h+1}\dfrac{k_s i}{r} + \dfrac{3}{4r^2}\right) \end{bmatrix} \exp(in\theta) = \\
&= \begin{bmatrix} -k_p^2 - (-1)^{h+1}\dfrac{k_p i}{r} + \dfrac{3}{4r^2} & \dfrac{in}{r}\left((-1)^{h+1}k_s i - \dfrac{1}{2r}\right) \\ -\dfrac{n^2}{r^2} & -\dfrac{in}{r}\left((-1)^{h+1}k_s i - \dfrac{1}{2r}\right) \\ 2\dfrac{in}{r}\left((-1)^{h+1}k_p i - \dfrac{1}{2r}\right) & -\dfrac{n^2}{r^2} + k_s^2 + (-1)^{h+1}\dfrac{k_s i}{r} - \dfrac{3}{4r^2} \end{bmatrix} \begin{bmatrix} H_n^{(h)}(k_p r) & 0 \\ 0 & H_n^{(h)}(k_s r) \end{bmatrix} \exp(in\theta).
\end{aligned}
\tag{4.21}
$$

The terms including $1/r$ and $1/r^2$ are again neglected since for large r their influence is minor. The previous equation then results in

$$
\boldsymbol{E}_{\boldsymbol{n}}^{\boldsymbol{r},\boldsymbol{\theta}} = \begin{bmatrix} -k_p^2 & 0 \\ 0 & 0 \\ 0 & k_s^2 \end{bmatrix} \begin{bmatrix} H_n^{(h)}(k_p r) & 0 \\ 0 & H_n^{(h)}(k_s r) \end{bmatrix} \exp(in\theta) = \boldsymbol{E}_* \boldsymbol{H}_{\boldsymbol{n}} \exp(in\theta), \tag{4.22}
$$

where

$$
\boldsymbol{E}_* = \begin{bmatrix} -k_p^2 & 0 \\ 0 & 0 \\ 0 & k_s^2 \end{bmatrix}. \tag{4.23}
$$

By the application of the material equations, the stress far-field solution $\boldsymbol{\sigma}_{\boldsymbol{n}}^{\boldsymbol{r},\boldsymbol{\theta}}$ with components in radial and angular directions can be easily obtained from the already derived strain solution

$$
\boldsymbol{\sigma}_{\boldsymbol{n}}^{\boldsymbol{r},\boldsymbol{\theta}} = \boldsymbol{k}\boldsymbol{\varepsilon}_{\boldsymbol{n}}^{\boldsymbol{r},\boldsymbol{\theta}} = \boldsymbol{k}\boldsymbol{E}_{\boldsymbol{n}}^{\boldsymbol{r},\boldsymbol{\theta}}\boldsymbol{X}_{\boldsymbol{n}} = \boldsymbol{S}_{\boldsymbol{n}}^{\boldsymbol{r},\boldsymbol{\theta}}\boldsymbol{X}_{\boldsymbol{n}}. \tag{4.24}
$$

Matrix $\boldsymbol{S}_{\boldsymbol{n}}^{\boldsymbol{r},\boldsymbol{\theta}}$ contains the stress basis for a single order n and its exact form is derived as

$$\begin{aligned}\boldsymbol{S}_{\boldsymbol{n}}^{\boldsymbol{r},\boldsymbol{\theta}} =& \boldsymbol{k}\boldsymbol{E}_{\boldsymbol{n}}^{\boldsymbol{r},\boldsymbol{\theta}} = \begin{bmatrix}\lambda+2\mu & \lambda & 0\\ \lambda & \lambda+2\mu & 0\\ 0 & 0 & \mu\end{bmatrix}\begin{bmatrix}-k_p^2 & 0\\ 0 & 0\\ 0 & k_s^2\end{bmatrix}\begin{bmatrix}H_n^{(h)}(k_p r) & 0\\ 0 & H_n^{(h)}(k_s r)\end{bmatrix}\exp(in\theta) = \\ =& \begin{bmatrix}-k_p^2(\lambda+2\mu) & 0\\ -k_p^2\lambda & 0\\ 0 & k_s^2\mu\end{bmatrix}\begin{bmatrix}H_n^{(h)}(k_p r) & 0\\ 0 & H_n^{(h)}(k_s r)\end{bmatrix}\exp(in\theta) = \boldsymbol{S}_*\boldsymbol{H}_{\boldsymbol{n}}\exp(in\theta),\end{aligned} \tag{4.25}$$

where

$$\boldsymbol{S}_* = \begin{bmatrix}-k_p^2(\lambda+2\mu) & 0\\ -k_p^2\lambda & 0\\ 0 & k_s^2\mu\end{bmatrix}. \tag{4.26}$$

The last field to be investigated are the tractions evaluated at a circular boundary located sufficiently far from the origin so that the asymptotic expression of the Hankel functions can be applied. Boundary tractions can be computed based on the boundary equilibrium expressed by eq. (2.35). The exact form of matrix $\boldsymbol{N}$ was introduced in eq. (2.14), however, since all the derivations in this section are perform in the polar reference frame, the components of the matrix $\boldsymbol{N}$ also need to be expressed in such coordinate system. Therefore, matrix

$$\boldsymbol{N}^{\boldsymbol{r},\boldsymbol{\theta}} = \begin{bmatrix}n_r & 0 & n_\theta\\ 0 & n_\theta & n_r\end{bmatrix} \tag{4.27}$$

is used instead, n_r and n_θ are the polar components of the outward unit normal at the boundary.

The desired boundary traction field is then computed as

$$\boldsymbol{t}_{\boldsymbol{n}}^{\boldsymbol{r},\boldsymbol{\theta}} = \boldsymbol{N}^{\boldsymbol{r},\boldsymbol{\theta}}\boldsymbol{\sigma}_{\boldsymbol{n}}^{\boldsymbol{r},\boldsymbol{\theta}} = \boldsymbol{N}^{\boldsymbol{r},\boldsymbol{\theta}}\boldsymbol{S}_{\boldsymbol{n}}^{\boldsymbol{r},\boldsymbol{\theta}}\boldsymbol{X}_{\boldsymbol{n}} = \boldsymbol{T}_{\boldsymbol{n}}^{\boldsymbol{r},\boldsymbol{\theta}}\boldsymbol{X}_{\boldsymbol{n}}, \tag{4.28}$$

where $\boldsymbol{T}_{\boldsymbol{n}}^{\boldsymbol{r},\boldsymbol{\theta}}$ stands for the matrix collecting boundary traction functions derived from the solution $\boldsymbol{u}_{\boldsymbol{n}}^{\boldsymbol{r},\boldsymbol{\theta}}$ for a single order n

$$\begin{aligned}\boldsymbol{T}_{\boldsymbol{n}}^{\boldsymbol{r},\boldsymbol{\theta}} =& \boldsymbol{N}^{\boldsymbol{r},\boldsymbol{\theta}}\boldsymbol{S}_{\boldsymbol{n}}^{\boldsymbol{r},\boldsymbol{\theta}} = \boldsymbol{N}^{\boldsymbol{r},\boldsymbol{\theta}}\boldsymbol{S}_*\boldsymbol{H}_{\boldsymbol{n}}\exp(in\theta) = \begin{bmatrix}n_r & 0 & n_\theta\\ 0 & n_\theta & n_r\end{bmatrix}\begin{bmatrix}-k_p^2(\lambda+2\mu) & 0\\ -k_p^2\lambda & 0\\ 0 & k_s^2\mu\end{bmatrix}\boldsymbol{H}_{\boldsymbol{n}}\exp(in\theta) = \\ =& \begin{bmatrix}-n_r k_p^2(\lambda+2\mu) & n_\theta k_s^2\mu\\ -n_\theta k_p^2\lambda & n_r k_s^2\mu\end{bmatrix}\boldsymbol{H}_{\boldsymbol{n}}\exp(in\theta) = \boldsymbol{T}_*\boldsymbol{H}_{\boldsymbol{n}}\exp(in\theta).\end{aligned} \tag{4.29}$$

As was mentioned, the boundary at which the tractions are evaluated is assumed to be circular. This implies that the the angular component n_θ of the outward normal is zero and the radial component $n_r = 1$, since the normal vector has a unit length. Using these findings, the relation for

$\boldsymbol{T}_*$ can be simplified

$$\boldsymbol{T}_* = \begin{bmatrix} -n_r k_p^2(\lambda+2\mu) & n_\theta k_s^2 \mu \\ -n_\theta k_p^2 \lambda & n_r k_s^2 \mu \end{bmatrix} = \begin{bmatrix} -k_p^2(\lambda+2\mu) & 0 \\ 0 & k_s^2 \mu \end{bmatrix}. \tag{4.30}$$

To conclude, main points of this section are summarized. The general form of the basis functions, which solve the governing differential equation in terms of displacements, was discussed in section 3.2. Each of these displacement solutions has the associated strain, stress and boundary traction fields, which can be derived based on the relations stated in chapter 2. In this part of the thesis, the aim was to find the exact relations for the associated fields evaluated in large distances from the origin. The matrices $\boldsymbol{U}_{\boldsymbol{n}}^{\boldsymbol{r,\theta}}$, $\boldsymbol{E}_{\boldsymbol{n}}^{\boldsymbol{r,\theta}}$, $\boldsymbol{S}_{\boldsymbol{n}}^{\boldsymbol{r,\theta}}$ and $\boldsymbol{T}_{\boldsymbol{n}}^{\boldsymbol{r,\theta}}$ collecting the individual basis functions for a single order n were derived. The rows of the matrices are associated with the individual components of the field, for which the polar reference frame was considered. The columns of the matrices represent the contribution of the pressure and shear waves respectively.

4.2.3 Dirichlet-to-Neumann Mapping

The solutions of the homogeneous Lamé equation for the individual fields in a sufficiently large distance from origin are now used to form the Dirichlet-to-Neumann map (4.1). Matrix $\boldsymbol{T}_*$ appearing in the expression for the traction basis in eq. (4.29) can be reformulated as

$$\boldsymbol{T}_* = \begin{bmatrix} -k_p^2(\lambda+2\mu) & 0 \\ 0 & k_s^2\mu \end{bmatrix} = i(-1)^{h+1} \begin{bmatrix} k_p(\lambda+2\mu) & 0 \\ 0 & k_s\mu \end{bmatrix} i(-1)^{h+1} \begin{bmatrix} k_p & 0 \\ 0 & -k_s \end{bmatrix} = \boldsymbol{C}\boldsymbol{U}_*, \tag{4.31}$$

where

$$\boldsymbol{C} = i(-1)^{h+1} \begin{bmatrix} k_p(\lambda+2\mu) & 0 \\ 0 & k_s\mu \end{bmatrix} \tag{4.32}$$

is the matrix of constants connecting matrices $\boldsymbol{U}_*$ and $\boldsymbol{T}_*$. Eq. (4.31) implies that the traction and displacement bases evaluated at a circular boundary in large distance from origin are related through a matrix of constants, which can be shown as

$$\boldsymbol{T}_{\boldsymbol{n}}^{\boldsymbol{r,\theta}} = \boldsymbol{T}_*\boldsymbol{H}_{\boldsymbol{n}} \exp(in\theta) = \boldsymbol{C}\boldsymbol{U}_*\boldsymbol{H}_{\boldsymbol{n}} \exp(in\theta) = \boldsymbol{C}\boldsymbol{U}_{\boldsymbol{n}}^{r,\theta}. \tag{4.33}$$

Furthermore, the complete solution can be recovered by including matrices collecting basis functions for all orders $-\infty < n < \infty$ multiplied by unknown coefficients collected in vector $\boldsymbol{X}$. Therefore, the complete traction solution evaluated on a circular boundary sufficiently far from the origin is expressed as

$$\begin{aligned} \boldsymbol{t}^{\boldsymbol{r,\theta}} &= \sum_{n=-\infty}^{\infty} \boldsymbol{t}_{\boldsymbol{n}}^{\boldsymbol{r,\theta}} = \sum_{n=-\infty}^{\infty} \boldsymbol{T}_{\boldsymbol{n}}^{\boldsymbol{r,\theta}} \boldsymbol{X}_{\boldsymbol{n}} = \sum_{n=-\infty}^{\infty} \boldsymbol{C}\boldsymbol{U}_{\boldsymbol{n}}^{r,\theta} \boldsymbol{X}_{\boldsymbol{n}} = \boldsymbol{C} \sum_{n=-\infty}^{\infty} \boldsymbol{U}_{\boldsymbol{n}}^{r,\theta} \boldsymbol{X}_{\boldsymbol{n}} = \boldsymbol{C}\boldsymbol{u}^{\boldsymbol{r,\theta}} \\ \boldsymbol{t}^{\boldsymbol{r,\theta}} &= \boldsymbol{C}\boldsymbol{u}^{\boldsymbol{r,\theta}} \end{aligned} \tag{4.34}$$

This equation shows that on a circular boundary in large distance from the source of excitation and irregularities, the boundary tractions and the displacements are connected through a matrix of constants. This statement holds for arbitrary loading and boundary conditions.

4.2.4 System Modification

The essence of the absorbing boundary technique is that the Robin-type relation, expressed by eq. (4.34), is weakly imposed on the boundary Γ_a^e located at finite distance from the source of excitation. As the asymptotic form of the Hankel function was used for the derivation of the relation (4.34), it is only valid when the boundary is infinitely far from origin. Therefore, this imposition results in an approximation and some spurious reflections may occur in the vicinity of the boundary. Moreover, the assumption of a circular boundary was considered in the previous section. Consequently, enforcing eq. (4.34) on a non circular boundary may result in an additional source of error.

The finite element system modification is now described. Firstly, the changes are presented for the case of a single element with one continuous Dirichlet boundary and only one absorbing boundary. Afterwards, a generalization for multiple elements is discussed.

Similarly to the Dirichlet boundary, also on the absorbing boundary Γ_a^e the boundary traction field is approximated

$$\boldsymbol{t} = \boldsymbol{Z_a p_a} \text{ on } \Gamma_a^e. \tag{4.35}$$

Matrix $\boldsymbol{Z_a}$ collects the approximation basis functions and vector $\boldsymbol{p_a}$ contains the related unknown coefficients. In this work, the same basis was chosen to approximate the boundary tractions on the Dirichlet as well as on the absorbing boundary, which implies that $\boldsymbol{Z_a} = \boldsymbol{Z}$.

As was already mentioned, eq. (4.34) is weakly enforced while the boundary traction basis $\boldsymbol{Z_a}$ is used as the weighting matrix. For convenience, eq. (4.34) is firstly inverted so that the displacements are expressed in terms of boundary tractions

$$\boldsymbol{u}^{r,\theta} = \boldsymbol{C}^{-1}\boldsymbol{t}^{r,\theta}. \tag{4.36}$$

Moreover, the components of the displacement and traction vectors appearing in the previous relation are in radial and angular directions. However, the boundary traction approximation as well as the displacement approximation is expressed for components in Cartesian directions, as can be noted from eqs. (3.1) and (4.35). Consequently, the relation (4.36) needs to be transformed. Using the transformation matrix $\boldsymbol{T}$, defined in eq. (3.30), and the formulas

$$\boldsymbol{u}^{r,\theta} = \boldsymbol{T}^T\boldsymbol{u}, \tag{4.37}$$

$$\boldsymbol{t}^{r,\theta} = \boldsymbol{T}^T\boldsymbol{t}, \tag{4.38}$$

eq. (4.36) is reformulated

$$\begin{aligned} \boldsymbol{u}^{\boldsymbol{r},\boldsymbol{\theta}} &= \boldsymbol{C}^{-1}\boldsymbol{t}^{\boldsymbol{r},\boldsymbol{\theta}} \\ \boldsymbol{T}^T\boldsymbol{u} &= \boldsymbol{C}^{-1}\boldsymbol{T}^T\boldsymbol{t} \\ \boldsymbol{T}\boldsymbol{T}^T\boldsymbol{u} &= \boldsymbol{T}\boldsymbol{C}^{-1}\boldsymbol{T}^T\boldsymbol{t} \\ \boldsymbol{u} &= \boldsymbol{C}^{\boldsymbol{x},\boldsymbol{y}-1}\boldsymbol{t}, \end{aligned} \tag{4.39}$$

where

$$\boldsymbol{C}^{\boldsymbol{x},\boldsymbol{y}} = \boldsymbol{T}\boldsymbol{C}\boldsymbol{T}^T. \tag{4.40}$$

Note that eqs. (4.39) and (4.34) represent the same relation, just using a different formulation.

Finally, eq. (4.39) can be weakly imposed on Γ_a^e

$$\int \boldsymbol{Z}_{\boldsymbol{a}}^T \left(\boldsymbol{u} - \boldsymbol{C}^{\boldsymbol{x},\boldsymbol{y}-1}\boldsymbol{t}\right) \mathrm{d}\Gamma_a^e = \boldsymbol{0}. \tag{4.41}$$

Inserting the domain displacement and boundary traction approximations, the previous equation is rephrased

$$-\int \boldsymbol{Z}_{\boldsymbol{a}}^T\boldsymbol{U}\,\mathrm{d}\Gamma_a^e\,\boldsymbol{X} + \int \boldsymbol{Z}_{\boldsymbol{a}}^T\boldsymbol{C}^{\boldsymbol{x},\boldsymbol{y}-1}\boldsymbol{Z}_{\boldsymbol{a}}\,\mathrm{d}\Gamma_a^e\,\boldsymbol{p}_{\boldsymbol{a}} = \int \boldsymbol{Z}_{\boldsymbol{a}}^T\boldsymbol{u}_{\boldsymbol{0}}\,\mathrm{d}\Gamma_a^e. \tag{4.42}$$

Using definitions

$$\boldsymbol{B}_{\boldsymbol{a}} = \int \widehat{\boldsymbol{U}}^T\boldsymbol{Z}_{\boldsymbol{a}}\,\mathrm{d}\Gamma_a^e, \tag{4.43}$$

$$\boldsymbol{D}_{\boldsymbol{a}} = \int \boldsymbol{Z}_{\boldsymbol{a}}^T\boldsymbol{C}^{\boldsymbol{x},\boldsymbol{y}-1}\boldsymbol{Z}_{\boldsymbol{a}}\,\mathrm{d}\Gamma_a^e, \tag{4.44}$$

$$\overline{\boldsymbol{u}_{\boldsymbol{a}_0}} = \int \boldsymbol{Z}_{\boldsymbol{a}}^T\boldsymbol{u}_{\boldsymbol{0}}\,\mathrm{d}\Gamma_a^e, \tag{4.45}$$

eq. (4.42) is abbreviated as

$$-\widehat{\boldsymbol{B}_{\boldsymbol{a}}}^T\,\boldsymbol{X} + \boldsymbol{D}_{\boldsymbol{a}}\,\boldsymbol{p}_{\boldsymbol{a}} = \overline{\boldsymbol{u}_{\boldsymbol{a}_0}}. \tag{4.46}$$

Another modification of the system arises in eq. (3.47), since the integral over the complete boundary now contains a portion related to the absorbing boundary Γ_a^e. Hence, the equation is modified

$$\int \widehat{\boldsymbol{U}}^T\boldsymbol{\mathcal{D}}\boldsymbol{\sigma}\,\mathrm{d}V^e = \int \widehat{\boldsymbol{U}}^T\boldsymbol{t}_{\boldsymbol{\Gamma}}\,\mathrm{d}\Gamma_\sigma^e + \int \widehat{\boldsymbol{U}}^T\boldsymbol{Z}\,\mathrm{d}\Gamma_u^e\,\boldsymbol{p} + \int \widehat{\boldsymbol{U}}^T\boldsymbol{Z}_{\boldsymbol{a}}\,\mathrm{d}\Gamma_a^e\,\boldsymbol{p}_{\boldsymbol{a}} - \int \left(\boldsymbol{\mathcal{D}}^*\widehat{\boldsymbol{U}}\right)^T\boldsymbol{\sigma}\,\mathrm{d}V^e. \tag{4.47}$$

Consequently, the first equation (3.62) of the governing system is changed as

$$\boldsymbol{D}\,\boldsymbol{X} - \boldsymbol{B}\,\boldsymbol{p} - \boldsymbol{B}_{\boldsymbol{a}}\,\boldsymbol{p}_{\boldsymbol{a}} = \overline{\boldsymbol{t}_{\boldsymbol{\Gamma}}} - \overline{\boldsymbol{t}_{\boldsymbol{\Gamma}_{\boldsymbol{0}}}}. \tag{4.48}$$

Considering both modifications, the finite element system expressed in eq. (3.68) is reformulated

$$\begin{bmatrix} \boldsymbol{D} & -\boldsymbol{B_a} & -\boldsymbol{B} \\ -\widehat{\boldsymbol{B_a}}^T & \boldsymbol{D_a} & \boldsymbol{0} \\ -\widehat{\boldsymbol{B}}^T & \boldsymbol{0} & \boldsymbol{0} \end{bmatrix} \begin{bmatrix} \boldsymbol{X} \\ \boldsymbol{p_a} \\ \boldsymbol{p} \end{bmatrix} = \begin{bmatrix} \overline{\boldsymbol{t_\Gamma}} - \overline{\boldsymbol{t_{\Gamma_0}}} \\ \overline{\boldsymbol{u_{a_0}}} \\ \overline{\boldsymbol{u_{\Gamma_0}}} - \overline{\boldsymbol{u_\Gamma}} \end{bmatrix}. \tag{4.49}$$

A generalization for the case of multiple finite elements is straightforward. Since the individual absorbing boundary edges cannot be shared by two elements, the coefficients $\boldsymbol{p_a}$ are related to one element only. The global system defined in eq. (3.100) can be modified analogously as the single element system, which results in

$$\begin{bmatrix} \boldsymbol{D_G} & -\boldsymbol{B_{a,G}} & -\boldsymbol{B_G} \\ -\widehat{\boldsymbol{B_{a,G}}}^T & \boldsymbol{D_{a,G}} & \boldsymbol{0} \\ -\widehat{\boldsymbol{B_G}}^T & \boldsymbol{0} & \boldsymbol{0} \end{bmatrix} \begin{bmatrix} \boldsymbol{X_G} \\ \boldsymbol{p_{a,G}} \\ \boldsymbol{p_G} \end{bmatrix} = \begin{bmatrix} \overline{\boldsymbol{t_{\Gamma_G}}} - \overline{\boldsymbol{t_{\Gamma_{0,G}}}} \\ \overline{\boldsymbol{u_{a_{0,G}}}} \\ \overline{\boldsymbol{u_{\Gamma_G}}} \end{bmatrix}, \tag{4.50}$$

where

$$\boldsymbol{D_{a,G}} = \begin{bmatrix} \boldsymbol{D_{a1}} & \boldsymbol{0} & \dots & \boldsymbol{0} \\ \boldsymbol{0} & \boldsymbol{D_{a2}} & \dots & \boldsymbol{0} \\ \vdots & \vdots & \ddots & \boldsymbol{0} \\ \boldsymbol{0} & \boldsymbol{0} & \boldsymbol{0} & \boldsymbol{D_{an_a}} \end{bmatrix}, \tag{4.51}$$

$$\boldsymbol{p_{a,G}} = \begin{bmatrix} \boldsymbol{p_{a1}}^T & \boldsymbol{p_{a2}}^T & \dots & \boldsymbol{p_{an_a}}^T \end{bmatrix}^T, \tag{4.52}$$

$$\overline{\boldsymbol{u_{a_{0,G}}}} = \begin{bmatrix} \overline{\boldsymbol{u_{a_0 1}}}^T & \overline{\boldsymbol{u_{a_0 2}}}^T & \dots & \overline{\boldsymbol{u_{a_0 n_a}}}^T \end{bmatrix}^T. \tag{4.53}$$

The additional subscript $i_a = 1, 2, \dots, n_a$ indicates indexing related to individual absorbing boundary edges with n_a denoting the number of all absorbing boundary edges. The individual $\boldsymbol{B_{a_{i_a}}^{(j_{el})}}$ matrices evaluated for element j_{el} and at absorbing edge i_a are sorted in the global $\boldsymbol{B_{a,G}}$ matrix in the following way: index j_{el} corresponds to the row and subscript i_a to the column in the final global matrix. As some elements may have no absorbing boundary, the global matrix $\boldsymbol{B_{a,G}}$ may contain rows with zeros only.

As the matrix $\boldsymbol{D_{a,G}}$ is symmetric, also the resulting system preserves this property. Due to the fact that the Robin-type relation is explicitly enforced, arbitrary solutions of the Bessel equation can be adopted for the formulation of the displacement basis $\boldsymbol{U}$. The exact forms of the bases derived using the asymptotic form of the Hankel function were only used to obtain the matrix $\boldsymbol{C}$ connecting the displacements and tractions at infinity.

This chapter describes the modelling procedure of infinite domains by an application of the absorbing boundary condition method. The Sommerfeld radiation condition constitutes the fundamental constraint for the previous derivations. In the beginning, it is shown that if the Hankel functions are used as the radial component W_n for the construction of the basis functions, the solution is also Sommerfeld-compliant. These findings are then applied for the derivation of the exact forms of the

solution basis of the individual fields in large distances from origin. From the resulting expressions, the linear mapping is found between the displacement and the traction fields evaluated at the circular boundary at infinity. Afterwards, this relation is weakly enforced at the absorbing boundary located at finite distance from origin, which results in an approximation of the real behaviour. Simultaneously, the tractions are approximated on the absorbing boundary. The resulting system of equations is modified, additional equation as well as structural degrees of freedom emerge. An advantage of the described concept is the freedom of choice of the Bessel solution functions used for the generation of the displacement approximation basis. On the other hand, the main drawbacks are the artificial wave reflections occurring due to the insufficient distance of the absorbing boundary from the origin of excitation or because of the inclination of the absorbing boundary.

5 Introduction to Wave Based Method

It was mentioned in the introduction that to validate the implemented hybrid-Trefftz method, the obtained results are compared to those acquired with the wave based method (WBM). Even though the wave based method modelling technique is not the main part of this thesis, a short chapter is dedicated to a brief introduction of it. Afterwards, main features of both methods are summarized and compared.

The application of the WBM on the steady-state elastodynamic problem is described in [Deckers et al 2012] and [Van Genechten et al 2010]. Both publications served as the reference for the presented theoretical aspects.

5.1 Basic Principle

Similarly to the hybrid-Trefftz method also WBM belongs to the family of Trefftz methods. This implies that the basis functions selected for the approximation of a certain field within the element domain are chosen to satisfy the governing differential equation. The individual basis components implicitly fulfil the governing equation, however, for a general case they violate the prescribed boundary conditions. Therefore, a finite number of such functions is combined so that the error between the true and approximated boundary conditions is decreased. What distinguishes both mentioned methods is the way how the boundary conditions as well as the inter-element continuity conditions are enforced. In the case of WBM, no additional field needs to be approximated, however, the boundary and the inter-element continuity conditions are weakly imposed on the element boundary with the use of the Galerkin weighted residual method. The necessary condition ensuring convergence of the method to the analytical solution is convexity of the element domain.

The set of equations (2.31) to (2.37) describing the elastodynamic problem in the frequency domain derived in chapter 2 form the starting point for the upcoming derivations. For clarity the subscript k related to the time discretization is omitted.

The workflow of the method procedure can be divided in the following parts. Firstly, the domain of the structure is discretized into a number of convex finite elements. Inside each element domain the displacement field is expanded in terms of shape functions multiplied by unknown participation factors. As was already stressed, the basis functions are selected as solutions of the underlying differential equation. Afterwards, the prescribed boundary conditions as well as the continuity between adjacent elements are weakly imposed. Subsequently, the system of algebraic equations is formed with the participation factors being the unknowns. After the solution is obtained, the unknown fields need to be recovered during a post-processing phase. The individual steps are described in detail in the following sections.

5.2 Domain Discretization

It was already indicated that to ensure the convergence to the analytical solution, the analysed domain must be of convex shape. In case this property is not fulfilled, the domain V needs to be partitioned into n_{el} convex subdomains $V^{(i_{el})}$, where $i_{el} = 1,2,\ldots,n_{el}$. The element boundary $\Gamma^{(i_{el})}$ can subsequently be divided into non-overlapping parts $\Gamma_u^{(i_{el})}$, $\Gamma_\sigma^{(i_{el})}$ and $\Gamma_I^{(i_{el},j_{el})}$. The first two symbols stand for the Dirichlet and Neumann boundaries where the displacement components and the boundary tractions are prescribed. $\Gamma_I^{(i_{el},j_{el})}$ denotes the inter-element boundary between two adjacent elements i_{el} and j_{el}.

The displacement and traction boundary conditions can be formulated in normal and tangential directions to the boundary. In residual form they are expressed as

$$\begin{aligned} R_{u_n}^{(i_{el})} &= u_n^{(i_{el})} - u_{\Gamma,n} = 0, \\ R_{u_t}^{(i_{el})} &= u_t^{(i_{el})} - u_{\Gamma,t} = 0, \end{aligned} \quad \text{on } \Gamma_u^{(i_{el})}$$
$$\begin{aligned} R_{t_n}^{(i_{el})} &= t_n^{(i_{el})} - t_{\Gamma,n} = 0, \\ R_{t_t}^{(i_{el})} &= t_t^{(i_{el})} - t_{\Gamma,t} = 0, \end{aligned} \quad \text{on } \Gamma_\sigma^{(i_{el})} \tag{5.1}$$

where $u_{\Gamma,n}$, $u_{\Gamma,t}$, $t_{\Gamma,n}$ and $t_{\Gamma,t}$ are the prescribed displacement and traction components.

There are four continuity conditions which need to be weakly imposed between the neighbouring elements i_{el} and j_{el}. Two are expressed in terms of displacement components $u_n^{(i_{el})}$ and $u_t^{(i_{el})}$ and two in terms of traction components $t_n^{(i_{el})}$ and $t_t^{(i_{el})}$. The conditions can be written in residual form as

$$\begin{aligned} R_{u_n}^{(i_{el},j_{el})} &= u_n^{(i_{el})} + u_n^{(j_{el})} = 0, \\ R_{u_t}^{(i_{el},j_{el})} &= u_t^{(i_{el})} + u_t^{(j_{el})} = 0, \\ R_{t_n}^{(i_{el},j_{el})} &= t_n^{(i_{el})} - t_n^{(j_{el})} = 0, \\ R_{t_t}^{(i_{el},j_{el})} &= t_t^{(i_{el})} - t_t^{(j_{el})} = 0. \end{aligned} \quad \text{on } \Gamma_I^{(i_{el},j_{el})} \tag{5.2}$$

To formulate a well posed problem, exactly two boundary conditions need to be enforced on each point of the boundary. Therefore, the inter-element displacement continuity conditions are imposed on one of the two adjacent elements while the traction continuity condition is enforced on the second element.

5.3 Displacement Field Expansion

As was indicated earlier, the basis functions are restricted to satisfy the homogeneous part of the governing differential equation (2.31). The solution procedure was already described in detail in section 3.2.1. It was shown that by the application of the Helmholtz decomposition (3.6), the system can be decoupled into two independent Helmholtz equations (3.12) and (3.16) in terms of dilatational and shear potentials Φ_p and Φ_s. Afterwards, the solution of the individual Helmholtz equations was obtained in polar reference. An alternative procedure is adopted in this section,

which consists of solving the Helmholtz equations directly in the Cartesian reference frame.

For clarity, a general form of the Helmholtz equation is reproduced

$$\frac{\partial^2 \Phi_\alpha}{\partial x^2} + \frac{\partial^2 \Phi_\alpha}{\partial y^2} + k_\alpha^2 \Phi_\alpha = 0, \tag{5.3}$$

where $\alpha = \{p,s\}$ and k_α denotes the related pressure or shear wave number. The following wave function sets can be considered as solutions of the previous equation

$$\begin{aligned}
\Psi_\alpha^a(x,y) &= \sin\left(k_{x,\alpha}^a x\right) \exp\left(i k_{y,\alpha}^a y\right), \\
\Psi_\alpha^b(x,y) &= \cos\left(k_{x,\alpha}^b x\right) \exp\left(i k_{y,\alpha}^b y\right), \\
\Psi_\alpha^c(x,y) &= \exp\left(i k_{x,\alpha}^c x\right) \sin\left(k_{y,\alpha}^c y\right), \\
\Psi_\alpha^d(x,y) &= \exp\left(i k_{x,\alpha}^d x\right) \cos\left(k_{y,\alpha}^d y\right).
\end{aligned} \tag{5.4}$$

In order the wave functions satisfy the Helmholtz equation (5.3), relations

$$\left(k_{x,\alpha}^a\right)^2 + \left(k_{y,\alpha}^a\right)^2 = \left(k_{x,\alpha}^b\right)^2 + \left(k_{y,\alpha}^b\right)^2 = \left(k_{x,\alpha}^c\right)^2 + \left(k_{y,\alpha}^c\right)^2 = \left(k_{x,\alpha}^d\right)^2 + \left(k_{y,\alpha}^d\right)^2 = k_\alpha^2 \tag{5.5}$$

between the individual wave numbers must hold.

It can be noted that there is infinite number of possibilities regarding the choice of the individual wave number pairs. An often proposed option selects the wave numbers as

$$\begin{aligned}
\left(k_{x,\alpha}^a, k_{y,\alpha}^a\right) &= \left(\frac{m_a \pi}{L_x}, \pm\sqrt{k_\alpha^2 - \left(k_{x,\alpha}^a\right)^2}\right), \; m_a = 0,1,2,\ldots,M_a \\
\left(k_{x,\alpha}^b, k_{y,\alpha}^b\right) &= \left(\frac{m_b \pi}{L_x}, \pm\sqrt{k_\alpha^2 - \left(k_{x,\alpha}^b\right)^2}\right), \; m_b = 0,1,2,\ldots,M_b \\
\left(k_{x,\alpha}^c, k_{y,\alpha}^c\right) &= \left(\pm\sqrt{k_\alpha^2 - \left(k_{y,\alpha}^c\right)^2}, \frac{m_c \pi}{L_y}\right), \; m_c = 0,1,2,\ldots,M_c \\
\left(k_{x,\alpha}^d, k_{y,\alpha}^d\right) &= \left(\pm\sqrt{k_\alpha^2 - \left(k_{y,\alpha}^d\right)^2}, \frac{m_d \pi}{L_y}\right), \; m_d = 0,1,2,\ldots,M_d
\end{aligned} \tag{5.6}$$

Symbols L_x and L_y denote the lengths of the smallest bounding box to the related element. The upper limits M_a, M_b, M_c and M_d are selected according to the chosen truncation rule.

Based on the previous discussion, the potentials Φ_α can be expanded in terms of the wave functions sets defined in eq. (5.4). As only a finite number of terms is included, this procedure results in an approximation

$$\Phi_\alpha \approx \sum_{m_a=1}^{M_a} w_{m_a}^a \Psi_\alpha^a + \sum_{m_b=1}^{M_b} w_{m_b}^b \Psi_\alpha^b + \sum_{m_c=1}^{M_c} w_{m_c}^c \Psi_\alpha^c + \sum_{m_d=1}^{M_d} w_{m_d}^d \Psi_\alpha^d. \tag{5.7}$$

The coefficients $w_\bullet^*$ are the unknown participation factors related to a single element. Note that the previously described expansion is performed for each element separately.

The displacement field components can be obtained from the approximated potentials Φ_p and Φ_s by application of eq. (3.6). Subsequently, the boundary tractions are acquired with the use

of eqs. (2.33) to (2.35). Moreover, both quantities need to be transformed to the normal and tangential directions with respect to the element boundary, since also the boundary conditions (5.1) as well as the inter-element continuity conditions (5.2) are expressed in terms of these components. Symbolically, the individual displacement and traction components, denoted by symbol a, can be expressed in terms of vector $\begin{bmatrix}\Phi_p & \Phi_s\end{bmatrix}^T$ as

$$a = \mathcal{L}_a \begin{bmatrix}\Phi_p \\ \Phi_s\end{bmatrix}, \tag{5.8}$$

where $\mathcal{L}_a$ is the specific differential operator and $a = \{u_n, u_t, t_n, t_t\}$. The individual operators $\mathcal{L}_a$ have the form

$$\begin{aligned}
\mathcal{L}_{u_n} &= \begin{bmatrix}\dfrac{\partial}{\partial n} & \dfrac{\partial}{\partial t}\end{bmatrix}, \\
\mathcal{L}_{u_t} &= \begin{bmatrix}\dfrac{\partial}{\partial t} & -\dfrac{\partial}{\partial n}\end{bmatrix}, \\
\mathcal{L}_{t_n} &= \begin{bmatrix}2\mu\dfrac{\partial^2}{\partial n^2} + \lambda\nabla^2 & 2\mu\dfrac{\partial^2}{\partial n \partial t}\end{bmatrix}, \\
\mathcal{L}_{t_t} &= \begin{bmatrix}2\mu\dfrac{\partial^2}{\partial n \partial t} & 2\mu\left(\dfrac{\partial^2}{\partial t^2} - \dfrac{\partial^2}{\partial n^2}\right)\end{bmatrix}.
\end{aligned} \tag{5.9}$$

Symbols $\dfrac{\partial}{\partial n}$ and $\dfrac{\partial}{\partial t}$ represent the normal and tangential derivative.

5.3.1 Construction of the System of Equations

The system of algebraic equations is obtained by weak imposition of the boundary as well as the inter-element continuity conditions defined in eqs. (5.1) and (5.2). For each element i_{el} the residuals are multiplied by weighting functions $\tilde{a}$ and integrated along the related boundary

$$\begin{aligned}
\int_{\Gamma_u^{(i_{el})}} \tilde{t}_n^{(i_{el})} R_{u_n}^{(i_{el})} + \tilde{t}_t^{(i_{el})} R_{u_t}^{(i_{el})} \mathrm{d}\Gamma - \int_{\Gamma_\sigma^{(i_{el})}} \tilde{u}_n^{(i_{el})} R_{t_n}^{(i_{el})} + \tilde{u}_t^{(i_{el})} R_{t_t}^{(i_{el})} \mathrm{d}\Gamma + \\
+ \sum_{j_{el}=1, j_{el}\neq i_{el}}^{n_{el}} \int_{\Gamma_I^{(i_{el},j_{el})}} \tilde{t}_n^{(i_{el})} R_{u_n}^{(i_{el},j_{el})} + \tilde{t}_t^{(i_{el})} R_{u_t}^{(i_{el},j_{el})} \mathrm{d}\Gamma + \\
- \sum_{j_{el}=1, j_{el}\neq i_{el}}^{n_{el}} \int_{\Gamma_I^{(i_{el},j_{el})}} \tilde{u}_n^{(i_{el})} R_{t_n}^{(i_{el},j_{el})} + \tilde{u}_t^{(i_{el})} R_{t_t}^{(i_{el},j_{el})} \mathrm{d}\Gamma = 0.
\end{aligned} \tag{5.10}$$

The first integral is related to the imposition of the displacement boundary condition while the second one is associated to enforcement of the traction boundary condition on element i_{el}. Furthermore, integrals along the edges which are shared with neighbouring elements j_{el} are considered. On each inter-element edge of element i_{el}, either the displacement residuals or the traction residuals are weakly enforced, the remaining option is then imposed on the neighbouring element j_{el}.

The individual weighting functions denoted by $\tilde{a}$ are expanded in terms of the same wave function

sets as the original fields

$$\tilde{a} = \mathcal{L}_a \begin{bmatrix} \tilde{\Phi}_p \\ \tilde{\Phi}_s \end{bmatrix}, \tag{5.11}$$

with

$$\tilde{\Phi}_\alpha \approx \sum_{m_a} \tilde{w}^a_{m_a} \Psi^a_\alpha + \sum_{m_b} \tilde{w}^b_{m_b} \Psi^b_\alpha + \sum_{m_c} \tilde{w}^c_{m_c} \Psi^c_\alpha + \sum_{m_d} \tilde{w}^d_{m_d} \Psi^d_\alpha. \tag{5.12}$$

The final system of algebraic equations is generated as follows: Firstly, the residuals in eqs. (5.1) and (5.2) are expressed in terms of unknown participation factors $w^*_\bullet$, which is done by substitution of eqs. (5.4), (5.7), (5.8) and (5.9). Afterwards, the residuals are substituted into eq. (5.10). Similarly, by combination of eqs. (5.11) and (5.12) also the weighting functions are expanded in terms of coefficients $\tilde{w}^*_\bullet$ and substituted into eq. (5.10). Performing such procedure for all the elements i_{el} and considering that the coefficients related to the weighting functions may be arbitrary, the system of algebraic equations is formulated with unknowns being the contribution factors of all elements. The resulting global system matrix has complex components and is generally nonsymmetric.

The individual system submatrices are constructed by integration along a portion of the element boundary. As the integrals cannot be evaluated analytically, numerical quadrature needs to be applied. Since the integrands are highly oscillatory functions, large number of quadrature points need to be considered so that the resulting approximation is sufficiently accurate.

After the system of equations is solved, the unknown contribution factors of each wave function for each element are obtained. To reconstruct the desired fields, a post-processing phase is necessary. Within each element, firstly the dilatational and shear potential fields are evaluated at the desired locations by substitution of the related coefficients $w^*_\bullet$ into eq. (5.7). Afterwards, the displacement fields can be obtained with the help of eq. (3.6) and the associated stress field is then acquired by application of eqs. (2.33) and (2.34).

5.4 Comparison of Wave Based and Hybrid-Trefftz Methods

In the following section both wave based and hybrid-Trefftz methods are compared in various categories.

Domain discretization: In the case of both methods the aim is to discretize the investigated structure into small number of large elements. As for both techniques the system matrices are constructed by integration along the element boundary, it is advantageous to keep the length of all element boundaries as small as possible, which is accomplished by reduction of the number of elements. Moreover, in the case of both methods, the complexity of the resulting system of equations is reduced when p-refinement techniques are adopted instead of the h-refinement ones. This means that to achieve the desired accuracy of the results, it proves to be more efficient to increase the number of functions in the approximation basis rather than increase the number of

elements. However, in the case of the hybrid-Trefftz method, when the elements are too large, and hence for a sufficient accuracy a large number of basis functions needs to be included, the resulting equation system turns out to be ill-conditioned. To overcome such issue, h-refinement technique needs to be applied.

Domain complexity: When complex shapes are modelled, the domain needs to be partitioned in many elements, which results in an increase of the inter-element boundary length as well as of the number of degrees of freedom. Overall, the computational cost of both methods is too large for such cases and perhaps different modelling strategy should be adopted instead. Furthermore, in the case of WBM, the necessary requirement for the method to converge is the element convexity. Therefore, some domain shapes, such as structures with circular holes, even cannot be divided into convex subdomains. This property makes to method even less applicable for modelling of complex domains.

Approximated fields and basis functions: In the case of both methods the displacement field is approximated inside the element domain. Moreover, the basis functions are required to satisfy the governing differential equation. The functions contained in the WBM basis are constructed as solutions of the Helmholtz equation expressed directly in Cartesian coordinates. On the other hand, the basis for the hybrid-Trefftz method is obtained by solving the Helmholtz equation in polar reference frame. Furthermore, in the case of the hybrid-Trefftz method, the tractions on the Dirichlet and inter-element boundary are additionally approximated. The basis for the such approximation is constructed using the Chebyshev polynomials.

Construction of the system of equations: In the case of WBM, the system of equations is constructed by weak imposition of the boundary as well as the inter-element continuity conditions. The displacement and traction residuals are multiplied by weighting functions and integrated along the related portion of the boundary. In the case of hybrid-Trefftz method, the finite element system of equations is generated as follows: The equilibrium equations are weakly imposed in the element domain, while the material law and the kinematic equations are satisfied strongly. Furthermore, the traction boundary approximation and the traction boundary conditions are substituted. All the equations are combined and the first matrix equation of the final system is formed. The second one is constructed by weak imposition of the displacement boundary and inter-element continuity conditions, while the boundary traction approximation basis is used as the weighting matrix. The individual submatrices in the case of both methods are constructed by integration of highly oscillatory functions along the element boundary, hence a large number of quadrature points must be considered so that the integrals are approximated accurately.

Resulting system of equations and number of degrees of freedom: The resulting global system matrices have complex components for both compared methods. The matrix associated to the hybrid-Trefftz method is Hermitian, which is an advantageous property, when iterative solvers are applied during the solution procedure. The number of degrees of freedom, and hence the size of the system of equations, related to both methods is generally small when compared to systems obtained with other methods, such as FEM. In the case of the hybrid-Trefftz method, additional degrees of freedom are introduced for the approximation of the boundary tractions. Therefore, the size of the resulting system is larger compared to the one acquired with WBM, when the number

of domain basis functions is kept the same. For both methods, the unknown coefficients represent the contribution factors of the related basis functions to the final solution. This implies that to recover the desired field of interest, post-processing is required, in which the basis functions are evaluated at the investigated locations and multiplied by the computed coefficients.

The main points are summarized in tab. 5.1.

	WBM	Hybrid-Trefftz method
Approximated fields in element domain	Displacements	Displacements
Domain basis functions	Satisfy the Lamé equation, solved in Cartesian reference frame	Satisfy the Lamé equation, solved in polar reference frame
Approximated fields on element boundary	None	Tractions
Construction of the system of equations	Prescribed boundary and continuity conditions weakly enforced on element boundary	Weak imposition of the equilibrium equations in element domain, substitution of the material law, kinematic equations, traction approximation and traction boundary condition, weak enforcement of the displacement boundary and continuity conditions on element boundary
System matrices evaluation	Integration along element boundary	Integration along element boundary
Degrees of freedom	Contribution factors of the individual wave functions in each element	Contribution factors of the individual basis functions in each element and coefficients related to the boundary traction approximation
Properties of the system of equations	Complex	Complex, Hermitian
Element shape requirements	Convex	None

Table 5.1: Comparison of WBM and hybrid-Trefftz method

6 Implementation

Most of the theoretical aspects related to the analysis of loaded elastodynamic media were described in the previous chapters. The hybrid-Trefftz finite element system of equations was derived using the weighted residual method and the modification of the system for unbounded problems was introduced. The following chapter is dedicated to the implementation of the previously discussed theoretical concepts.

The programming aspects of the Trefftz finite element method are discussed in [Qin and Wang 2008], where the implementation is described for potential problems as well as for plane elasticity.

Firstly, the topic of numerical integration is introduced, since it is a necessary mathematical tool enabling an efficient implementation of the described method. Subsequently, implemented elements are mentioned and relations for description of the element geometry are derived. The third and last section of the chapter is devoted to a detailed description of the implemented code and its structure.

6.1 Numerical Integration

All the system matrices and vectors appearing in the governing system of equations (4.49) are defined as integrals over the element boundary or a portion of it. For elements of a general shape it is infeasible to perform the integration analytically and therefore numerical quadrature rules need to be applied instead.

Let s be the coordinate running along a single element edge and l be the length of the edge. Integral of an arbitrary function $g(x,y)$ over the single edge is approximated as

$$\int_0^l g(x,y)\,\mathrm{d}s \approx \sum_{k=1}^{q} w_k g(x_k,y_k), \tag{6.1}$$

where q denotes the order of the quadrature, (x_k,y_k) are the quadrature points and w_k are the corresponding quadrature weights. As quadrature rules are defined in terms of the normalized coordinate $\xi \in \langle -1,1 \rangle$, the previous equation is modified

$$\int_0^l g(x,y)\,\mathrm{d}s = \int_{-1}^{1} g\left(x(\xi),y(\xi)\right) \frac{\mathrm{d}s}{\mathrm{d}\xi}\mathrm{d}\xi \approx \sum_{k=1}^{q} w_k g(x(\xi_k),y(\xi_k))J(\xi_k), \tag{6.2}$$

where ξ_k denotes the quadrature points in 1D normalized reference frame. In the previous equation the integral over the single edge was transformed to integral performed over the normalized coordinate ξ, which was done by expanding the differential segment $\mathrm{d}s$ using the chain rule. The

term $\mathrm{d}s/\mathrm{d}\xi$ is referred to as the Jacobian J. The mapping between the side coordinate ξ and the spatial coordinates $x(\xi)$ and $y(\xi)$ needs to be defined based on the particular element boundary shape.

To evaluate the Jacobian, the differential boundary segment $\mathrm{d}s$ is firstly expressed in terms of the differential Cartesian segments $\mathrm{d}x$ and $\mathrm{d}y$, which are then with the use of the chain rule expanded in terms of the coordinate ξ

$$\mathrm{d}s = \sqrt{\mathrm{d}x^2 + \mathrm{d}y^2} = \sqrt{\left(\frac{\mathrm{d}x}{\mathrm{d}\xi}\mathrm{d}\xi\right)^2 + \left(\frac{\mathrm{d}y}{\mathrm{d}\xi}\mathrm{d}\xi\right)^2} = \sqrt{\left(\frac{\mathrm{d}x}{\mathrm{d}\xi}\right)^2 + \left(\frac{\mathrm{d}y}{\mathrm{d}\xi}\right)^2}\mathrm{d}\xi. \tag{6.3}$$

Therefore the Jacobian results in

$$J = \frac{\mathrm{d}s}{\mathrm{d}\xi} = \sqrt{\left(\frac{\mathrm{d}x}{\mathrm{d}\xi}\right)^2 + \left(\frac{\mathrm{d}y}{\mathrm{d}\xi}\right)^2}. \tag{6.4}$$

The exact relation for the Jacobian hence depends on the shape of the boundary and the specific form of the mapping between the side coordinate and the Cartesian reference frame.

In this work the Gauss-Legendre quadrature rule is chosen. For q integration points a polynomial of order $2q-1$ is integrated exactly. The integration points and weights can be obtained by the application of the Golub-Welsch algorithm [Golub and Welsch 1969].

6.2 Implemented Elements

In this section the implemented element types are discussed and the particular form of the mapping between the side coordinate ξ and the Cartesian coordinates x and y of the points on the element edge is introduced. Subsequently, the derivative of such mapping is derived so that the Jacobian defined in eq. (6.3) can be computed. In addition, components of the unit normal at the point on the boundary are expressed, since such information is necessary for computation of some of the system matrices.

In chapter 3 it was mentioned that elements of arbitrary shape and with optional number of edges can be used. However, for simplicity, in this work only elements with straight or circular edges were implemented. In the following subsections both formulations are explained in detail.

6.2.1 Element with Straight Edges

Assume index $i = 1,2,\ldots,n_{no}$ runs over the element nodes with n_{no} being the number of element nodes. Since a straight edge is completely defined be two neighbouring nodes, number of edges n_{ed} corresponds to the number of nodes, therefore $n_{ed} = n_{no}$. In the case of straight edge, the geometry can be described using the linear shape functions. Therefore, an arbitrary point on the

edge between nodes i and $i+1$ can be obtained as

$$x = \begin{bmatrix} \frac{1-\xi}{2} & \frac{1+\xi}{2} \end{bmatrix} \begin{bmatrix} x_i \\ x_{i+1} \end{bmatrix}, \tag{6.5}$$

$$y = \begin{bmatrix} \frac{1-\xi}{2} & \frac{1+\xi}{2} \end{bmatrix} \begin{bmatrix} y_i \\ y_{i+1} \end{bmatrix}, \tag{6.6}$$

where (x_i,y_i) are the coordinates of ith node. For the computation of the Jacobian, the derivatives with respect to ξ coordinate need to be expressed as well

$$\frac{\mathrm{d}x}{\mathrm{d}\xi} = \begin{bmatrix} -\frac{1}{2} & \frac{1}{2} \end{bmatrix} \begin{bmatrix} x_i \\ x_{i+1} \end{bmatrix}, \tag{6.7}$$

$$\frac{\mathrm{d}y}{\mathrm{d}\xi} = \begin{bmatrix} -\frac{1}{2} & \frac{1}{2} \end{bmatrix} \begin{bmatrix} y_i \\ y_{i+1} \end{bmatrix}. \tag{6.8}$$

Components of the outward unit normal vector $\boldsymbol{n} = \begin{bmatrix} n_x & n_y \end{bmatrix}^T$ are then calculated as

$$\begin{aligned} n_x =& \frac{\mathrm{d}y}{\mathrm{d}s} = \frac{\mathrm{d}y}{\mathrm{d}\xi}\frac{\mathrm{d}\xi}{\mathrm{d}s} = \frac{1}{J}\frac{\mathrm{d}y}{\mathrm{d}\xi}, \\ n_y =& -\frac{\mathrm{d}x}{\mathrm{d}s} = -\frac{\mathrm{d}x}{\mathrm{d}\xi}\frac{\mathrm{d}\xi}{\mathrm{d}s} = -\frac{1}{J}\frac{\mathrm{d}x}{\mathrm{d}\xi}. \end{aligned} \tag{6.9}$$

It is important to stress that the concept of nodal interpolation is only applied for the description of the geometry of the element. As was mentioned in chapter 3, the domain displacement and boundary traction approximation bases are strictly hierarchical and their exact form was derived earlier.

6.2.2 Element with Circular Edges

The situation gets more complex when a circular edge is considered. In such case, not only coordinates of the two neighbouring nodes are sufficient to define the geometry of the edge, but additional information regarding the coordinates of the center $(x_{c,j},y_{c,j})$ of the circular edge needs to be provided. Index j runs over all circular edges belonging to a certain element. To define the mapping from the coordinate ξ to the Cartesian coordinates of points on the edge, the radius r, starting angle α_0 and ending angle α_1 need to be calculated first. α_0 indicates the positive angle between the x-axis and the position of node i. Similarly, α_1 stands for the positive angle between x-axis and the position of node $i+1$. The geometry of a single edge j is depicted in fig. 6.1. The formulas for calculation of the mentioned parameters read as

$$r = \sqrt{(x_i - x_{c,j})^2 + (y_i - y_{c,j})^2}, \tag{6.10}$$

$$\alpha_0 = \mathrm{atan2}(y_i - y_{c,j}, x_i - x_{c,j}), \tag{6.11}$$

$$\alpha_1 = \mathrm{atan2}(y_{i+1} - y_{c,j}, x_{i+1} - x_{c,j}). \tag{6.12}$$

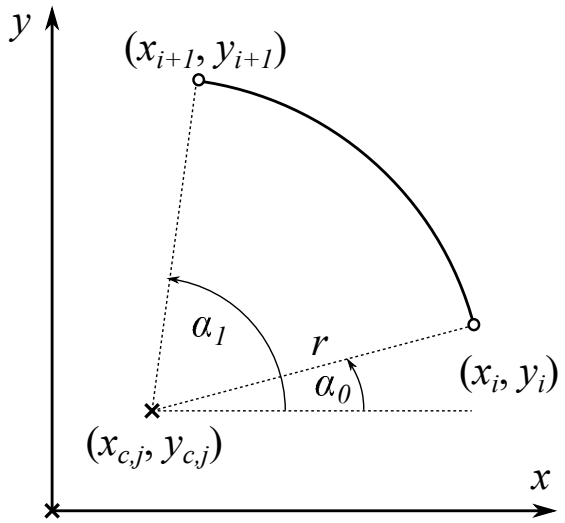

Figure 6.1: Circular edge geometry

Afterwards, for the given coordinate ξ, the position of a point on the edge is calculated as

$$x = x_{c,j} + r\cos\Big(\alpha_0 + \frac{1+\xi}{2}(\alpha_1 - \alpha_0)\Big), \tag{6.13}$$

$$y = y_{c,j} + r\sin\Big(\alpha_0 + \frac{1+\xi}{2}(\alpha_1 - \alpha_0)\Big). \tag{6.14}$$

To obtain the derivatives of the spatial coordinates with respect to the side coordinate, the previous relations are differentiated

$$\frac{\mathrm{d}x}{\mathrm{d}\xi} = -r\frac{\alpha_1 - \alpha_0}{2}\sin\Big(\alpha_0 + \frac{1+\xi}{2}(\alpha_1 - \alpha_0)\Big), \tag{6.15}$$

$$\frac{\mathrm{d}y}{\mathrm{d}\xi} = r\frac{\alpha_1 - \alpha_0}{2}\cos\Big(\alpha_0 + \frac{1+\xi}{2}(\alpha_1 - \alpha_0)\Big). \tag{6.16}$$

The Jacobian can subsequently be calculated using eq. (6.4), which results in

$$J = \sqrt{\Big(\frac{\mathrm{d}x}{\mathrm{d}\xi}\Big)^2 + \Big(\frac{\mathrm{d}y}{\mathrm{d}\xi}\Big)^2} = r\frac{\alpha_1 - \alpha_0}{2}. \tag{6.17}$$

The components of the outward normal are expressed by eq. (6.9), substituting the individual terms yields

$$\begin{aligned} n_x &= \frac{1}{J}\frac{\mathrm{d}y}{\mathrm{d}\xi} = \cos\Big(\alpha_0 + \frac{1+\xi}{2}(\alpha_1 - \alpha_0)\Big), \\ n_y &= -\frac{1}{J}\frac{\mathrm{d}x}{\mathrm{d}\xi} = \sin\Big(\alpha_0 + \frac{1+\xi}{2}(\alpha_1 - \alpha_0)\Big). \end{aligned} \tag{6.18}$$

The previously derived formulas completely define the mapping between the normalized side coordinate ξ and the Cartesian coordinates of points located at the element edge. Therefore, the

system matrices can be approximated using the numerical quadrature rule by the application of eq. (6.2). For the case of a straight edge, only coordinates of the two end nodes are the necessary input. For a circular edge, coordinates of the center needs to be provided additionally. The number of element edges may be arbitrary. In the thesis only elements with four edges are implemented, however, generalization for optional number of edges is straightforward.

So far no comments were placed regarding the position of the Cartesian reference frame used for the derivation of above formulas. Two options are implemented in this work. One possibility is to consider the xy-reference frame as the global one and formulate the relations for all elements in terms of this single coordinate system. In such case, the coordinates (x_i,y_i) of nodes of a single element also correspond to their global coordinates.

The other option is to consider the xy-reference frame as the local coordinate system placed at the element center. For such case, assume there exists a different global reference frame with axis x^G and y^G. In addition, (x_i^G,y_i^G) are the coordinates of the nodes of a single element and $(x_{c,i}^G,y_{c,i}^G)$ are the global coordinates of the center of the circular edges. The position of the geometrical center of the element is calculated as

$$x_{centre}^G = \frac{1}{n_{no}} \sum_{i=1}^{n_{no}} x_i^G, \tag{6.19}$$

$$y_{centre}^G = \frac{1}{n_{no}} \sum_{i=1}^{n_{no}} y_i^G. \tag{6.20}$$

Subsequently, the element nodal coordinates in the local reference frame are obtained as

$$x_i = x_i^G - x_{centre}^G, \tag{6.21}$$

$$y_i = y_i^G - y_{centre}^G. \tag{6.22}$$

Similarly, when a circular edge is considered, the coordinates of the center of the edge are expressed as

$$x_{c,i} = x_{c,i}^G - x_{centre}^G, \tag{6.23}$$

$$y_{c,i} = y_{c,i}^G - y_{centre}^G. \tag{6.24}$$

Note that such transformation has no influence on the value of the Jacobian or on the components of the unit normal, it only affects the location of points on the element boundary, which are now shifted by the position of the element center.

The application of the second option together with incorporation of scaling procedures of the final system of equations often results in reduction of the numerical error caused by ill-conditioned global system matrix.

6.3 Program Structure

The program is implemented in software MATLAB. The reason for the choice of interpretive programming language is the wide range of inbuilt functions and commands, which makes the programming and visualization process faster and easier compared to compiled languages such as C or C++. On the other hand, this comes with a cost of greater run time. However, for the objective of this thesis such drawback is acceptable.

The program workflow can be divided into the following sections: data input, computation of the system matrices, solution of the system of equations and post-processing and visualization. Each of these procedures is described in detail in the subsequent sections.

6.3.1 Data Input

All the necessary data are input from a text file. It needs to contain information related to material properties, geometry, loading, boundary conditions, approximation bases and number of Gauss points.

The material properties consist of the Young modulus, Poisson's ratio, loss factor and the mass density. The Lamé parameters can then be calculated based on the formulas provided in chapter 2 and subsequently, the wave velocities can be evaluated.

It is assumed that the domain of interest is already discretized into finite elements and therefore the meshing procedure is skipped. In the input file, for each element, indices of the related nodes need to be provided and also Cartesian coordinates of each node are given. By default it is assumed that the element edges are straight. Additionally, a list of circular edges is included in the input file, containing the indices of the related end nodes and Cartesian coordinates of the centres of the circular edges. Furthermore, as was mentioned in the previous section, information regarding the choice of the reference frame for the evaluation of points on the boundary is attended.

The loading is defined by a list of loaded edges. For each loaded edge, index of the related element together with indices of the edge end nodes are provided. Only distributed loading varying linearly is implemented, hence it can be completely defined by the values of the loading at the end nodes of the edge. This information is also given for each edge in the list. Moreover, the frequency of excitation needs to be mentioned in the input file so that the wave numbers can be computed.

Constrained edges are defined in a similar way as the loaded edges. In the list of constrained edges, related element index as well as indices of the end nodes are mentioned. For each constrained edge, values of the prescribed displacements are included. In addition, if the constrained edge is of mixed type, the fixed degree of freedom is marked. In the case an unbounded domain is analysed, a list of edges on which the absorbing boundary condition is considered needs to be given. The edges are again defined by the index of the related element and by indices of the end nodes.

Information related to the approximation bases need to contain the length of both domain displacement and boundary traction bases. Moreover, the type of the Bessel solution function needs to be indicated. The number of terms contained in the domain approximation basis is calculated from the maximum order N of the Bessel solution function W_n, which is discussed in section 3.2.1. Therefore, maximum order of the Bessel solution function is included in the input file. Similarly,

the length of the boundary approximation basis can be deduced from the maximum order M of the polynomial included in the basis, which is hence provided as the input.

6.3.2 System Matrices Computation

After the necessary data are obtained, the process of building the system of equations may start. All the matrices and vectors which appear in the global system of equations (4.50) are gradually assembled. This procedure is discussed in detail in the following sections.

For the implementation, it is assumed no body forces are applied on the analysed structure. This implies that the vector of particular solution $\boldsymbol{u_0}$, appearing in eq. (3.1), vanishes. Consequently, also vectors $\overline{\boldsymbol{t_{\Gamma_{0,G}}}}$ and $\overline{\boldsymbol{u_{a_{0,G}}}}$, which are included in the right hand side of the governing system of equations (4.50), have zero components only. Furthermore, in the definition of vector $\overline{\boldsymbol{u_{\Gamma_G}}}$ all the terms $\overline{\boldsymbol{u_{\Gamma_0}}}_i^{(j)}$ are neglected. Moreover, in the case the mixed boundary condition is applied, it is assumed that the prescribed traction component is zero, hence also the vectors $\overline{\boldsymbol{t_{\Gamma m}}}$ or $\overline{\boldsymbol{t'_{\Gamma m}}}$ appearing in eqs. (3.107) and (3.127) vanish.

Global D_G Matrix

The global $\boldsymbol{D_G}$ matrix is composed from the local $\boldsymbol{D}^{(i_{el})}$ matrices evaluated for each element in the way described by eq. (3.86). Therefore, in the code there is a loop over all elements, in which the individual $\boldsymbol{D}^{(i_{el})}$ matrices are computed and afterwards assembled to the allocated $\boldsymbol{D_G}$ matrix.

The single $\boldsymbol{D}^{(i_{el})}$ matrix is evaluated based on the definition in eq. (3.59). The integration needs to be performed over the whole element boundary, however, the integral can be split into multiple integrals over the individual edges. The edge integrals are then approximated using the Gauss-Legendre quadrature of the given order q, which is expressed by eq. (6.2). This procedure is illustrated as

$$\boldsymbol{D} = \int \widehat{\boldsymbol{U}}^T \boldsymbol{N}\boldsymbol{k}\boldsymbol{E}\,\mathrm{d}\Gamma^e = \sum_{j=1}^{n_{ed}} \int_0^{l_j} \widehat{\boldsymbol{U}}^T \boldsymbol{N}\boldsymbol{k}\boldsymbol{E}\,\mathrm{d}s_j \approx \sum_{j=1}^{n_{ed}} \sum_{k=1}^{q} w_k \widehat{\boldsymbol{U}}^T(\xi_k)\boldsymbol{N}(\xi_k)\boldsymbol{k}\boldsymbol{E}(\xi_k)J_j(\xi_k), \quad (6.25)$$

where j is an index running over the element edges, s_j denotes an individual edge coordinate, l_j is the length of the edge j and J_j stands for the Jacobian related to the particular edge.

The implemented function for the computation of the individual $\boldsymbol{D}^{(i_{el})}$ matrices consists of two nested loops, one running over the element edges and the second one over the number of integration points. Firstly, for each integration point k the related weight w_k and point coordinate ξ_k are obtained. Afterwards, Cartesian coordinates of the associated Gauss point together with the components of the unit normal and value of the Jacobian are acquired. These values are calculated based on the formulas derived in sections 6.2.1 and 6.2.2. It is however necessary to firstly check, if the current evaluated edge is circular, so that the correct formulation is chosen. Moreover, if the local reference frame was chosen for the evaluation of points on the boundary, the global nodal coordinates as well as the global positions of the center of the circular edges need to be transformed to the local coordinate system, which is described by eqs. (6.19) to (6.24).

Subsequently, when the Cartesian coordinates of the quadrature points are known, the displacement and strain bases $\boldsymbol{U}(x(\xi_k),y(\xi_k))$ and $\boldsymbol{E}(x(\xi_k),y(\xi_k))$ can be evaluated by implementation of the formulas mentioned in section 3.2.2. The number of terms contained in the basis strictly depends on the chosen maximum order N of the Bessel solution function.

The material matrix $\boldsymbol{k}$ has constant components and therefore can be evaluated outside of both loops. Afterwards, as all the required terms are known, the contribution of a single gauss point to the complete integral appearing in eq. (6.25) can be calculated and next iteration may proceed. This scheme is repeated until all the edges and integration points are considered. The overall procedure of evaluation of the matrix $\boldsymbol{D_G}$ is illustrated by the following pseudocode:

1. Allocate $\boldsymbol{D_G}$
2. Loop over all elements i_{el}
   a) Obtain nodal coordinates
      - If local reference frame is chosen $\rightarrow$ transform the nodal coordinates
   b) Compute $\boldsymbol{D}^{(i_{el})}$
      i. Allocate $\boldsymbol{D}^{(i_{el})}$
      ii. Compute material matrix $\boldsymbol{k}$
      iii. Loop over element edges
         A. Loop over integration points k
            - Evaluate position of the Gauss point, the components of the unit normal and the Jacobian
            - Evaluate bases $\boldsymbol{U}(x(\xi_k),y(\xi_k))$ and $\boldsymbol{E}(x(\xi_k),y(\xi_k))$ at the Gauss point location
            - Compute the contribution of the integration point and add it to the existing matrix: $\boldsymbol{D}^{(i_{el})} = \boldsymbol{D}^{(i_{el})} + w_k \widehat{\boldsymbol{U}}^T \boldsymbol{N}\boldsymbol{k}\boldsymbol{E} J_j$
   c) Assemble $\boldsymbol{D}^{(i_{el})}$ to $\boldsymbol{D_G}$

When choosing the reference frame for evaluation of the element matrices, one needs to be aware that the Bessel function of the second kind or any of the Hankel functions are singular at the origin. Therefore, if any of the aforementioned Bessel solution functions is chosen for the radial component W_n appearing in the definition of the bases $\boldsymbol{U}$ or $\boldsymbol{E}$, the origin of the chosen reference frame needs to be placed outside of the element. This implies that in such case only the option of the global reference frame needs to be adopted, since the local one is placed at the center of the element.

As is evident from the previous discussion, the individual $\boldsymbol{D}^{(i_{el})}$ matrices are approximated by the sum of weighted evaluations of the integrand multiplied by the Jacobian. This procedure contains evaluation of the bases $\boldsymbol{U}(x,y)$ and $\boldsymbol{E}(x,y)$, and therefore evaluation of the Bessel solution functions at positions on the boundary. As the Bessel functions of the first kind and of high orders n tend to get flatter in the vicinity of origin, some components of the evaluated bases are almost zero, when large number of terms is considered in the approximation basis and the evaluation position is

located close to the origin of the reference frame. As an outcome, matrices $\boldsymbol{D}^{(i_{el})}$ and consequently the global $\boldsymbol{D_G}$ matrix collect components of varying orders of magnitude, which results in badly conditioned system of equations. Such outcome motivates to apply certain scaling procedures of the final system of equations in order to diminish the resulting numerical error.

To a certain extend, the condition number of the matrix $\boldsymbol{D_G}$ could be reduced by placing the global reference frame sufficiently far from all elements. However, for such case the implemented scaling of the final system of equations does not improve the condition number as much. Overall, it turns out that the combination of using the Bessel functions of the first kind with local reference frame and applying the scaling procedure described in section 6.3.3 results in the system of equations with the lowest condition number of all the considered options.

Global B_G Matrix

As was discussed in section 3.4.6, the global $\boldsymbol{B_G}$ matrix is assembled from the individual $\boldsymbol{B}_j^{(i_{el})}$ matrices evaluated for edge j belonging to element i_{el}. All edges on which the displacement boundary condition is applied together with the inter-element edges are considered for the evaluation. In the implemented algorithm, firstly the list of all the mentioned edges containing the related element index is obtained and then the matrix $\boldsymbol{B_G}$ is allocated. Subsequently, loop over the listed edges is performed, in which the individual $\boldsymbol{B}_j^{(i_{el})}$ matrices are evaluated. Afterwards, the individual matrices are assembled to the global one, the element index i_{el} corresponds to the row and the edge index j to the column in the resulting global matrix.

The single $\boldsymbol{B}_j^{(i_{el})}$ matrix is computed using the definition in eq. (3.75). By the application of the numerical quadrature rule, the integral is approximated as

$$\boldsymbol{B}_j^{(i_{el})} = \int \widehat{\boldsymbol{U}^{(i_{el})}}^T \boldsymbol{Z}\, \mathrm{d}\Gamma^e_{u_j} = \int_0^{l_j} \widehat{\boldsymbol{U}^{(i_{el})}}^T \boldsymbol{Z}\, \mathrm{d}s_j \approx \sum_{k=1}^{q} w_k \widehat{\boldsymbol{U}^{(i_{el})}}^T (x(\xi_k),y(\xi_k))\boldsymbol{Z}(\xi_k) J_j(\xi_k), \quad (6.26)$$

where s_j denotes the coordinate running along the single edge j and l_j stands for the length of the edge.

The function for computation of the single $\boldsymbol{B}_j^{(i_{el})}$ matrix contains a loop over the integration points k. For each Gauss point the coordinates in the chosen reference frame are calculated as well as the value of the Jacobian. Afterwards, the displacement basis $\boldsymbol{U}(x(\xi_k),y(\xi_k))$ can be evaluated at the position of the quadrature points. In addition, also the boundary approximation basis $\boldsymbol{Z}(\xi_k)$ is evaluated, since it is defined in terms of the coordinate ξ, the position of the Gauss point ξ_k can directly be inserted. Subsequently, the contribution of the single integration point to the overall sum appearing in eq. (6.26) can be computed.

It was mentioned in section 3.4.6 that for the inter-element edges, two $\boldsymbol{B}_j^{(i_{el})}$ matrices are evaluated, sharing the same edge index j but differing with the element index i_{el}. In the assembly process, the sign of those two matrices must be the opposite, which results from enforcement of the displacement continuity condition. Therefore, in the algorithm it needs to be checked, if the matrix for the common edge was already evaluated for the neighbouring element, and if yes, the second matrix needs to be multiplied by the minus sign.

In the case the mixed boundary condition is applied on the current edge j, matrix $\boldsymbol{B}_j^{(i_{el})}$ needs to be replaced by $\boldsymbol{B}_{\boldsymbol{m}j}^{(i_{el})}$, which was defined in eq. (3.108). A way of implementing such modification is to discard half of the columns of the matrix $\boldsymbol{Z}$ related to the unconstrained degree of freedom. In addition, in the general case of mixed boundary condition, when the displacement is fixed in normal or tangential direction, the matrix $\boldsymbol{B}_j^{(i_{el})}$ is replaced by matrix $\boldsymbol{B'}_{\boldsymbol{m}j}^{(i_{el})}$, which is defined in eq. (3.125). In such situation the only difference compared to the previous case is that the components of the displacement approximation basis need to be transformed to normal and tangential directions, which is described by eq. (3.120). Otherwise the procedure is identical.

The algorithm for computation of the $\boldsymbol{B_G}$ matrix can be summarized by the following pseudocode.

1. Obtain list of all Dirichlet (constrained and inter-element) edges
2. Allocate $\boldsymbol{B_G}$ matrix
3. Loop over all Dirichlet edges j
   a) Get related element index i_{el} and corresponding nodal coordinates
      - If local reference frame is chosen → transform the nodal coordinates
   b) Compute $\boldsymbol{B}_j^{(i_{el})}$
      i. Allocate $\boldsymbol{B}_j^{(i_{el})}$
      ii. Loop over integration points k
         A. Evaluate position of the Gauss point, the components of the unit normal and the Jacobian
         B. Evaluate bases $\boldsymbol{U}(x(\xi_k),y(\xi_k))$ at the Gauss point location ξ_k
            - If the general case of mixed boundary condition is applied → transform the basis as: $\boldsymbol{U} = \boldsymbol{T}^T\boldsymbol{U}$
         C. Evaluate bases $\boldsymbol{Z}(\xi_k)$ at the Gauss point location ξ_k
            - If only one displacement component is prescribed → keep only half of the matrix $\boldsymbol{Z}$
         D. Compute the contribution of the integration point and add it to the existing matrix: $\boldsymbol{B}_j^{(i_{el})} = \boldsymbol{B}_j^{(i_{el})} + w_k\widehat{\boldsymbol{U}}^T\boldsymbol{Z}J_j$
            - If the edge was already evaluated for the neighbouring element → multiply to Gauss point contribution by the minus sign: $\boldsymbol{B}_j^{(i_{el})} = \boldsymbol{B}_j^{(i_{el})} - w_k\widehat{\boldsymbol{U}}^T\boldsymbol{Z}J_j$
   c) Assemble $\boldsymbol{B}_j^{(i_{el})}$ to $\boldsymbol{B_G}$

Global $D_{a,G}$ and $B_{a,G}$ Matrices

The matrices $\boldsymbol{D_{a,G}}$ and $\boldsymbol{B_{a,G}}$, related to the absorbing boundary condition, are defined in section 4.2.4. Both are assembled from the individual $\boldsymbol{D}_{\boldsymbol{a}j_a}$ and $\boldsymbol{B}_{\boldsymbol{a}j_a}^{(i_{el})}$ matrices evaluated for absorbing boundary edges j_a. The algorithm therefore contains a loop over all edges j_a, on which the absorbing

boundary condition is applied. For each edge, firstly the element index and the associated nodal coordinates are obtained. In the case the local reference frame is adopted, the coordinates are transformed. Afterwards, individual $\boldsymbol{D}_{\boldsymbol{a}j_a}$ and $\boldsymbol{B}_{\boldsymbol{a}j_a}^{(i_{el})}$ matrices are computed and assembled to their global counterparts.

The single $\boldsymbol{D}_{\boldsymbol{a}j_a}$ matrix is defined in eq. (4.44). The integral over the absorbing edge is approximated using the numerical quadrature rule

$$\boldsymbol{D}_{\boldsymbol{a}j_a} = \int \boldsymbol{Z}_{\boldsymbol{a}}^T \boldsymbol{C}^{\boldsymbol{x},\boldsymbol{y}-1} \boldsymbol{Z}_{\boldsymbol{a}} \,\mathrm{d}\Gamma_{a_j}^e = \int_0^{l_{j_a}} \boldsymbol{Z}_{\boldsymbol{a}}^T \boldsymbol{C}^{\boldsymbol{x},\boldsymbol{y}-1} \boldsymbol{Z}_{\boldsymbol{a}} \,\mathrm{d}s_{j_a} = \sum_{k=1}^{q} w_k \boldsymbol{Z}_{\boldsymbol{a}}^T(\xi_k) \boldsymbol{C}^{\boldsymbol{x},\boldsymbol{y}-1}(\xi_k) \boldsymbol{Z}_{\boldsymbol{a}}(\xi_k) J_{j_a}(\xi_k), \tag{6.27}$$

where s_{j_a} denotes the coordinate running along the single absorbing edge j_a and l_{j_a} stands for the length of the edge. The function for computation of the single $\boldsymbol{D}_{\boldsymbol{a}j_a}$ matrix therefore consists of a loop over all integration points. For each Gauss point, the Jacobian and components of unit normal are expressed together with the basis $\boldsymbol{Z}_{\boldsymbol{a}}(\xi_k)$. Matrix $\boldsymbol{C}^{\boldsymbol{x},\boldsymbol{y}}$ is calculated based on eq. (4.40), in which the matrix $\boldsymbol{C}$ (defined in eq. (4.32)) is transformed. As $\boldsymbol{C}$ has constant components, it can be evaluated outside of the loop. Symbol h, appearing in definition of matrix $\boldsymbol{C}$, represents the kind of the Hankel function for which the Dirichlet-to-Neumann map was derived. The sign of the imaginary part of the wave numbers is the decisive factor for the choice of the Hankel function kind h, which is thoroughly discussed in section 4.2.1. After all the matrices are computed for the current Gauss point, its contribution to the complete sum can be evaluated and the code may proceed to the next iteration.

The process of computation of the single matrix $\boldsymbol{B}_{\boldsymbol{a}j_a}^{(i_{el})}$ is very similar to the evaluation of matrix $\boldsymbol{B}_j^{(i_{el})}$, which is described above. Since the absorbing boundary edges cannot be shared by two elements and no mixed boundary condition is applied there, the function for evaluation of $\boldsymbol{B}_{\boldsymbol{a}j_a}^{(i_{el})}$ is simplified.

The algorithm for computation of the global system matrices related to absorbing boundary edges can be summarized by the following pseudocode.

1. Allocate matrices $\boldsymbol{D}_{\boldsymbol{a},\boldsymbol{G}}$ and $\boldsymbol{B}_{\boldsymbol{a},\boldsymbol{G}}$
2. Loop over all edges j_a on the absorbing boundary
   a) Get related element index i_{el} and the corresponding nodal coordinates
      - If local reference frame is chosen → transform the nodal coordinates
   b) Compute $\boldsymbol{D}_{\boldsymbol{a}j_a}$
      i. Allocate $\boldsymbol{D}_{\boldsymbol{a}j_a}$
      ii. Compute matrix $\boldsymbol{C}$
      iii. Loop over integration points k
         A. Evaluate components of unit normal and the Jacobian at the current Gauss point

B. Evaluate bases $\boldsymbol{Z_a}(\xi_k)$ at the Gauss point location ξ_k

C. Calculate matrix $\boldsymbol{C^{x,y}}$ and invert it

D. Compute the contribution of the integration point and add it to the existing matrix: $\boldsymbol{D_{a\,j_a}} = \boldsymbol{D_{a\,j_a}} + w_k \boldsymbol{Z_a^T} \boldsymbol{C^{x,y\,-1}} \boldsymbol{Z_a} J_{j_a}$

c) Compute $\boldsymbol{B_{a\,j_a}^{(i_{el})}}$

i. Allocate $\boldsymbol{B_{a\,j_a}^{(i_{el})}}$

ii. Loop over integration points k

A. Evaluate position of the Gauss point and the Jacobian

B. Evaluate bases $\boldsymbol{U}(x(\xi_k),y(\xi_k))$ at the Gauss point location ξ_k

C. Evaluate bases $\boldsymbol{Z_a}(\xi_k)$ at the Gauss point location ξ_k

D. Compute the contribution of the integration point and add it to the existing matrix: $\boldsymbol{B_{a\,j_a}^{(i_{el})}} = \boldsymbol{B_{a\,j_a}^{(i_{el})}} + w_k \widehat{\boldsymbol{U}}^T \boldsymbol{Z_a} J_{j_a}$

d) Assemble $\boldsymbol{D_{a\,j_a}}$ to $\boldsymbol{D_{a,G}}$

e) Assemble $\boldsymbol{B_{a\,j_a}^{(i_{el})}}$ to $\boldsymbol{B_{a,G}}$

Global Vector $\overline{\boldsymbol{t_{\Gamma_G}}}$

The global vector $\overline{\boldsymbol{t_{\Gamma_G}}}$ is assembled from the individual $\overline{\boldsymbol{t_\Gamma}}^{(i_{el})}$ load vectors evaluated for each element using eq. (3.90). The single $\overline{\boldsymbol{t_\Gamma}}^{(i_{el})}$ vector is defined in eq. (3.60). The integral over the complete Neumann boundary associated to a certain element can be split to multiple integrals performed over the edges where non-zero tractions are prescribed. The parts of the Neumann boundary where the tractions are zero can be discarded from the integration, since the integrand vanishes in such case.

Assume that all the loaded edges are labelled by index $j_N = 1,2,\ldots,n_N$ with n_N being the overall number of loaded edges. Furthermore, assume a set $S^{(i_{el})}$ collects the indices j_N related to a certain element i_{el}. Under such considerations, loading vector $\overline{\boldsymbol{t_\Gamma}}^{(i_{el})}$, related to a single element, can be split into integrals evaluated over the individual edges contained in the set $S^{(i_{el})}$

$$\overline{\boldsymbol{t_\Gamma}}^{(i_{el})} = \sum_{n \in S^{(i_{el})}} \overline{\boldsymbol{t_\Gamma}}_n = \sum_{n \in S^{(i_{el})}} \int_0^{l_n} \widehat{\boldsymbol{U}}^T \boldsymbol{t_{\Gamma}}_n \,\mathrm{d}s_n. \tag{6.28}$$

In this equation s_n denotes the coordinate running along a single edge n and l_n means the length of such edge. Vector $\boldsymbol{t_\Gamma}_n$ contains functions describing the distributed loading on the current edge n. Furthermore, the contributions related to a single edge are approximated using the numerical quadrature

$$\overline{\boldsymbol{t_\Gamma}}_{j_N} = \int_0^{l_{j_N}} \widehat{\boldsymbol{U}}^T \boldsymbol{t_\Gamma}_{j_N} \,\mathrm{d}s_{j_N} \approx \sum_{k=1}^{q} w_k \widehat{\boldsymbol{U}}^T (x(\xi_k),y(\xi_k)) \boldsymbol{t_\Gamma}_{j_N}(\xi_k) J_{j_N}(\xi_k). \tag{6.29}$$

The implemented code is structured in the following way. It contains a loop over all loaded edges j_N. After the element index i_{el} associated to the current edge is obtained, the related nodal coordinates are extracted. In the case of local reference frame, they need to be transformed afterwards. Subsequently, vector $\overline{\boldsymbol{t}_{\boldsymbol{\Gamma}}}_{j_N}$ is evaluated and assembled to the global vector $\overline{\boldsymbol{t}_{\boldsymbol{\Gamma}_G}}$ according to the related element index i_{el}.

In the function for computation of the single $\overline{\boldsymbol{t}_{\boldsymbol{\Gamma}}}_{j_N}$ vector, firstly the components of the loading at the end nodes are extracted from the input data. Subsequently, a loop over the integration points k is entered and the position of the Gauss point, components of the unit normal and Jacobian are evaluated. As was mentioned before, the loading is assumed to be linear along the edge, hence the corresponding value of the loading function at the quadrature points can be obtained with the use of the linear shape functions. Therefore, also the shape functions are evaluated and afterwards the loading intensity at the current point can be calculated. As the input loading components are expressed in normal and tangential directions, they need to be transformed to Cartesian components eventually. Then the basis $\boldsymbol{U}(x(\xi_k),y(\xi_k))$ is expressed at the Gauss point location and the contribution of the current integration point to the complete integral is evaluated.

In the following pseudocode the main points of the algorithm implemented for evaluation of the vector $\overline{\boldsymbol{t}_{\boldsymbol{\Gamma}_G}}$ are recapitulated.

1. Allocate $\overline{\boldsymbol{t}_{\boldsymbol{\Gamma}_G}}$
2. Loop over edges j_N where non-zero tractions are prescribed
   a) Get element index i_{el} and the corresponding coordinates of the element nodes
      - If local reference frame is chosen → transform the nodal coordinates
   b) Compute $\overline{\boldsymbol{t}_{\boldsymbol{\Gamma}}}_{j_N}$
      i. Allocate $\overline{\boldsymbol{t}_{\boldsymbol{\Gamma}}}_{j_N}$
      ii. Obtain normal and tangential components of the loading at the end nodes
      iii. Loop over integration points k
         A. Evaluate position of the Gauss point, the components of the unit normal, the Jacobian and the value of the shape functions
         B. Compute the loading components at the current integration point multiplying the end values by shape functions
         C. Transform the components to Cartesian directions
         D. Evaluate bases $\boldsymbol{U}(x(\xi_k),y(\xi_k))$ at the Gauss point location
         E. Compute the contribution of the integration point and add it to the existing vector: $\overline{\boldsymbol{t}_{\boldsymbol{\Gamma}}}_{j_N} = \overline{\boldsymbol{t}_{\boldsymbol{\Gamma}}}_{j_N} + w_k \widehat{\boldsymbol{U}}^T \boldsymbol{t}_{\boldsymbol{\Gamma}}{}_{j_N} J_{j_N}$
   c) Assemble $\overline{\boldsymbol{t}_{\boldsymbol{\Gamma}}}_{j_N}$ to $\overline{\boldsymbol{t}_{\boldsymbol{\Gamma}_G}}$ based on the element index i_{el}

Global Vector $\overline{\boldsymbol{u}_{\boldsymbol{\Gamma}_G}}$

The construction procedure of the vector $\overline{\boldsymbol{u}_{\boldsymbol{\Gamma}_G}}$ described in section 3.4.6 is simplified, when no body forces are acting on the structure. The length of the global vector $\overline{\boldsymbol{u}_{\boldsymbol{\Gamma}_G}}$ depends on the number of all Dirichlet edges j (including both constrained and inter-element ones). However, non-zero components only appear in the rows related to the edges, where the displacement boundary condition is applied. For these edges vector $-\overline{\boldsymbol{u}_{\boldsymbol{\Gamma}}}_j^{(i_{el})}$ is evaluated based on eq. (3.65) and added to the global vector according to index j.

The integral appearing in the definition of the single $\overline{\boldsymbol{u}_{\boldsymbol{\Gamma}}}_j^{(i_{el})}$ vector is approximated using the quadrature rule

$$\overline{\boldsymbol{u}_{\boldsymbol{\Gamma}}}_j^{(i_{el})} = \int_0^{l_j} \boldsymbol{Z}^T \boldsymbol{u}_{\boldsymbol{\Gamma}j} \,\mathrm{d}s_j = \sum_{k=1}^{q} w_k \boldsymbol{Z}^T(\xi_k) \boldsymbol{u}_{\boldsymbol{\Gamma}j} J_j(\xi_k). \tag{6.30}$$

Vector $\boldsymbol{u}_{\boldsymbol{\Gamma}j}$ collects the prescribed displacement components on the current edge j, which are constant functions.

Assume a set S_c collects the indices j related to the constrained edges, hence indices associated to the inter-element edges are omitted. In the algorithm a loop over the indices $n \in S_c$ is performed. Inside the loop the individual $-\overline{\boldsymbol{u}_{\boldsymbol{\Gamma}}}_n^{(i_{el})}$ vectors are evaluated and assembled to the global vector $\overline{\boldsymbol{u}_{\boldsymbol{\Gamma}_G}}$ based on the edge index n.

The function for computation of the single $\overline{\boldsymbol{u}_{\boldsymbol{\Gamma}}}_n^{(i_{el})}$ vector contains a loop over the integration points. Inside the loop the Jacobian $J_n(\xi_k)$ and the basis $\boldsymbol{Z}(\xi_k)$ are evaluated. Afterwards, the contribution of one Gauss point to the complete sum appearing in eq. (6.30) is calculated. If the constrained edge is of mixed type, and therefore only one degree of freedom $u_{\Gamma n}$ is prescribed, the product $\boldsymbol{Z}^T(\xi_k)\boldsymbol{u}_{\boldsymbol{\Gamma}n}$ in eq. (6.30) is replaced by $\boldsymbol{Z}_{\boldsymbol{v}}^T(\xi_k)u_{\Gamma n}$. Vector $\boldsymbol{Z}_{\boldsymbol{v}}$ is a part of the complete matrix $\boldsymbol{Z}$ and was defined in section 3.3.

The following list of procedures sums up the implemented algorithm for computation of the vector $\overline{\boldsymbol{u}_{\boldsymbol{\Gamma}_G}}$.

1. Allocate $\overline{\boldsymbol{u}_{\boldsymbol{\Gamma}_G}}$ vector
2. Loop over all constrained edges $n \in S_c$
   a) Get related element index i_{el} and corresponding nodal coordinates
      - If local reference frame is chosen → transform the nodal coordinates
   b) Compute $\overline{\boldsymbol{u}_{\boldsymbol{\Gamma}}}_n^{(i_{el})}$
      i. Allocate $\overline{\boldsymbol{u}_{\boldsymbol{\Gamma}}}_n^{(i_{el})}$
      ii. Loop over integration points k
         A. Evaluate the Jacobian
         B. Evaluate bases $\boldsymbol{Z}(\xi_k)$ at the Gauss point location ξ_k
         C. Compute the contribution of the integration point and add it to the existing vector: $\overline{\boldsymbol{u}_{\boldsymbol{\Gamma}}}_n^{(i_{el})} = \overline{\boldsymbol{u}_{\boldsymbol{\Gamma}}}_n^{(i_{el})} + w_k \boldsymbol{Z}^T \boldsymbol{u}_{\boldsymbol{\Gamma}n} J_n$

- If only one degree of freedom is prescribed $\rightarrow \overline{\boldsymbol{u}_{\boldsymbol{\Gamma}}}_n^{(i_{el})} = \overline{\boldsymbol{u}_{\boldsymbol{\Gamma}}}_n^{(i_{el})} + w_k \boldsymbol{Z}_{\boldsymbol{v}}^T u_{\Gamma n} J_n$

c) Assemble $\overline{\boldsymbol{u}_{\boldsymbol{\Gamma}}}_n^{(i_{el})}$ to $\overline{\boldsymbol{u}_{\boldsymbol{\Gamma_G}}}$

6.3.3 System Solution and Scaling

The final governing system of equations is constructed by combining all the previously derived global matrices and vectors, which is described by eq. (4.50). In short notation, the system can be expressed as

$$\boldsymbol{A}\boldsymbol{x} = \boldsymbol{b}, \tag{6.31}$$

where

$$\boldsymbol{A} = \begin{bmatrix} \boldsymbol{D_G} & -\boldsymbol{B_{a,G}} & -\boldsymbol{B_G} \\ -\widehat{\boldsymbol{B_{a,G}}}^T & \boldsymbol{D_{a,G}} & \boldsymbol{0} \\ -\widehat{\boldsymbol{B_G}}^T & \boldsymbol{0} & \boldsymbol{0} \end{bmatrix}, \tag{6.32}$$

$$\boldsymbol{x} = \begin{bmatrix} \boldsymbol{X}_{\boldsymbol{G}}^T & \boldsymbol{p}_{\boldsymbol{a,G}}^T & \boldsymbol{p}_{\boldsymbol{G}}^T \end{bmatrix}^T, \tag{6.33}$$

$$\boldsymbol{b} = \begin{bmatrix} \overline{\boldsymbol{t_{\Gamma_G}}}^T & \boldsymbol{0}^T & \overline{\boldsymbol{u_{\Gamma_G}}}^T \end{bmatrix}^T. \tag{6.34}$$

The condition number of the matrix $\boldsymbol{A}$ as well as the resulting numerical error can be reduced by the application of a system scaling procedure. Eq. (6.31) can be reformulated as

$$\begin{aligned} \widehat{\boldsymbol{S}}^T \boldsymbol{A} \boldsymbol{S} \boldsymbol{S}^{-1} \boldsymbol{x} &= \widehat{\boldsymbol{S}}^T \boldsymbol{b} \\ \overline{\boldsymbol{A}} \overline{\boldsymbol{x}} &= \overline{\boldsymbol{b}}, \end{aligned} \tag{6.35}$$

where $\overline{\boldsymbol{A}} = \widehat{\boldsymbol{S}}^T \boldsymbol{A} \boldsymbol{S}$, $\overline{\boldsymbol{x}} = \boldsymbol{S}^{-1}\boldsymbol{x}$ and $\overline{\boldsymbol{b}} = \widehat{\boldsymbol{S}}^T \boldsymbol{b}$. The term $\boldsymbol{S}$ denotes a diagonal scaling matrix. The previously described modification preserves the symmetry property of the original matrix $\boldsymbol{A}$.

The idea of the scaling procedure is to modify the system so that the diagonal terms of $\overline{\boldsymbol{A}}$ are of similar magnitude and close to unity. Therefore, the diagonal components of the scaling matrix collect inverted square roots of the diagonal terms appearing in the matrix $\boldsymbol{A}$. In the case the diagonal component of $\boldsymbol{A}$ is zero, the associated term in the scaling matrix is taken as one. Hence the components $S_{i,i}$ on the diagonal of matrix $\boldsymbol{S}$ can be expressed as

$$S_{i,i} = \begin{cases} \dfrac{1}{\sqrt{A_{i,i}}}, & \text{if } A_{i,i} \neq 0 \\ 1, & \text{if } A_{i,i} = 0, \end{cases} \tag{6.36}$$

where $A_{i,i}$ denotes the diagonal components of $\boldsymbol{A}$. Symbol i stands for the row index of the related matrix.

The modified system in eq. (6.35) is solved by the application of the MATLAB inbuilt function `mldivide`, which chooses a suitable solver according to the properties of the matrix $\overline{\boldsymbol{A}}$. After the scaled solution vector $\overline{\boldsymbol{x}}$ is computed, the original vector of unknown coefficients $\boldsymbol{x}$ is obtained as

$\boldsymbol{x} = \boldsymbol{S}\overline{\boldsymbol{x}}$.

6.3.4 Post-processing and Visualization

As was mentioned in section 3.5, vectors $\boldsymbol{X_G}$, $\boldsymbol{p_{a,G}}$ and $\boldsymbol{p_G}$ collect the generalized quantities and therefore a post-processing phase is necessary so that the values of the fields of interest are obtained. These consist of the displacement, strain and stress field, which are all derived from the the approximated displacement field within an element.

In the post-processing part of the algorithm, a loop over all elements is implemented. Inside the loop indices of the Dirichlet edges j as well as the absorbing edges j_a related to the particular element are obtained. Subsequently, the coefficients $\boldsymbol{X}^{(i_{el})}$ associated to the displacement approximation of the element are extracted from the global vector $\boldsymbol{X_G}$. Similarly, also the coefficients $\boldsymbol{p}_j$ and $\boldsymbol{p_a}_{j_a}$ linked to the Dirichlet and absorbing edges at the current element are pulled out from the global vectors $\boldsymbol{p_G}$ and $\boldsymbol{p_{a,G}}$. Afterwards, the function for evaluation of the fields on a single element is called.

Inside the function a grid of points (x_e,y_e) belonging to the investigated element is calculated. Subscript e denotes the index of the point. A loop over those evaluation locations is performed, for each, the bases $\boldsymbol{U}(x_e,y_e)$ and $\boldsymbol{E}(x_e,y_e)$ are computed and values of the displacement and strain fields are calculated based on eqs. (3.1) and (3.4). The stress field can then be evaluated by the application of the material law expressed by eq. (2.34).

The tractions on the Dirichlet and absorbing boundary can be computed using two approaches. The first option is to use the boundary traction approximation introduced in eq. (3.36), where the related $\boldsymbol{p}_j$ or $\boldsymbol{p_a}_{j_a}$ coefficients are inserted. The second way is to directly compute the tractions from the stress field evaluated based on the domain displacement approximation. In fact, the second option represents the tractions associated to the computed displacement field and therefore these are of main interest. However, comparing them with the tractions, which were computed based on the boundary traction approximation, can serve as a measure of quality of the results.

Based on the discussion in the previous paragraph, also normal and tangential tractions on the Dirichlet and absorbing edges are evaluated in the field evaluation function. Therefore, a second loop over the aforementioned edges is implemented. Inside the loop the normalized locations of the points $\xi_l \in \langle -1,1 \rangle$ are generated and a loop over those is entered. Subscript l stands for the index of the point. Subsequently, for each point on the boundary, the tractions derived from the domain displacement field are evaluated. This procedure consists of mapping the normalized boundary coordinate ξ_l to the chosen Cartesian reference frame and evaluation of the matrix of unit normals at the current point. Then the strain basis $\boldsymbol{E}(x(\xi_l),y(\xi_l))$ is calculated and the stresses are expressed by application of eqs. (3.4) and (2.34). The Cartesian components of the boundary tractions are then computed with the use of the boundary equilibrium based on eq. (2.35). As the components in normal and tangential directions are of interest, the tractions need to be transformed eventually.

Computation of the boundary tractions based on the boundary approximation can be performed in the same loop over the locations ξ_l. The boundary approximation basis $\boldsymbol{Z}(\xi_l)$ can directly be evaluated at the point location ξ_l and multiplied by the corresponding coefficients $\boldsymbol{p}_j$ or $\boldsymbol{p_a}_{j_a}$. In

the case the current Dirichlet edge j is the inter-element one, it needs to be checked, if in the assembly process of $\boldsymbol{B_g}$ the related $\boldsymbol{B}_j^{(i_{el})}$ matrix was considered with the minus sign. In the case it was, the associated $\boldsymbol{p}_j$ vector needs to be multiplied by the minus sign as well, which results from the traction continuity condition and eq. (3.94).

After all the fields are evaluated for the investigated points in the domain and on the boundary of the element, the stored results can be visualized. The previously described procedure is then repeated for all elements.

The post-processing procedure is recapitulated in the following pseudocode.

1. Loop over all elements i_{el}
   a) Get nodal coordinates related to the current element
      - If local reference frame is chosen → transform the nodal coordinates
   b) Obtain indices j and j_a of the Dirichlet and absorbing edges related to the current element
   c) Extract the vectors of coefficients $\boldsymbol{X}^{(i_{el})}$, $\boldsymbol{p}_j$ and $\boldsymbol{p_a}_{j_a}$ associated to the current element
   d) Evaluate the displacements, strains and stresses in the element domain and tractions on the boundary
      i. Compute the material matrix $\boldsymbol{k}$
      ii. Create a grid of points (x_e,y_e) inside the element
      iii. Loop over the evaluation points
         A. Evaluate bases $\boldsymbol{U}(x_e,y_e)$ and $\boldsymbol{E}(x_e,y_e)$ at the current point
         B. Compute the displacement, strain and stress components at the current point
      iv. Loop over the Dirichlet and absorbing edges
         A. Generate boundary evaluation points ξ_l in the normalized space ξ
         B. Loop over the points ξ_l
            - Compute the tractions derived from the displacement field
              - Map the points to the Cartesian coordinates in the chosen reference frame and obtain components of the unit normal
              - Evaluate the strain basis $\boldsymbol{E}(x(\xi_l),y(\xi_l))$ and subsequently the vector of strain components
              - Compute the stress vector and the derived traction components
            - Compute tractions from the boundary traction approximation
              - Evaluate basis $\boldsymbol{Z}(\xi_l)$
              - Compute the boundary tractions by multiplying the basis $\boldsymbol{Z}(\xi_l)$ with the coefficients $\boldsymbol{p}_j$ or $\boldsymbol{p_a}_{j_a}$
            - Transform the boundary tractions to normal and tangential components

v. Plot the evaluated fields in the element domain and on the element boundary

The overall program structure is summarized in the flowchart in fig. 6.2.

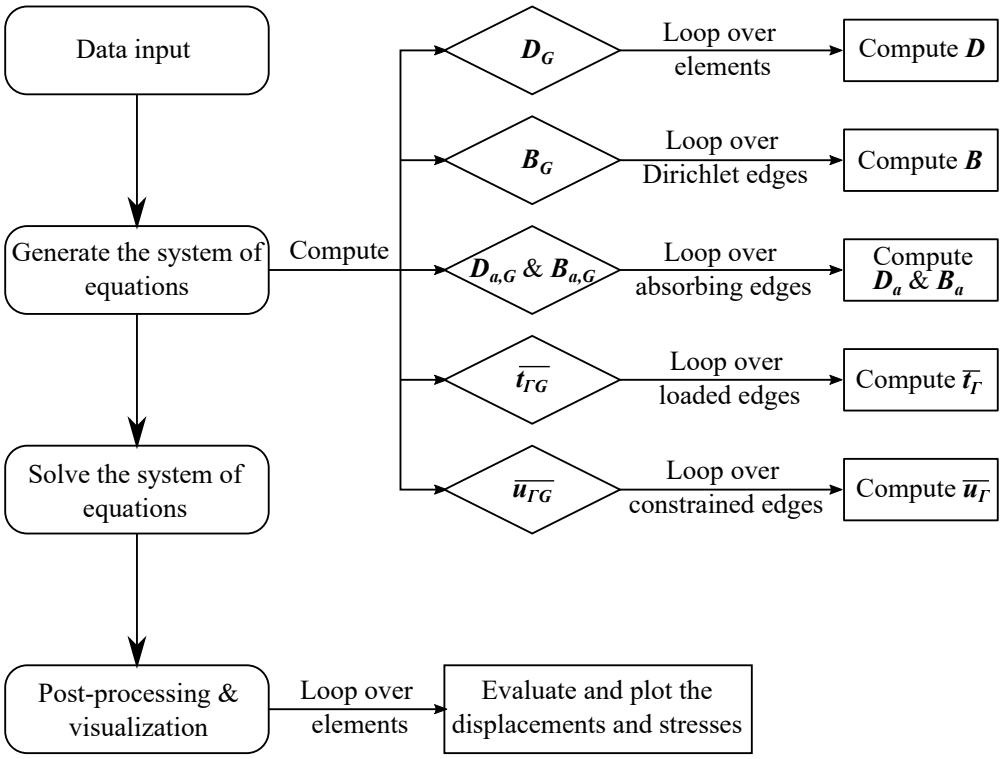

Figure 6.2: Program structure

7 Results

In the following chapter the implemented method is tested on various examples and the results are presented and summarized.

As the first example, bounded domain is analysed and the results are compared to the known analytical solution. The convergence process is studied in detail while both p-refinement and h-refinement strategies are applied. In the second test case the implemented approach for modelling of infinite domains is validated. Also for this example the simulation outcome, which was obtained for various meshes and for approximation bases including various numbers of terms, is compared to the true reference solution. Furthermore, the effect of the distance from the origin at which the infinite domain is truncated is investigated. As the last example, wave propagation in a loaded half space is examined and the results are compared to those obtained using the wave based method.

In the first section of the chapter the quantity chosen as the measure for comparison of the obtained results is introduced.

7.1 Global Comparison Quantity

To compare the approximated results to the reference solution, it is advantageous to introduce a single scalar quantity which reflects the properties of the obtained vector fields. The chosen quantity, denoted by E, is defined as

$$E = \frac{1}{2}\int \widehat{\boldsymbol{\sigma}}^T \boldsymbol{\varepsilon}\,\mathrm{d}V - \frac{1}{2}\int \widehat{\dot{\boldsymbol{u}}}^T \rho \dot{\boldsymbol{u}}\,\mathrm{d}V. \tag{7.1}$$

The first term in the previous equation denotes the potential energy related to the deformed body averaged over one period $T = 2\pi/\omega$. The second term in eq. (7.1) represents the kinetic energy averaged over the period T, therefore the meaning of the quantity E is the difference between average potential and kinetic energies associated to the investigated domain. The reason why measure E is used instead of the average mechanical energy, which is expressed as the sum of both mentioned energies, is the simplicity of its evaluation. As will be shown, eq. (7.1) can be reformulated into convenient expression, which can be evaluated by the product of the vector of coefficients $\boldsymbol{X_G}$ and already computed matrix $\boldsymbol{D_G}$.

The velocity field $\dot{\boldsymbol{u}}(x,y)$, appearing in eq. (7.1), can be expressed in terms of the displacement field $\boldsymbol{u}(x,y)$ as

$$\dot{\boldsymbol{u}} = i\omega \boldsymbol{u}, \tag{7.2}$$

which follows from the spectral representation of the individual fields discussed in chapter 2. Sub-

stituting the previous expression into eq. (7.1), the quantity E can be reformulated to

$$E = \frac{1}{2}\int \widehat{\boldsymbol{\sigma}}^T \boldsymbol{\varepsilon}\,\mathrm{d}V - \frac{1}{2}\int \widehat{i\omega}\widehat{\boldsymbol{u}}^T \rho i\omega \boldsymbol{u}\,\mathrm{d}V = \frac{1}{2}\int \widehat{\boldsymbol{\sigma}}^T \boldsymbol{\varepsilon}\,\mathrm{d}V - \frac{1}{2}\omega^2 \int \widehat{\boldsymbol{u}}^T \rho \boldsymbol{u}\,\mathrm{d}V. \tag{7.3}$$

In the subsequent sections, this equation is further developed and manipulated and exact formulas for its evaluation based on both analytical solutions as well as on the results obtained using hybrid-Trefftz method are expressed.

7.1.1 Analytical Expression

The solution procedure of the spectral Lamé equation was thoroughly discussed in section 3.2. The solution functions are ordered in the displacement and strain approximation bases $\boldsymbol{U}$ and $\boldsymbol{E}$. For a single order n, the components in radial and angular directions are collected in matrices $\boldsymbol{U}_{\boldsymbol{n}}^{\boldsymbol{r},\boldsymbol{\theta}}$ and $\boldsymbol{E}_{\boldsymbol{n}}^{\boldsymbol{r},\boldsymbol{\theta}}$, which are expressed in eqs. (3.31) and (3.34). The functions associated to p-waves are collected in the first column and the ones related to s-waves appear in the second column. The quantity E related to these individual modes can be obtained by substitution of the basis components into eq. (7.3).

For the particular 2D case of interest, the volume integral in eq. (7.3) turns to a surface integral multiplied by the thickness of the structure, which is assumed to be unitary. Furthermore, to simplify the resulting expression, the shape of the body is assumed to be circular section defined by the inner and outer radii r_0 and r_1 and starting and ending angles θ_0 and θ_1. The integration is then performed in polar coordinate system, therefore eq. (7.3) is modified as

$$E = \frac{1}{2}\int \left(\widehat{\boldsymbol{\sigma}}^T \boldsymbol{\varepsilon} - \omega^2 \widehat{\boldsymbol{u}}^T \rho \boldsymbol{u}\right)\,\mathrm{d}V = \frac{1}{2}\int_{r_0}^{r_1}\int_{\theta_0}^{\theta_1} \left(\widehat{\boldsymbol{\sigma}}^T \boldsymbol{\varepsilon} - \omega^2 \widehat{\boldsymbol{u}}^T \rho \boldsymbol{u}\right) r\,\mathrm{d}\theta\mathrm{d}r. \tag{7.4}$$

In the following, this expression is expanded individually for the p-wave and s-wave solution functions.

P-wave Solution

The displacement components in polar coordinates associated to the p-wave solution can be extracted from the expression (3.31) and read as

$$\boldsymbol{u}_{n,p}^{r,\theta} = \frac{1}{2}k_p \begin{bmatrix} W_{n-1}(k_p r) - W_{n+1}(k_p r) \\ iW_{n-1}(k_p r) + iW_{n+1}(k_p r) \end{bmatrix} \exp(in\theta). \tag{7.5}$$

Similarly, the strain components associated to p-waves are taken from eq. (3.34) and are expressed as

$$\boldsymbol{\varepsilon}_{n,p}^{r,\theta} = \frac{1}{4}k_p^2 \begin{bmatrix} W_{n-2}(k_p r) - 2W_n(k_p r) + W_{n+2}(k_p r) \\ -W_{n-2}(k_p r) - 2W_n(k_p r) - W_{n+2}(k_p r) \\ 2i(W_{n-2}(k_p r) - W_{n+2}(k_p r)) \end{bmatrix} \exp(in\theta). \tag{7.6}$$

The related stress field is obtained by the application of the material law (2.6). Substituting the previous expressions for the displacement, strain and stress components into eq. (7.4), the relation can be reformulated. After some symbolic manipulations, the individual products appearing in the integrand result in

$$\widehat{\boldsymbol{\sigma}}^T\boldsymbol{\varepsilon} = \frac{1}{2}k_p^4\left(2\widehat{W_n}W_n(\lambda+\mu)+\mu\left(\widehat{W_{n-2}}W_{n-2}+\widehat{W_{n+2}}W_{n+2}\right)\right), \tag{7.7}$$

$$\widehat{\boldsymbol{u}}^T\rho\boldsymbol{u} = \frac{1}{2}\rho k_p^2\left(\widehat{W_{n-1}}W_{n-1}+\widehat{W_{n+1}}W_{n+1}\right). \tag{7.8}$$

One can note that both of the previous terms are independent of angular coordinate θ and hence the associated integral in eq. (7.4) can be computed separately and the expression is then simplified

$$E = \frac{1}{2}\int_{r_0}^{r_1}\int_{\theta_0}^{\theta_1}\left(\widehat{\boldsymbol{\sigma}}^T\boldsymbol{\varepsilon}-\omega^2\widehat{\boldsymbol{u}}^T\rho\boldsymbol{u}\right)r\,\mathrm{d}\theta\mathrm{d}r = \frac{1}{2}(\theta_1-\theta_0)\int_{r_0}^{r_1}\left(\widehat{\boldsymbol{\sigma}}^T\boldsymbol{\varepsilon}-\omega^2\widehat{\boldsymbol{u}}^T\rho\boldsymbol{u}\right)r\,\mathrm{d}r, \tag{7.9}$$

where the products $\widehat{\boldsymbol{\sigma}}^T\boldsymbol{\varepsilon}$ and $\widehat{\boldsymbol{u}}^T\rho\boldsymbol{u}$ are expressed by eqs. (7.7) and (7.8). The integral appearing in the previous equation cannot be computed analytically for an arbitrary type of the Bessel solution function W_n and therefore the resulting value is approximated by the application of numerical integration techniques.

S-wave Solution

The quantity E related to the displacement shapes associated to s-waves is obtained in the similar way as was described in the previous subsection. The related displacement and strain basis components are extracted from expressions (3.31) and (3.34)

$$\boldsymbol{u}_{n,s}^{r,\theta} = \frac{1}{2}k_s\begin{bmatrix} iW_{n-1}(k_sr)+iW_{n+1}(k_sr) \\ W_{n+1}(k_sr)-W_{n-1}(k_sr)\end{bmatrix}\exp(in\theta), \tag{7.10}$$

$$\boldsymbol{\varepsilon}_{n,s}^{r,\theta} = \frac{1}{4}k_s^2\begin{bmatrix} iW_{n-2}(k_sr)-iW_{n+2}(k_sr) \\ iW_{n+2}(k_sr)-iW_{n-2}(k_sr) \\ -2(W_{n-2}(k_sr)+W_{n+2}(k_sr))\end{bmatrix}\exp(in\theta). \tag{7.11}$$

The products appearing in the integral in eq. (7.4) can subsequently be simplified to

$$\widehat{\boldsymbol{\sigma}}^T\boldsymbol{\varepsilon} = \frac{1}{2}\mu k_s^4\left(\widehat{W_{n-2}}W_{n-2}+\widehat{W_{n+2}}W_{n+2}\right), \tag{7.12}$$

$$\widehat{\boldsymbol{u}}^T\rho\boldsymbol{u} = \frac{1}{2}\rho k_s^2\left(\widehat{W_{n-1}}W_{n-1}+\widehat{W_{n+1}}W_{n+1}\right). \tag{7.13}$$

Also in the case of s-wave solution, the integrand turns out to be independent of the angular coordinate θ and hence the expression for E is simplified to eq. (7.9), where the terms $\widehat{\boldsymbol{\sigma}}^T\boldsymbol{\varepsilon}$ and $\widehat{\boldsymbol{u}}^T\rho\boldsymbol{u}$ are formulated in eqs. (7.12) and (7.13).

7.1.2 Finite Element Approximation

Substituting the domain displacement and strain field approximations defined in eqs. (3.1) and (3.4) into expression (7.3), the relation for the finite element approximation E_{FE} of the true quantity E can be obtained. To simplify the derivation, the terms related to the particular solution are omitted. Firstly, the approximation E^e_{FE} associated to a single element is expressed as

$$\begin{aligned} E^e_{FE} =& \frac{1}{2}\int \widehat{\boldsymbol{\sigma}}^T \boldsymbol{\varepsilon}\,\mathrm{d}V^e - \frac{1}{2}\omega^2 \int \widehat{\boldsymbol{u}}^T \rho \boldsymbol{u}\,\mathrm{d}V^e = \\ =& \frac{1}{2}\int \widehat{(\boldsymbol{k}\boldsymbol{\mathcal{D}}^*\boldsymbol{U}\boldsymbol{X})}^T \boldsymbol{E}\boldsymbol{X}\,\mathrm{d}V^e - \frac{1}{2}\omega^2 \int \widehat{(\boldsymbol{U}\boldsymbol{X})}^T \rho \boldsymbol{U}\boldsymbol{X}\,\mathrm{d}V^e = \\ =& \frac{1}{2}\widehat{\boldsymbol{X}}^T \int (\boldsymbol{\mathcal{D}}^*\widehat{\boldsymbol{U}})^T \boldsymbol{k}\boldsymbol{E}\,\mathrm{d}V^e\,\boldsymbol{X} - \frac{1}{2}\omega^2 \widehat{\boldsymbol{X}}^T \int \widehat{\boldsymbol{U}}^T \rho \boldsymbol{U}\,\mathrm{d}V^e\,\boldsymbol{X}. \end{aligned} \tag{7.14}$$

Subsequently, the first integral in the previous equation is modified using the integration by parts technique and the property (3.2) of the displacements basis $\boldsymbol{U}$ is applied. Similar procedure was also used for the derivation of eq. (3.52), which can now be substituted into eq. (7.14)

$$\begin{aligned} E^e_{FE} =& \frac{1}{2}\widehat{\boldsymbol{X}}^T \int \widehat{\boldsymbol{U}}^T \boldsymbol{N}\boldsymbol{k}\boldsymbol{E}\,\mathrm{d}\Gamma^e\,\boldsymbol{X} + \frac{1}{2}\omega^2 \widehat{\boldsymbol{X}}^T \int \widehat{\boldsymbol{U}}^T \rho \boldsymbol{U}\,\mathrm{d}V^e\,\boldsymbol{X} - \frac{1}{2}\omega^2 \widehat{\boldsymbol{X}}^T \int \widehat{\boldsymbol{U}}^T \rho \boldsymbol{U}\,\mathrm{d}V^e\,\boldsymbol{X} = \\ =& \frac{1}{2}\widehat{\boldsymbol{X}}^T \int \widehat{\boldsymbol{U}}^T \boldsymbol{N}\boldsymbol{k}\boldsymbol{E}\,\mathrm{d}\Gamma^e\,\boldsymbol{X} = \frac{1}{2}\widehat{\boldsymbol{X}}\boldsymbol{D}\,\boldsymbol{X}. \end{aligned} \tag{7.15}$$

The definition (3.58) of the matrix $\boldsymbol{D}$ was substituted into the previous equation.

The approximation E_{FE} for all elements is then expressed as

$$E_{FE} = \sum_{i=1}^{n_{el}} {E^e_{FE}}^{(i)} = \frac{1}{2}\sum_{i=1}^{n_{el}} \widehat{\boldsymbol{X}^{(i)}}^T \boldsymbol{D}^{(i)}\,\boldsymbol{X}^{(i)} = \frac{1}{2}\widehat{\boldsymbol{X}_{\boldsymbol{G}}}^T \boldsymbol{D}_{\boldsymbol{G}}\,\boldsymbol{X}_{\boldsymbol{G}}. \tag{7.16}$$

7.2 Example 1: Comparison with Analytical Solution

To validate the implemented code, the obtained results are compared with the known analytical solution. The quantity E, defined in the previous section, is chosen as the measure used for comparison of the analytical and approximated solutions.

For this test case, the domain shape was chosen as the quarter of a hollow circle with inner radius $r_0 = 5\,\mathrm{m}$ and outer radius $r_1 = 25\,\mathrm{m}$. The scheme of the investigated structure is depicted in fig. 7.1a.

The assumed material properties and excitation frequency $f = \omega/2\pi$ are listed in tab. 7.1, where also the derived wave numbers are mentioned.

$\tilde{E}$ [N/m^2]	ν	ρ [kg/m^3]	f [Hz]	η	k_p [1/m]	k_s [1/m]
26000000	0.3	2000	10	0	0.475	0.889

Table 7.1: Material properties, Example 1

Firstly, the analytical solution is introduced and subsequently the results of the numerical simulation are presented.

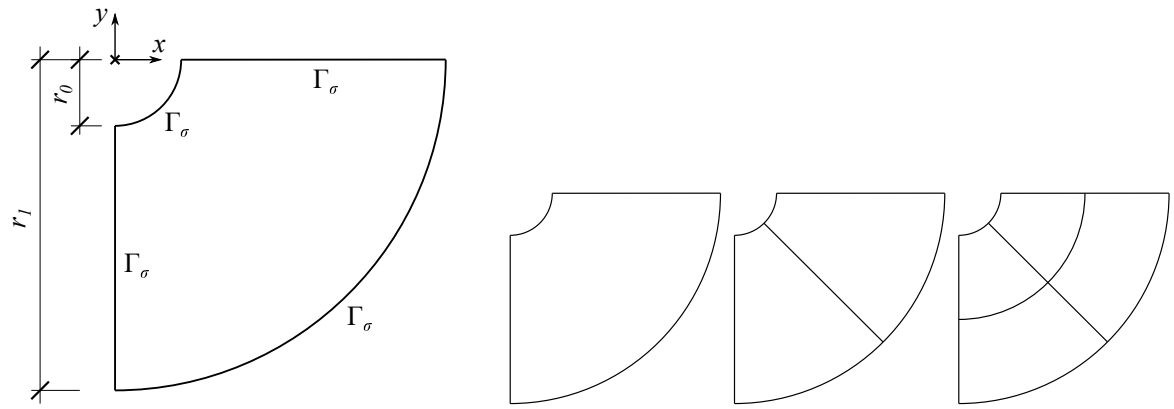

(a) Domain scheme

(b) Finite element meshes

Figure 7.1: Example 1

7.2.1 Analytical Solution

The displacement shapes satisfying the Lamé equation were derived in section 3.2 and for a single order n are collected in matrix $\boldsymbol{U_n}$ defined in eq. (3.30). The functions associated to p-waves are stored in the first column of the matrix and the s-wave terms appear in the second column. These basis functions are directly considered as the analytical solution to which the approximated solution obtained with the implemented method is compared.

The Hankel function of the first kind was chosen as the function W appearing in the matrix $\boldsymbol{U_n}$. The origin for the evaluation of the displacement shapes corresponds to the origin of the Cartesian coordinate system visualized in fig. 7.1a. The order $n = 4$ was selected for the investigated case. In fig. 7.2 the shapes of the displacement field components associated to the p-wave solution are visualized. Similarly, in fig. 7.3 both components of the s-wave displacement solution are plotted.

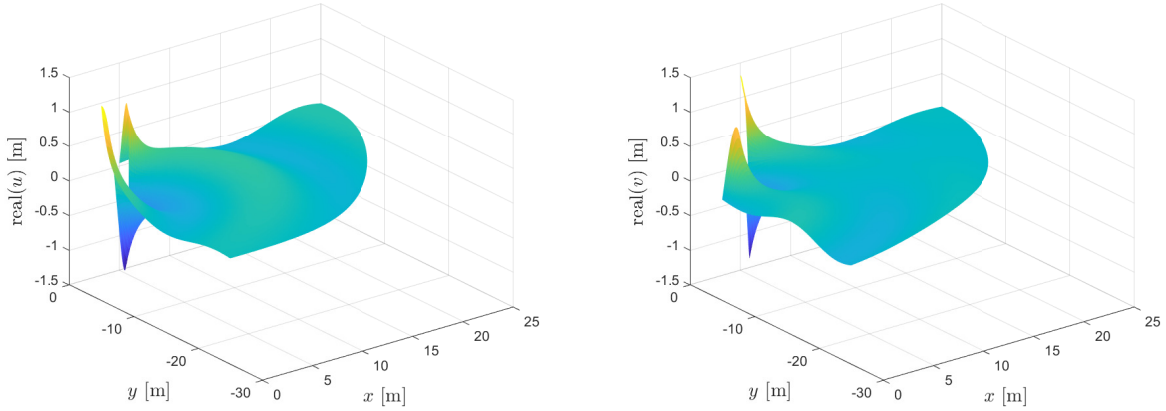

(a) Displacement component u

(b) Displacement component v

Figure 7.2: Analytical displacement solution of Example 1, $W = H^{(1)}$, $n = 4$, p-wave contribution

Due to the special choice of the shape of the investigated domain, the simplified expression (7.9) for the measure E, which is derived in section 7.1.1, can be used for its evaluation. For the

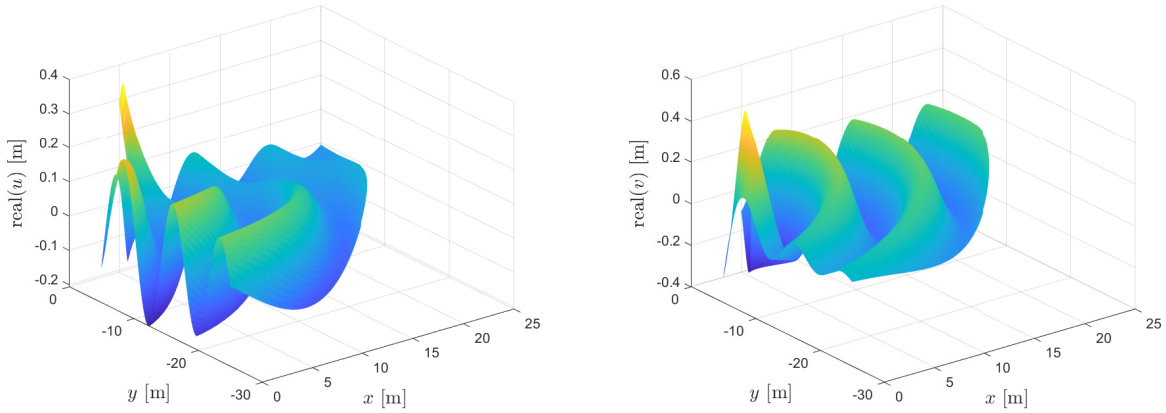

(a) Displacement component u

(b) Displacement component v

Figure 7.3: Analytical displacement solution of Example 1, $W = H^{(1)}$, $n = 4$, s-wave contribution

particular case, values $\theta_0 = -\pi/2$ and $\theta_1 = 0$ are substituted into eq. (7.9). The products $\widehat{\boldsymbol{\sigma}}^T \boldsymbol{\varepsilon}$ and $\widehat{\boldsymbol{u}}^T \rho \boldsymbol{u}$ appearing in the integrand are expressed in eqs. (7.7) and (7.8) for the p-wave solution and by eqs. (7.12) and (7.13) for the s-wave solution. The integral is then approximated by the inbuilt MATLAB function `integral`.

The shown displacement shapes have certain associated strain fields, which can directly be obtained from the basis $\boldsymbol{E_n}$ defined in eq. (3.33). Afterwards, the related stress fields can be acquired by application of the material law. Subsequently, using the boundary equilibrium equation (2.35), the tractions on the boundary of the investigated domain can be recovered. When the problem is modelled using the hybrid-Trefftz method, these tractions derived from the analytical solutions are applied as the boundary condition. Further details are discussed in the next section.

7.2.2 Approximated Solution

As was outlined in the previous paragraph, the boundary tractions obtained from the analytical solution are applied as the loading when the structure is modelled using the implemented method. Therefore the whole boundary of the domain is considered as the Neumann boundary, which is also visualized in fig. 7.1a. Firstly, the boundary tractions associated to the p-wave solution, which is displayed in fig. 7.2, are applied on all the outer edges and the results are compared to the analytical solution. As the second test case, the boundary tractions derived from the s-wave solution (see fig. 7.3) are considered as the traction boundary condition. For both cases, expression (7.16) is used for evaluation of the comparison measure E.

The structure is analysed using three different finite element meshes, which discretize the domain into one, two and four finite elements. The individual meshes are visualized in fig. 7.1b. For each mesh and each test case (p-wave or s-wave case) simulations for various orders N and M, which determine the number of terms contained in the domain displacement and boundary traction bases, are performed. The total number of degrees of freedom, which defines the number of unknowns in

the final system of equations, can be calculated as

$$n_{DOF} = 2n_{el}(2N + 1) + 2n_D(M + 1). \tag{7.17}$$

Symbol n_D denotes the overall number of Dirichlet edges, meaning both inter-element ones as well as the edges, where the displacement components are prescribed. As all the outer edges are part of the Neumann boundary for this test case, n_D stands directly for the number of inter-element edges. For each mesh the number of Dirichlet edges is listed in tab. 7.2.

n_{el}	1	2	4
n_D	0	1	4

Table 7.2: Number of Dirichlet edges for Example 1

The Bessel function of the first kind is chosen as the function W appearing in the definition of the basis $\boldsymbol{U_n}$. For the evaluation of the system matrices, local reference frame placed to the geometrical center of the related element is considered. The number of Gauss points used for the numerical integration along the individual edges was set to $q = 250$. Perhaps even fewer quadrature points would be sufficient, however, the aim was to reduce the error caused by the numerical integration as much as possible.

The convergence plots for the case, when the domain is discretized using a single element, are depicted in fig. 7.4. As for this case there are no Dirichlet edges, all the degrees of freedom are related to the coefficients $\boldsymbol{X}$ multiplying the domain approximation functions. The simulation was performed for the displacement basis of maximum orders $N = 16, 17, \ldots, 30$. The total number of degrees of freedom is then calculated using formula (7.17) and plotted on the x-axis. On the y-axis, the ratio E_{FE}/E is plotted.

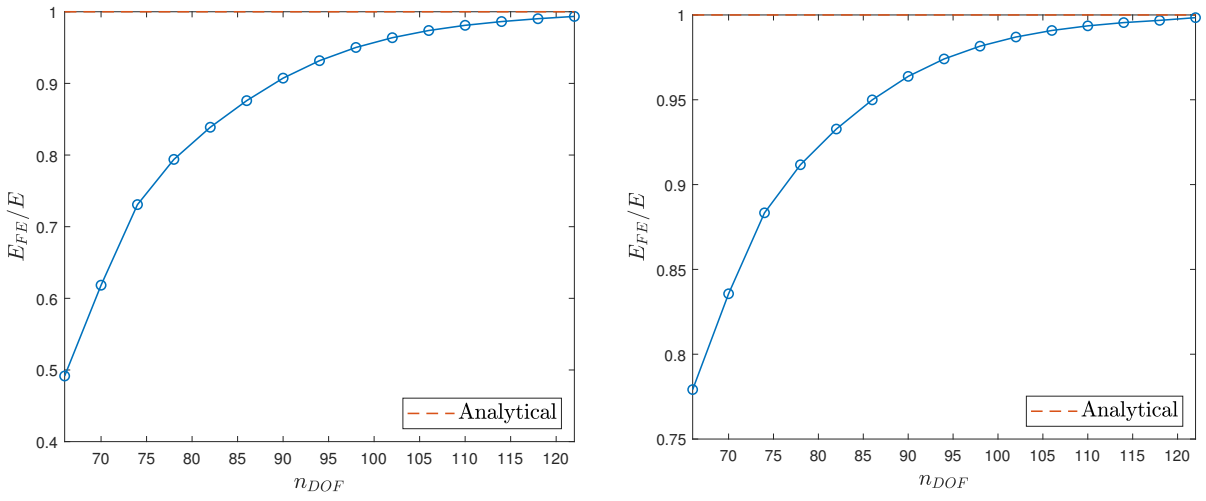

(a) P-wave case **(b)** S-wave case

Figure 7.4: Example 1: Comparison to the analytical solution, 1 element

It can be seen that for increasing number of terms contained in the displacement basis the approximated solution converges to the analytical one. For the p-wave case, when $N = 24$, and

therefore $n_{DOF} = 98$, the error is less than 5%. For the s-wave case, order $N = 22$, which corresponds to $n_{DOF} = 90$, is required to achieve results with error smaller than 5%.

When the structure is discretized using two finite elements, the boundary tractions are approximated on the single inter-element edge. The convergence plots for both p-wave and s-wave cases are visualized in fig. 7.5. The analysis is performed for maximum orders $M = 7, 9, 11, 13$ of the polynomial contained in the boundary traction basis. For each order M, the number of terms contained in the displacement basis is increased, orders in range from $N = 10$ to $N = 21$ are considered. Therefore the individual lines illustrate an increase of the number of terms contained in the domain displacement basis while the length of the traction basis is fixed. The total number of degrees of freedom, which is plotted on the x-axis, is calculated using the relation (7.17).

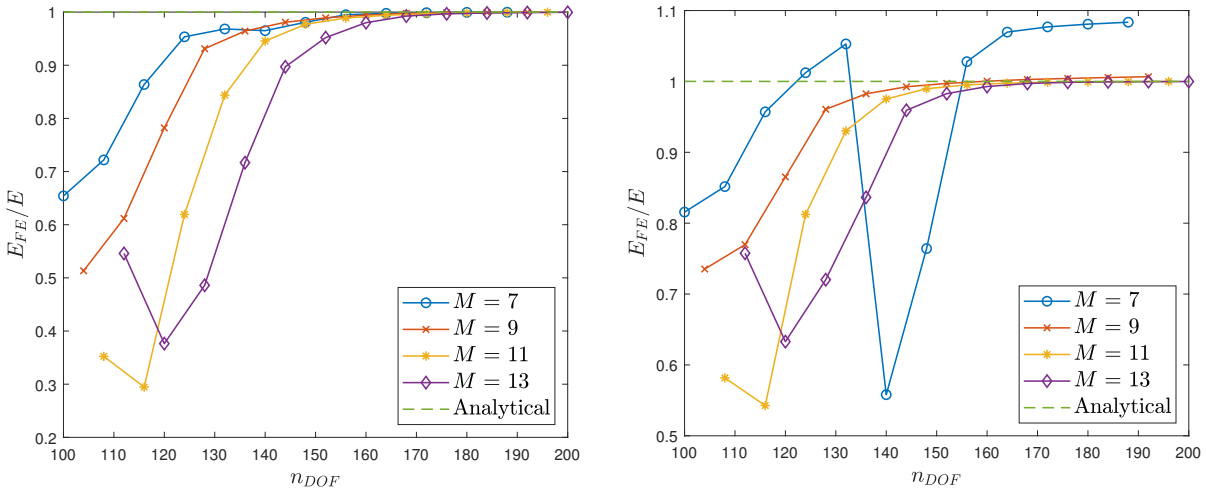

(a) P-wave case **(b)** S-wave case

Figure 7.5: Example 1: Comparison to the analytical solution, 2 elements

From fig. 7.5a for the p-wave case, it can be noted that for all the considered maximum orders M, the approximated results tend towards the reference solution, when the length of the domain approximation basis is increased. Such results indicate that the analytical tractions evaluated at the inter-element boundary can be sufficiently well approximated by the polynomials with all the considered maximum orders M. However, this statement does not hold any more when the s-wave case is analysed. From fig. 7.5b it can be seen that for $M = 7$ the results converge to value which is significantly different compared to analytically evaluated one. As the s-wave analytical solution is more oscillatory compared to the p-wave one, the polynomial of maximum order $M = 7$ cannot approximate the related tractions evaluated at the inter-element edge sufficiently well.

In fact, the same behaviour can be observed even for the p-wave case, only in much larger scale. In fig. 7.6 the results evaluated for domain basis with orders between $N = 21$ and $N = 25$ are visualized. One can note that the lines for orders $M = 7$ and $M = 9$ also tend towards values which are larger compared to the analytical solution. However, the error is negligible in such case, since the analytical tractions are well captured by the polynomial of the related orders. Nevertheless, the exact value of the analytical solution can be recovered only when both orders N and M tend to infinity.

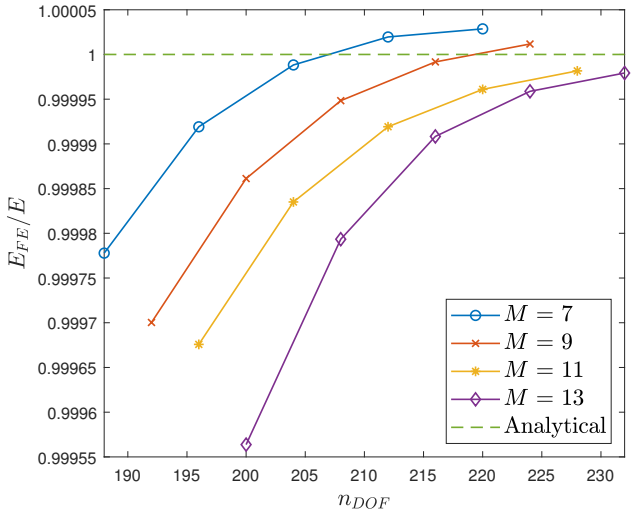

Figure 7.6: Example 1: Comparison to the analytical solution, 2 elements, p-wave case, large scale

From the convergence plots in fig. 7.5 it can be concluded that for the p-wave case, sufficiently accurate results, that is with error smaller than 5%, are achieved for basis orders $M = 7$ and $N = 13$ and hence for $n_{DOF} = 124$. For the s-wave case, similar accuracy is obtained for $M = 9$ and $N = 13$, which means $n_{DOF} = 128$.

As the last investigated case, the domain is discretized using four finite elements. Results for both p-wave and s-wave cases are shown in fig. 7.7. The maximum polynomial orders M contained in the boundary traction basis are $M = 4, 6, 8$. Simultaneously the displacement basis dimension is increased, the maximum included orders vary from $N = 9$ to $N = 15$.

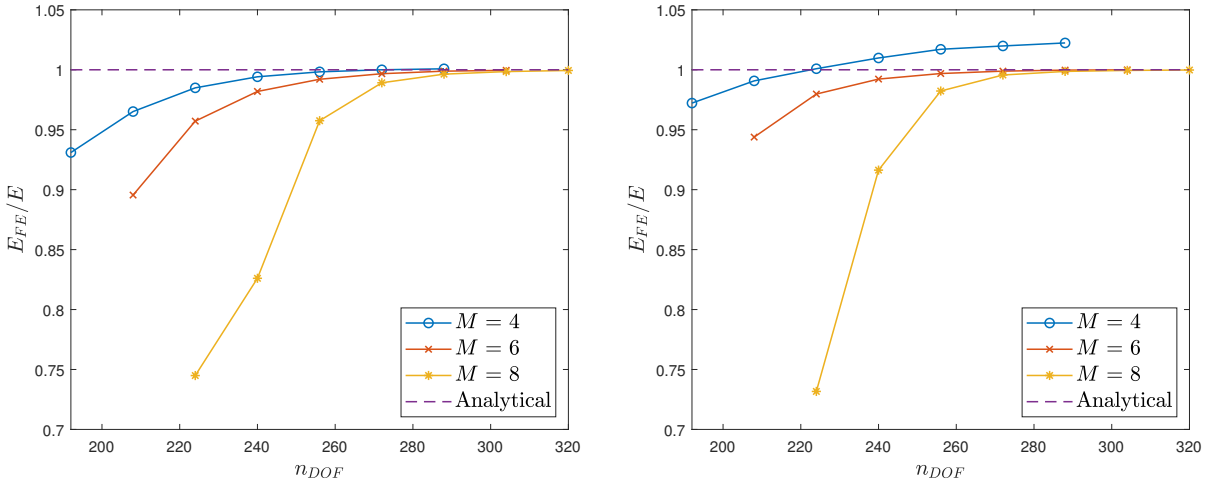

(a) P-wave case

(b) S-wave case

Figure 7.7: Example 1: Comparison to the analytical solution, 4 elements

For the p-wave case, it can be concluded that for all the considered boundary traction basis lengths with maximum orders M, the approximated results converge to values sufficiently close to the analytical expression. For $M = 4$ and $N = 10$, which corresponds to $n_{DOF} = 208$, the error is smaller than 5%.

For the s-wave case, noticeable mismatch occurs for traction basis with $M = 4$, however, the resulting error of the converged value is smaller then 5%, which is acceptable. Already for $M = 4$ and $N = 9$, and therefore for $n_{DOF} = 192$, the difference compared to the analytical solution is smaller than 5%.

To give a reader an idea, how the approximated displacement shapes look like, in the following figures they are visualized for the four-element mesh with bases constructed for orders $N = 10$ and $M = 4$. In fig. 7.8 the p-wave case is shown and in fig. 7.9 the s-wave one is depicted.

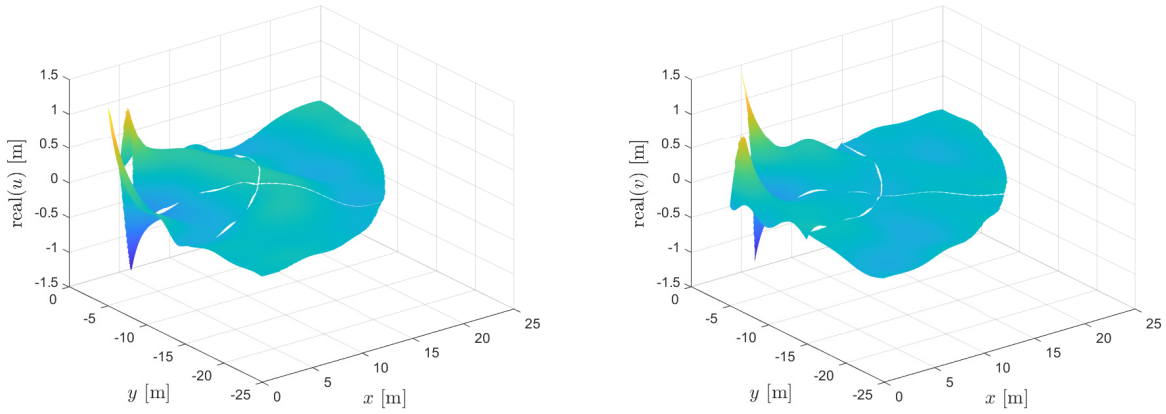

(a) Displacement component u **(b)** Displacement component v

Figure 7.8: Example 1: Approximated displacement shapes, p-wave case, 4 elements, $N = 10$, $M = 4$

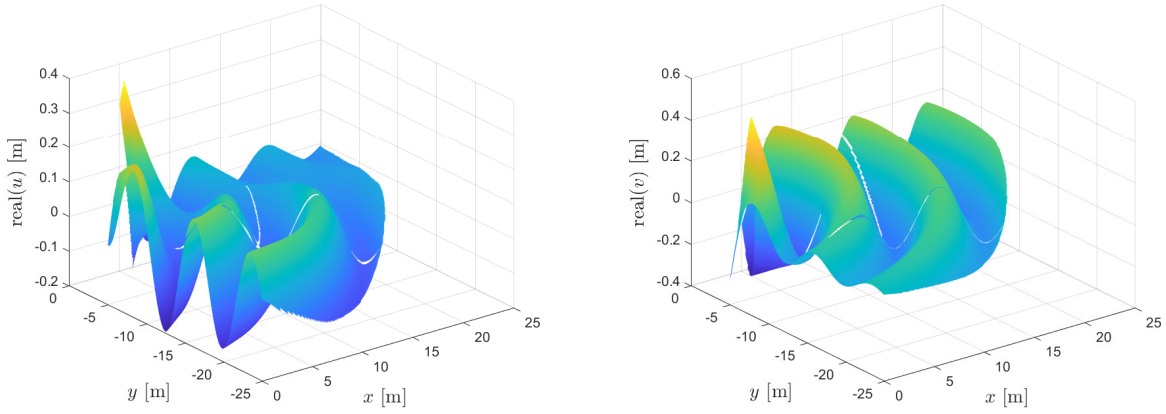

(a) Displacement component u **(b)** Displacement component v

Figure 7.9: Example 1: Approximated displacement shapes, s-wave case, 4 elements, $N = 10$, $M = 4$

From the briefly summarized results for the individual meshes and cases, certain trend regarding the required number of terms included in both domain displacement and boundary traction bases can be observed. For increasing number of elements, the individual bases need to have less terms to achieve similar accuracy as was obtained with the coarser mesh. This is an expected behaviour, since the approximated fields evaluated in smaller domains tend to have less oscillations and therefore

smaller number of basis functions is necessary for their sufficient approximation. On the other hand, the total number of degrees of freedom required for a certain accuracy is larger for the finer meshes. This motivates to model the analysed domain using only few elements but bases with many terms. However, a drawback of such approach are the numerical difficulties which result in badly conditioned system of equations. The reason for such behaviour is that high order Bessel functions tend to get flatter in the vicinity of origin. Therefore, the domain approximation basis $\boldsymbol{U}$ evaluated at the given location contains values which are due to limited computer precision regarded as zero. A possible remedy could be the introduction of the scaling of the individual Bessel functions. This way it could be ensured that the basis functions of all orders have similar maximum amplitudes within the element domain. However, as this approach was not implemented in the code, for some cases it is necessary to include more elements in the mesh to decrease the error caused by high condition number of the global system matrix.

In all the provided plots the approximated measure E_{FE} tends to converge to a certain value, when the boundary traction basis order M is fixed and the number of terms contained in the domain basis is increased. However, as was already discussed, for the finite traction approximation order M there exists a mismatch between the converged value and the analytically evaluated one. A nice visualization of such convergence process can be obtained by plotting the inter-element tractions. These can be derived directly from the stress field associated to the displacement solution. Note that since the inter-element edge is shared by two elements, two variants of the common tractions exist. Moreover, as the inter-element tractions are independently approximated based on eq. (3.36), also such representation of the tractions is available. In fig. 7.10 the normal tractions evaluated at the inter-element edge are plotted for the case the domain is discretized using two finite elements. The tractions are evaluated for the s-wave case, the boundary basis order $M = 9$ is chosen and the domain approximation basis order is increased from $N = 10$ to $N = 16$ with step of two orders. The associated convergence plot can be found in fig. 7.5b, where it is represented by the red line. In fig. 7.10 the individual lines correspond to tractions evaluated from the obtained displacement solution for both adjacent elements, to the approximated boundary tractions and to the analytical solution. Radius r is plotted on the x-axis.

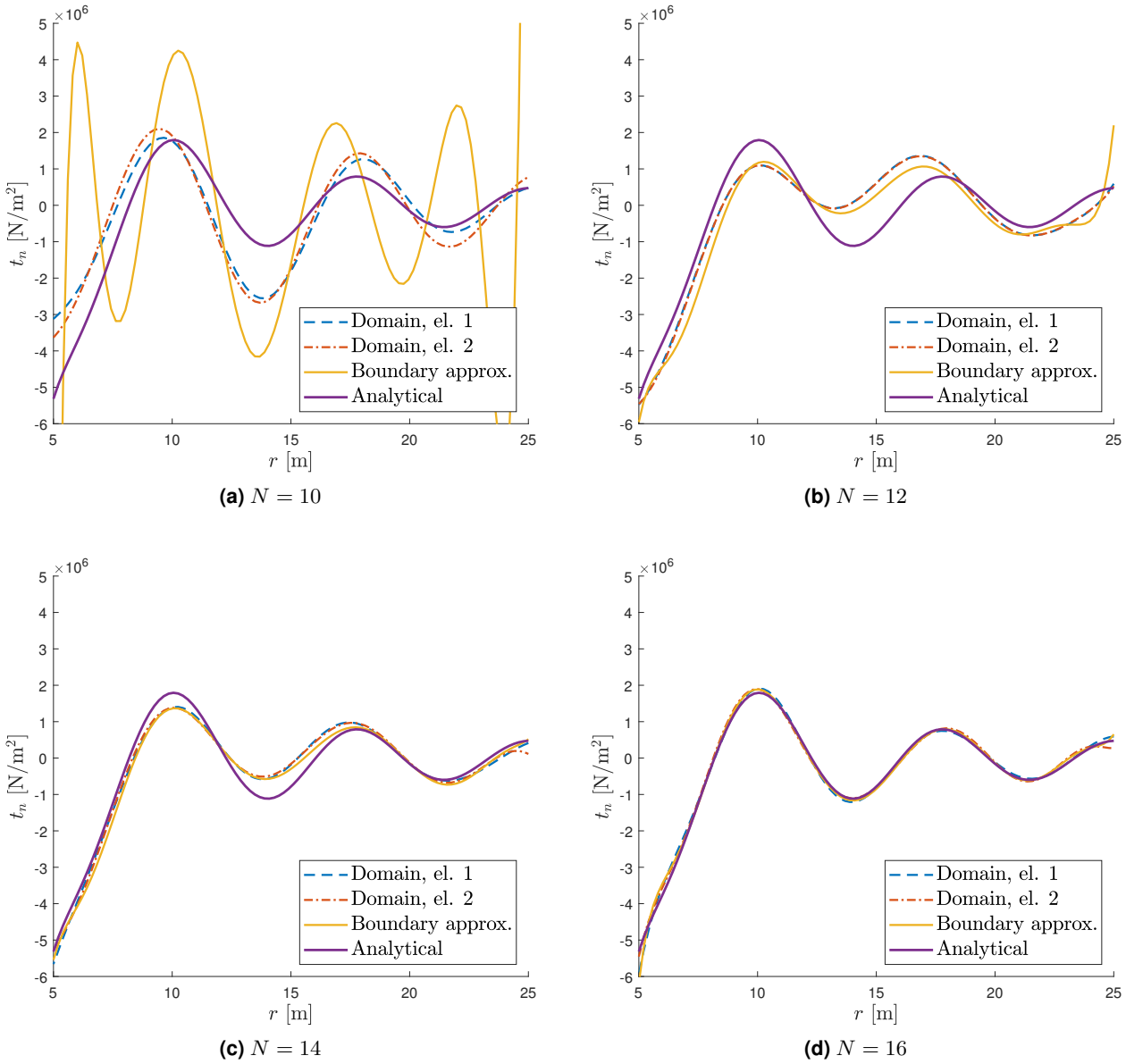

(a) $N = 10$ **(b)** $N = 12$

(c) $N = 14$ **(d)** $N = 16$

Figure 7.10: Example 1: Inter-element normal tractions for varying order N, s-wave case, 2 elements, $M = 9$

From fig. 7.10a it is apparent that there is a significant deviation between the tractions obtained from the displacement solution and the ones evaluated from the boundary approximation. In addition, non-negligible mismatch can be spotted between the tractions associated to the approximated solution and the analytical ones. From figures 7.10b and 7.10c one can see that for increasing order N of the domain displacement basis the tractions computed from the boundary approximation and those related to the obtained displacement solution tend to be more similar to each other and closer to the analytically evaluated ones. In fig. 7.10d all the representations are in a good agreement, which indicates the associated orders M and N are sufficient.

The situation, when the maximum order M is not sufficiently high to capture the behaviour of the real boundary tractions, can be observed for the two-element mesh case for order $M = 7$. In fig. 7.5b the related convergence plot is visualized with blue color. For order $N = 21$, which

corresponds to $n_{DOF} = 188$, the resulting solution seems to be already converged. The normal tractions evaluated on the inter-element boundary are depicted in fig. 7.11.

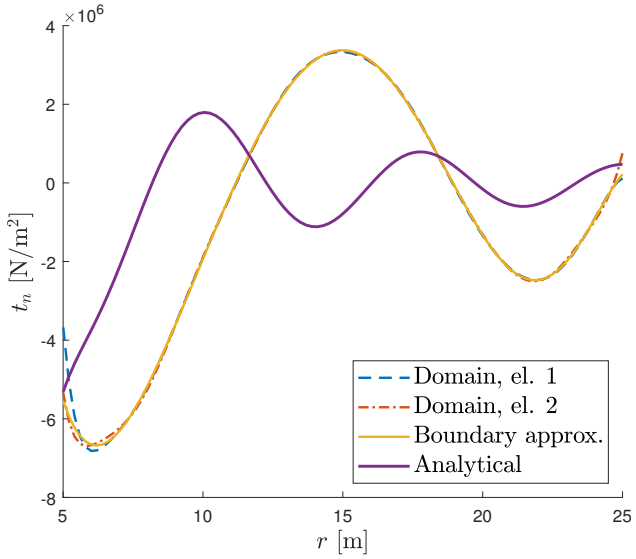

Figure 7.11: Example 1: Inter-element normal tractions, s-wave case, 2 elements, $M = 7$, $N = 21$

One can see that the lines representing tractions derived from the displacement solution and those obtained from the traction approximation have very similar shapes. This implies that for the given boundary basis order M, the domain basis order N is sufficient. However, from fig. 7.11 it is obvious that these shapes are remarkably different from the true solution. Further increase of order N would not solve this issue. In such situation it is necessary to enlarge the boundary basis order so that the true tractions can be approximated more accurately.

7.3 Example 2: Absorbing Boundary Condition Validation

In this example the implemented absorbing boundary condition approach is validated.

The aim of the absorbing boundary condition technique is to approximate the solution in an infinite domain by analysing only a finite region. The domain is truncated at certain distance from the origin of excitation and the absorbing boundary condition is applied on the associated boundary. The investigated domain for this test case is very similar to the one analysed in Example 1, only the outer radius r_1 tends to infinity. Moreover, at the radius r_a from the origin the absorbing boundary is placed. The scheme of such structure is depicted in fig. 7.12. The specific values of the radii are $r_0 = 5\,\mathrm{m}$ and $r_a = 25\,\mathrm{m}$.

As was discussed in section 4.2.1, when the Hankel function is used as the function W for the generation of the displacement basis, the resulting solution also satisfies the Sommerfeld radiation condition. Therefore, the displacement basis functions considered as the analytical solution in Example 1 are not only solutions of the governing differential equation but as well fulfil the radiation condition in infinity. Therefore, they are also considered as the reference solution for this test case.

The procedure of obtaining the approximated solution is similar to the one adopted in Example

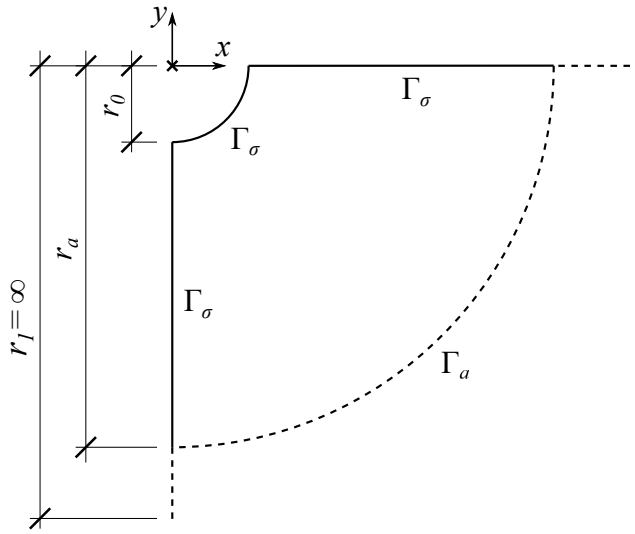

Figure 7.12: Example 2: Domain scheme

1. From the analytical solution, which is the same for both examples, the tractions on the outer boundary are derived and applied as the loading to the numerical model. However, in this test case, the Neumann boundary does not include the edge, at which the infinite domain is truncated. This one is considered as the absorbing boundary and the absorbing boundary condition is enforced there. In fig. 7.12 the Neumann edges, where the traction boundary condition is applied, are denoted by Γ_σ and the absorbing boundary is marked by symbol Γ_a. In the case the absorbing boundary is located sufficiently far from origin, the approximated displacement shapes should be similar to the analytical solutions plotted in figures 7.2 and 7.3.

The quantity E is again chosen as the measure for comparison of the approximated and analytical solutions. Its reference value can be evaluated using eq. (7.9). The aim is to compare both solution shapes within the interior domain, therefore the upper limit for the integration in eq. (7.9) is now replaced by r_a. The finite element approximation E_{FE} is obtained using eq. (7.16).

The considered material properties and the loading frequency are identical to those used in Example 1 and are listed in tab. 7.1. The simulations are again performed for single-element, two-element and four-element meshes, which are depicted in fig. 7.1b. The Bessel function of the first kind is used for the construction of the domain basis and local reference frame located at the element center is chosen for the evaluation of the system matrices. Also in this example the number of integration points is set to $q = 250$.

For each of the p-wave and s-wave test cases and each mesh, simulations for various dimensions of the domain displacement and boundary traction bases are performed. The number of total degrees of freedom serves as the measure of complexity of the resulting system of equations and can be calculated as

$$n_{DOF} = 2n_{el}(2N + 1) + 2(n_D + n_a)(M + 1), \tag{7.18}$$

where n_a denotes the overall number of absorbing edges in the finite element system. Note that when

absorbing boundary condition is applied, the boundary tractions are additionally approximated on the related absorbing edges. Therefore the related degrees of freedom need to be included in the formula. In the single-element mesh, there is one absorbing edge and for both two- and four-element meshes, two absorbing edges appear in the system.

In figures 7.13, 7.14 and 7.15 the convergence plots for all the considered meshes and for both p-wave and s-wave cases are presented. The individual lines denote results for the fixed maximum order M of the polynomial included in the boundary traction basis while the order N of the domain basis is increased. For each combination of orders N and M the number of degrees of freedom is calculated and plotted on the x-axis.

The considered orders N and M are the same as for the cases in Example 1. As the boundary approximation needs to be applied also in the case of the single-element mesh in this example, multiple lines for orders $M = 4$, 6, 8 can be spotted in fig. 7.13.

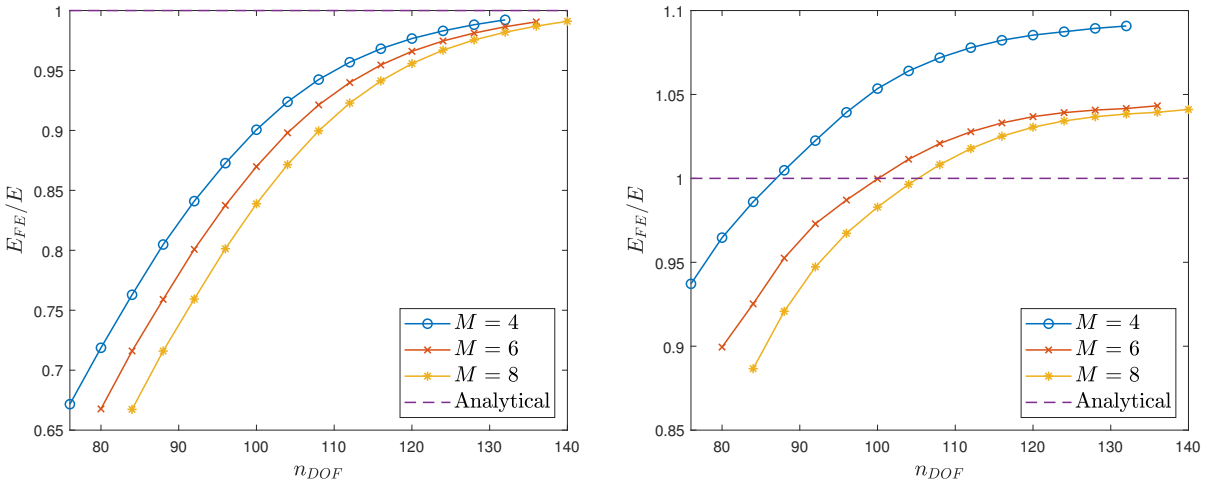

(a) P-wave case **(b)** S-wave case

Figure 7.13: Comparison to the analytical solution, unbounded domain, 1 element

From the provided results, one can note that for the p-wave case, the approximated quantity E_{FE} tends to converge to value which is very close to the analytically evaluated one, this holds for all the investigated meshes and all the considered orders M. The plots 7.14a and 7.15a are very similar to their finite counterparts presented in Example 1. One can note that in fig. 7.13a the lines for all orders are almost the same. This indicates that the tractions evaluated at the absorbing boundary might be sufficiently approximated also by the polynomial of lower order than those considered. Based on the given results one can conclude that for the p-wave case the selected distance r_a, where the infinite domain is cut, is adequately large.

In the case of s-wave solution, the approximated results tend to converge to value which is 3.7% larger than the analytically evaluated one. Such behaviour can be seen for all the meshes and for most of the considered orders M. Only for the single-element mesh the order $M = 4$ and for the two-element mesh the order $M = 7$ are insufficient to capture the behaviour of the approximated boundary tractions. The reason for such overestimation are the spurious reflections, which occur due to the imposition of the absorbing boundary condition in the finite distance from the origin.

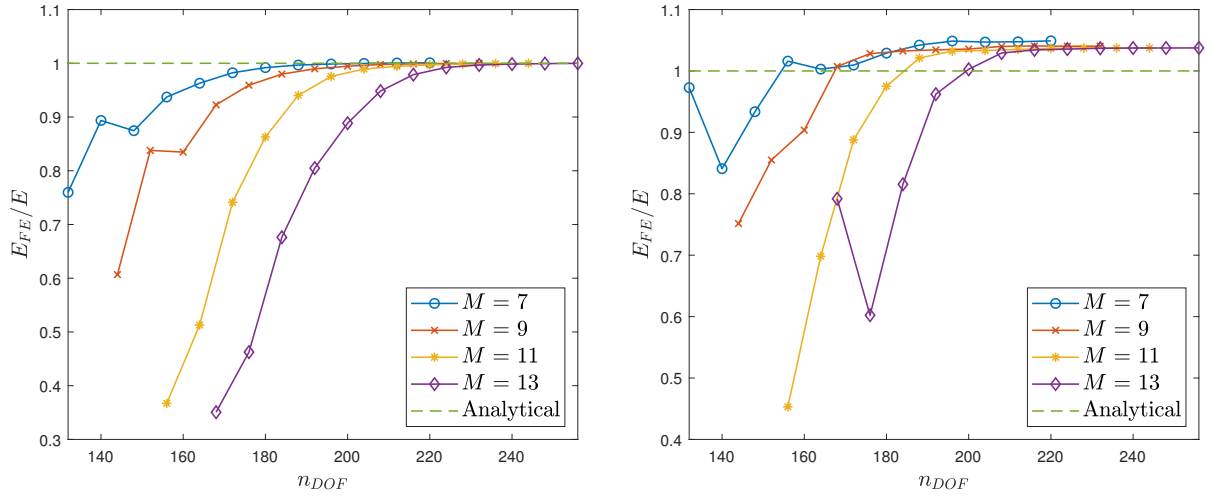

(a) P-wave case **(b)** S-wave case

Figure 7.14: Comparison to the analytical solution, unbounded domain, 2 elements

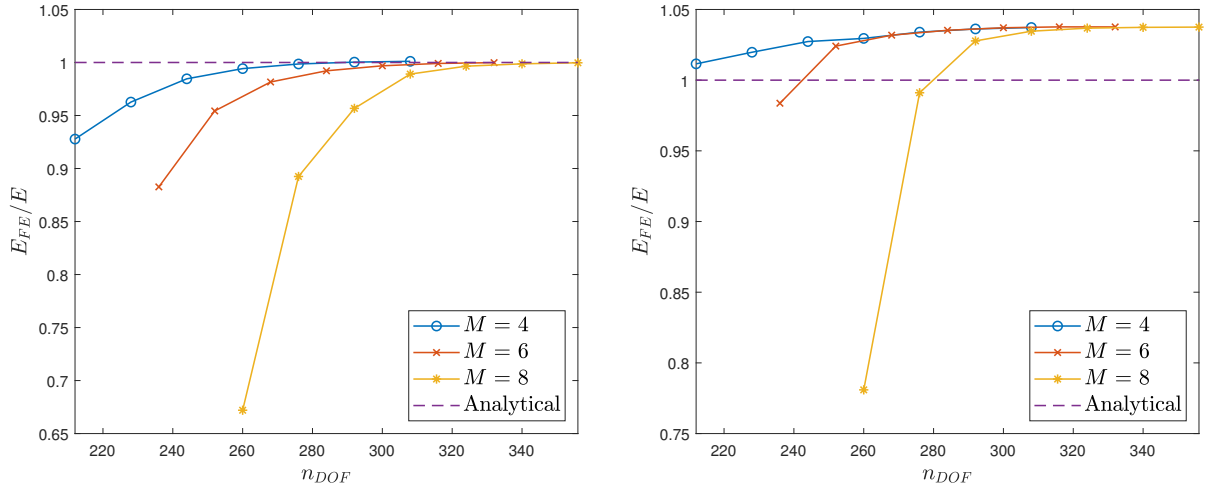

(a) P-wave case **(b)** S-wave case

Figure 7.15: Comparison to the analytical solution, unbounded domain, 4 elements

Recall that the enforced relation (4.36) between the displacements and tractions only holds when evaluated in infinity. When imposed in finite distances, it results in an approximation. The resulting error depends on the characteristics of the target solution. As the s-wave displacement shape is more oscillatory compared to the p-wave one, truncation of the domain at the same distance r_a yields more severe errors.

The effect of varying distance r_a, at which the absorbing boundary is placed, on the resulting energy is studied next. The four-element mesh is chosen and computations for domains with various distances r_a are performed. The number of terms included in the domain displacement and boundary traction bases is chosen such that the the convergence is reached and further increase in orders N and M has negligible impact on the approximated solution. The outcome of the simulations is depicted in fig. 7.16.

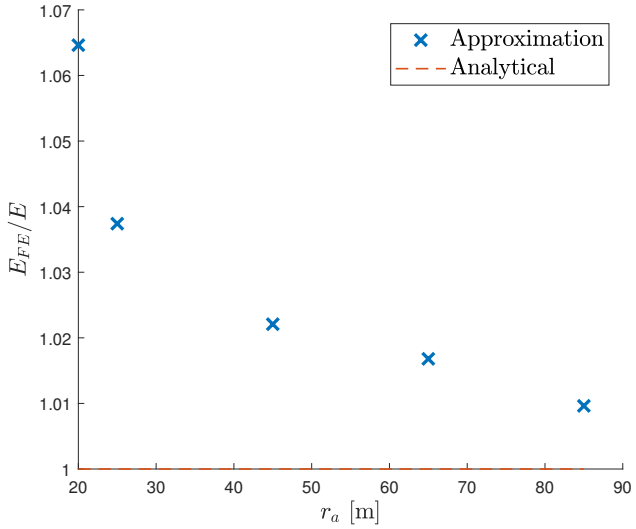

Figure 7.16: Effect of the distance r_a on the approximated solution of Example 2

One can clearly see that as the distance of the absorbing boundary from the origin is increased, the difference between the analytical and approximated solutions is diminished. Such results are in agreement with the expected behaviour.

7.4 Example 3: Comparison to Wave Based Method

In the previous two examples the results obtained using the hybrid-Trefftz method were compared to the known analytical solutions. In both of the cases the approximated solutions were in a good agreement with the reference one. In this section a more realistic test case is analysed, which is an infinite half-space loaded by a distributed load q. The scheme of the domain is visualized in fig. 7.17, where also the dimensions are stated. One can note that in certain distance from origin the infinite space is truncated and the absorbing boundary is introduced.

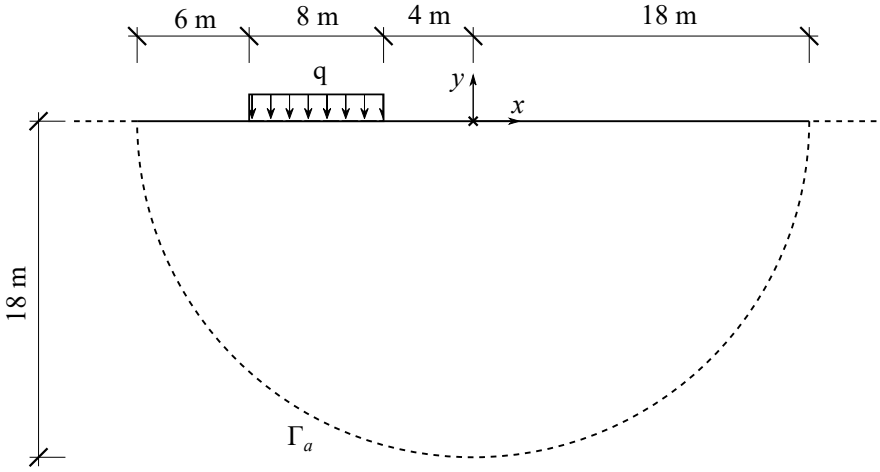

Figure 7.17: Example 3: Domain scheme

In this example also the damping of the structure is considered, the loss factor η together with

other material and loading parameters are listed in tab. 7.3.

$\tilde{E}$ [N/m^2]	ν	ρ [kg/m^3]	f [Hz]	q [N/m^2]	η
26000000	0.3	2000	30	1	0.1

Table 7.3: Material properties, Example 3

Firstly, a number of simulations for various orders of the approximation bases is performed and the convergence of the results towards a stationary value is checked. Both maximum orders N and M are increased until the resulting value E_{FE} stabilizes, such procedure enables to estimate the required number of terms, which need to be considered in the approximation bases. The approximated displacement shapes associated to the converged values are then compared to the results obtained with the wave based method. The already existing MATLAB program, developed at the Chair of Structural Mechanics at Technical University of Munich, was provided for the WBM simulations.

7.4.1 Hybrid-Trefftz Method Results

For the analysis using the implemented hybrid-Trefftz method, the domain is discretized into ten finite elements. The mesh is visualized in fig. 7.18.

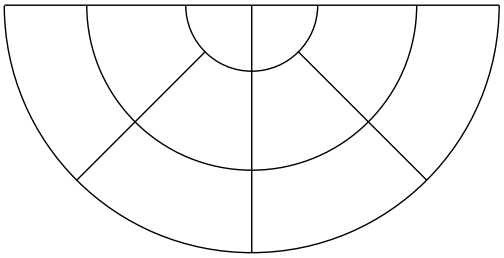

Figure 7.18: Hybrid-Treffz method mesh for Example 3

For the assessment of the required number of terms, which need to be included in the approximation bases, simulations for orders $N = 24, 26, \ldots, 42$ and $M = 13, 15, \ldots, 21$ were performed. The resulting approximated quantity E_{FE} related to each combination of N and M is visualized in fig. 7.19. The individual lines correspond to the fixed order M of the boundary traction basis while the order N of the domain displacement basis is increased and plotted on the x-axis. Due to inclusion of the damping of the structure, the approximated comparison quantity E_{FE} is complex value, hence the plots for both real and imaginary parts are depicted in figs. 7.19a and 7.19b.

From the shown convergence plots the following statements can be deduced. Firstly, one can note that the imaginary part varies only marginally for almost all the considered orders M and N. For orders $M = 15, 17, 19, 21$ the converged value is almost identical. From the plots for the real part of E_{FE}, it can be seen that for high order N the difference between the evaluated lines for all the considered orders M is only marginal. Hence one can assume that even polynomial of maximum order $M = 13$ is able to approximate the boundary tractions sufficiently well. Moreover, as the convergence rate is higher for the boundary basis of the lower maximum order, accurate results

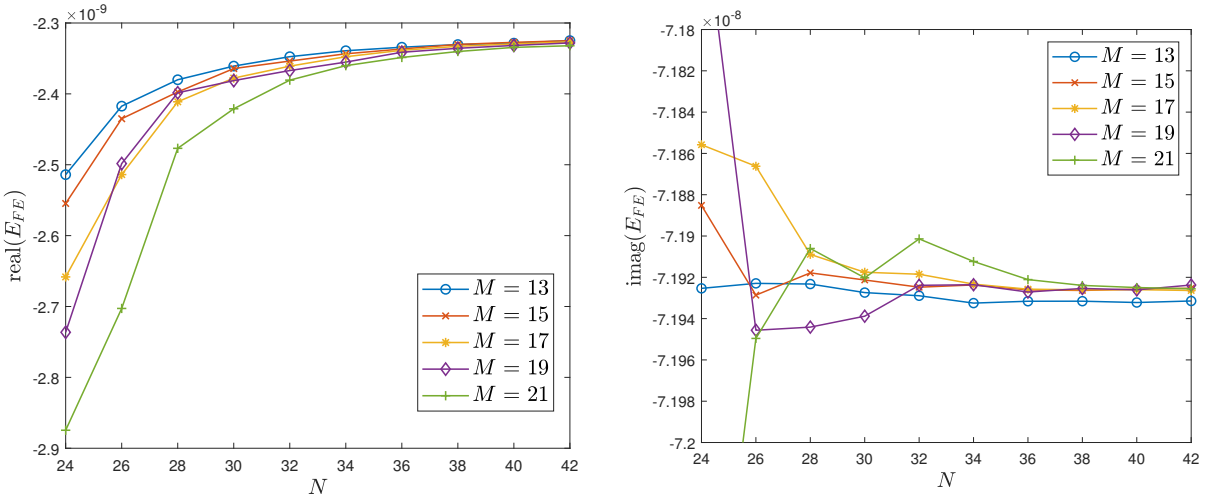

(a) Real part

(b) Imaginary part

Figure 7.19: Example 3: Convergence of E_{FE}, 10 elements

can be obtained also already for smaller number of terms included in the domain approximation basis. Therefore, it can be concluded that for the highest considered orders, which are $M = 21$ and $N = 42$, the most accurate results are obtained. However, in comparison with results for orders $M = 13$ and $N = 36$ the benefit of the additional number of degrees of freedom is minor. Therefore, the latter orders are assumed to produce sufficiently accurate results and are considered for the further assessment. The associated number of degrees of freedom is computed using formula (7.18), where the number of Dirichlet edges is $n_D = 15$ and number of absorbing edges is $n_a = 4$. Therefore, the resulting number of degrees of freedom in the system is 1992. A significant reduction of the unknowns in the system could be achieved by discretizing the domain with smaller number of elements. However, without incorporation of further scaling procedures, the system of equation gets ill-conditioned and the quality of the results for coarser mesh is compromised.

The approximated displacement shapes are depicted in fig. 7.20. In fig. 7.20b, where the v displacement component is visualized, clear wave pattern travelling in the y-direction can be spotted. Similar displacement shape could be expected from the given loading, therefore the approximated solution seems to be plausible.

7.4.2 Wave Based Method Results

As was already mentioned, to validate the results of Example 3, the solution obtained using the implemented hybrid-Trefftz method is compared with the one acquired with the wave based method. To model the wave propagation in the infinite domain, coupling with integral transform method is introduced. Therefore, the infinite half-space sketched in fig. 7.17 is divided into the external and internal regions, the separating boundary coincides with the absorbing boundary Γ_a. In the internal region, wave based method is used to simulate the wave propagation, while in the external part the integral transform method is applied. Subsequently, coupling at the circular boundary (denoted by Γ_a) is enforced. A short introduction into the wave based method modelling together

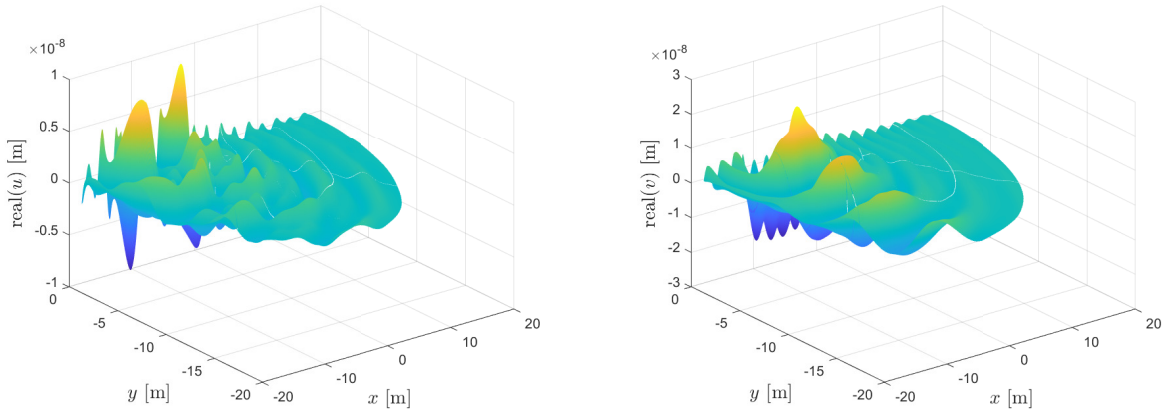

(a) Displacement component u **(b)** Displacement component v

Figure 7.20: Example 3: Approximated displacement shapes obtained with hybrid-Trefftz method

with the comparison of both WBM and hybrid-Trefftz method is provided in chapter 5. As was mentioned previously, an already existing code is provided for the WBM analysis.

The internal region is discretized into three finite elements, the resulting mesh is depicted in fig. 7.21. As this test case was taken from the model examples provided with the WBM code, the simulation parameters are assumed to be tuned so that the results are sufficiently accurate. The overall number of degrees of freedom associated to the coupled system of equations is 3324. For the numerical integration along the boundary edges 102 quadrature points were used.

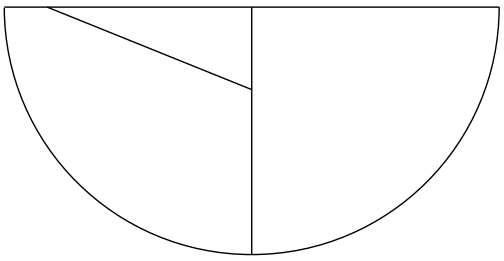

Figure 7.21: WBM mesh for Example 3

The resulting displacement shapes are shown in fig. 7.22. From the visual comparison with the solution acquired with the hybrid-Trefftz method, which is depicted in fig. 7.20, strong similarity can be noticed. Further analysis of the error between both approximations is described in the next section.

7.4.3 Results Comparison

In this section the difference between the displacement fields obtained with both methods is studied. Firstly, to get an idea about the similarity of the approximations, the results are displayed in the same figure. To make the graphs more illustrative and clear, the displacement fields are evaluated at various vertical sections and plotted afterwards. The x-coordinates x_s of the evaluation sections are chosen as $x_s = -7, -10, -13, -16$ m. In fig. 7.23 the real part of the v displacement component

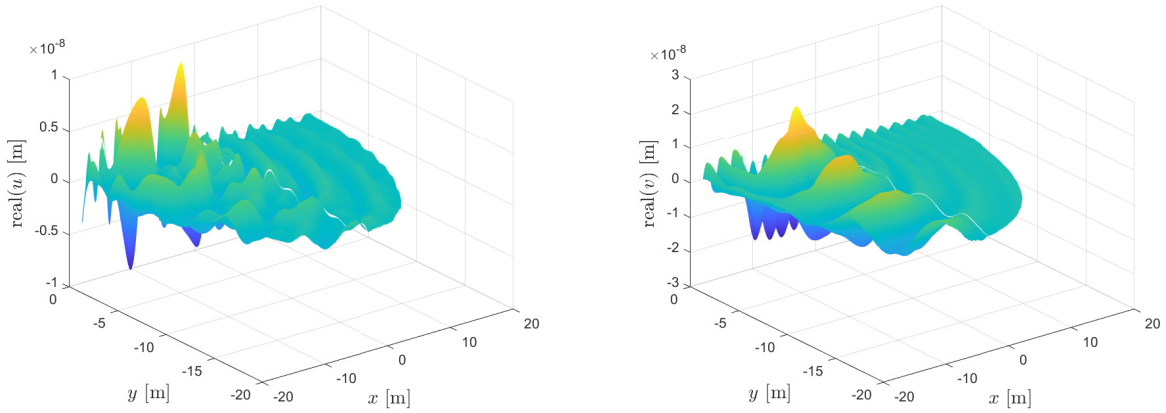

(a) Displacement component u **(b)** Displacement component v

Figure 7.22: Example 3: Approximated displacement shapes obtained with wave based method

associated to both WBM and hybrid-Trefftz method (HT) is visualized for each investigated section. The y-coordinate of the evaluated point at the vertical line is plotted on the x-axis.

It can be seen that for the sections located at $x_s = -7$ m and $x_s = -10$ m the vertical displacement components v evaluated using both methods are almost identical. A notable mismatch can be spotted for the sections located further from the loading and closer to the left boundary. Nevertheless, also for $x_s = -13$ m and $x_s = -16$ m both methods produce similar results.

In fig. 7.24 the horizontal displacement component u evaluated at the same vertical sections is visualized. Also for this case both approximations are in a very good agreement, larger deviations can be noted only at the very left section with $x_s = -16$ m.

As for the practical cases the displacements at the surface are perhaps the most important outcome, also these are presented. In fig. 7.25 both components evaluated at the horizontal line located at $y_s = 0$ m are depicted. As can be seen, also at the surface the approximated displacement fields look alike, non negligible deferences are apparent in the vicinity of the left absorbing boundary.

The so far discussed results served mainly for the qualitative assessment of the solutions obtained using both methods. In the following, the mismatch between the displacement shapes is computed for the whole surface and visualized in fig. 7.26. The absolute error measure is chosen and is computed as the difference between real parts of the displacement component evaluated using hybrid-Trefftz method and the one computed with WBM. Hence it is expressed as

$$\begin{aligned} \mathrm{Err}(u) &= \mathrm{real}(u_{HT} - u_{WBM}), \\ \mathrm{Err}(v) &= \mathrm{real}(v_{HT} - v_{WBM}), \end{aligned} \tag{7.19}$$

where $u_{HT}(x,y)$, $v_{HT}(x,y)$ and $u_{WBM}(x,y)$, $v_{WBM}(x,y)$ denote the displacement components evaluated using hybrid-Trefftz method and wave based method.

The already stated conclusions regarding the error distribution can be deduced also from fig. 7.26. The largest deviations occur near the left side of the absorbing boundary, which is located

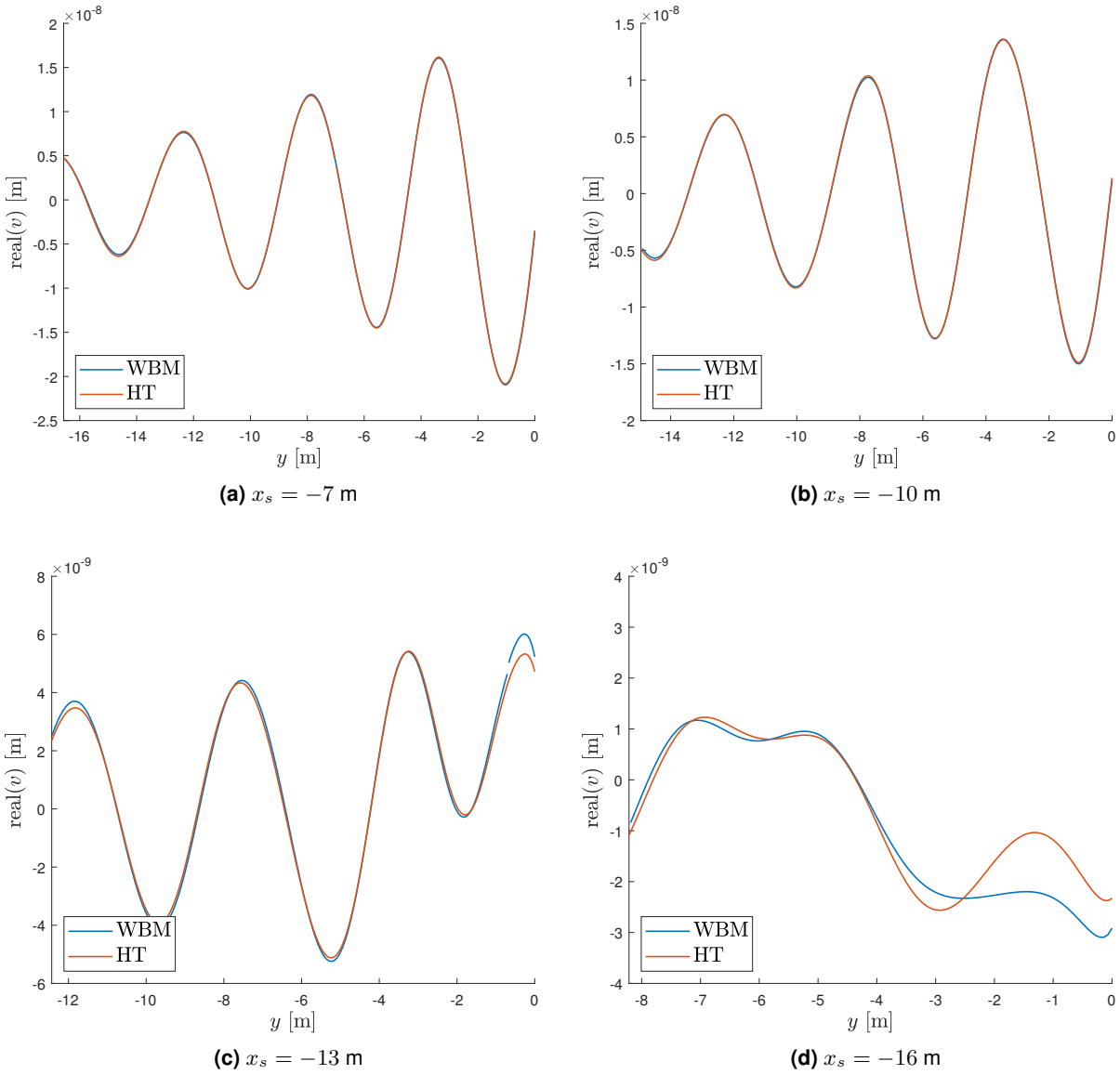

(a) $x_s = -7$ m **(b)** $x_s = -10$ m

(c) $x_s = -13$ m **(d)** $x_s = -16$ m

Figure 7.23: Example 3: Comparison of the vertical displacement component v evaluated at various vertical sections

close to the source of excitation. Possible reason for this mismatch might be the insufficient distance between the position of the absorbing boundary and the loading, which may cause spurious wave reflections. The potential remedy could be to increase the radius at which the absorbing boundary is located and hence diminish the resulting deviations. However, one has to be aware that in this example the results are not compared to the true analytical solution, but to the different numerical approximation. Therefore, the mismatch between both displacement shapes does not imply that one of the methods produce such error, but rather that the error of both approximations combined together generates the mentioned deviations.

The average error for each displacement component, which is calculated as the mean of absolute value of $\mathrm{Err}(u)$ or $\mathrm{Err}(v)$, is evaluated in tab. 7.4. Furthermore, the maximum of the absolute value of the individual displacement components evaluated using WBM is also stated and the ratio of the

average error and the maximum displacement is computed. As can be seen, for both components

$\tilde{f}$	mean(abs(Err($\tilde{f}$))) [m]	max(abs($\tilde{f}_{WBM}$)) [m]	mean(abs(Err($\tilde{f}$)))/max(abs($\tilde{f}_{WBM}$))
u	8.6972 e-11	9.3159 e-09	0.0093
v	8.3992 e-11	2.1047 e-08	0.0040

Table 7.4: Example 3: Error evaluation

the average difference between the results obtained with individual methods is less than 1% of the maximum displacement.

Overall, it can be concluded that both approximated solutions are in a good agreement. The number of total unknowns in the system for the considered simulation parameters is significantly larger in the case of the wave based method. However, no basis refinement study was performed for the WBM results, perhaps similar accuracy could be achieved even for lower number of degrees of freedom. Therefore, no conclusions regarding the comparison of the computational efficiency of both methods are stated.

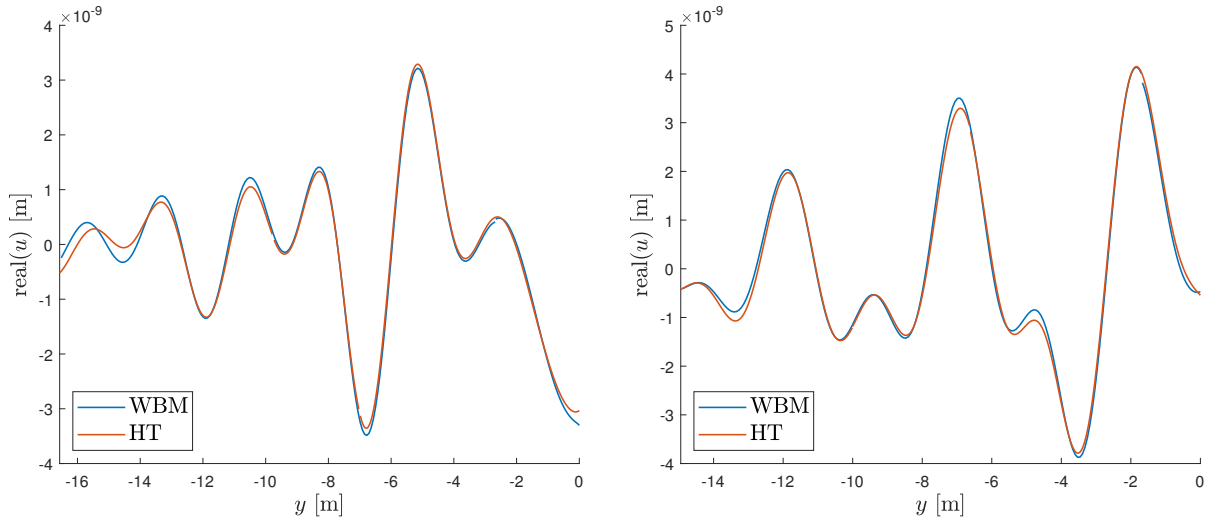

(a) $x_s = -7$ m **(b)** $x_s = -10$ m

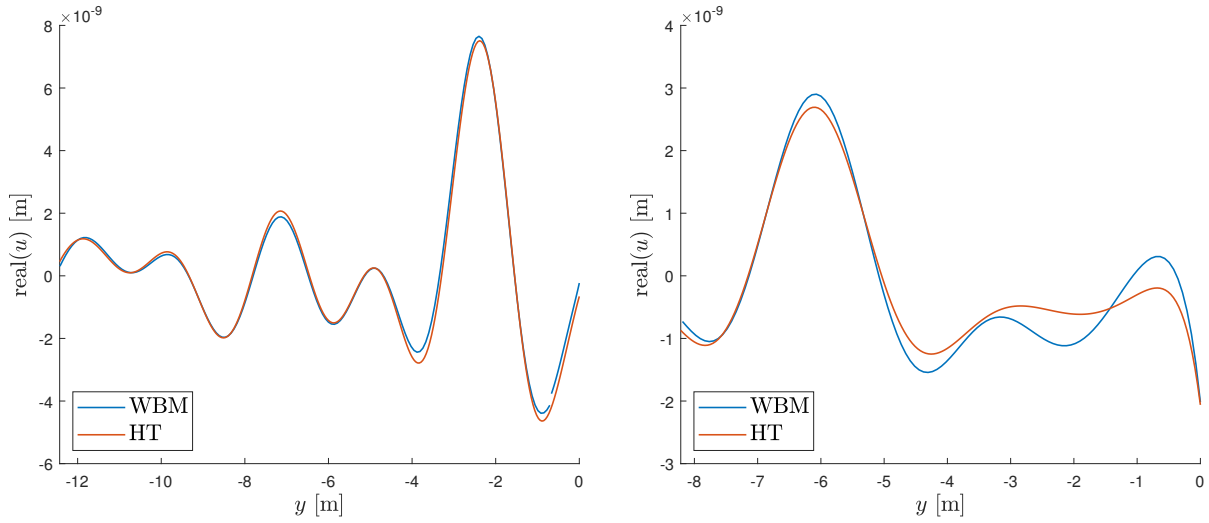

(c) $x_s = -13$ m **(d)** $x_s = -16$ m

Figure 7.24: Example 3: Comparison of the horizontal displacement component u evaluated at various vertical sections

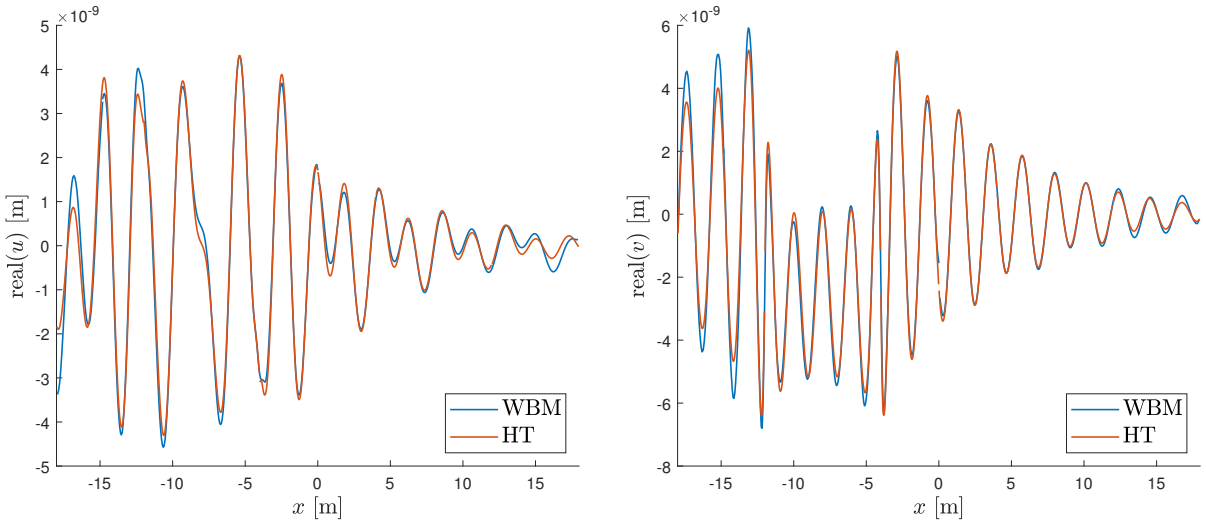

(a) Displacement component u **(b)** Displacement component v

Figure 7.25: Example 3: Comparison of the displacement components evaluated at the surface

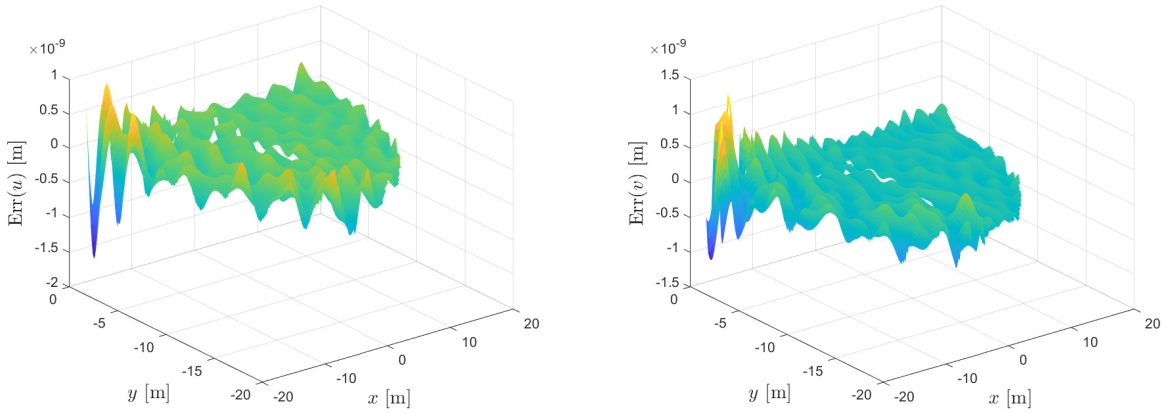

(a) Error in displacement component u **(b)** Error in displacement component v

Figure 7.26: Example 3: Error between hybrid-Trefftz and wave based method results

8 Conclusion

In the thesis the hybrid-Trefftz method is applied as the numerical technique for approximation of the solution of the spectral form of Lamé equation. The distinctive feature of the method is the special choice of the shape functions, which are used for approximation of the displacement field inside the element domain. The basis functions are chosen as the solutions of the governing differential equation. Therefore, due to the fact that the approximation functions reflect the mechanical features of the modelled phenomenon, the domain can be discretized into only a few elements. In addition, the number of required elements is independent of the excitation frequency, which makes the method applicable even for higher frequencies.

To obtain more accurate results, the number of terms included in the domain basis is increased instead of refining the element mesh. Such p-refinement technique proves to produce equation systems with a relatively low number of degrees of freedom compared to conventional methods. Even local singularities can be modelled without mesh refinement by including special singular functions in the approximation basis. Moreover, the resulting system matrices appearing in the final system of equations are constructed by integration along the element boundary instead along the element domain as is common in e.g. FEM. As a consequence, elements of arbitrary shape and number of edges may be used for the analysis. In addition, numerical error arising due to mesh distortion is practically avoided.

What distinguishes the hybrid-Trefftz approach from other subclasses of the Trefftz family is the way how the boundary conditions and the inter-element continuity conditions are enforced. For this purpose, the boundary tractions are additionally approximated at the element boundary. Compared to e.g. wave based method, for which the inter-element and boundary conditions are directly weakly imposed without introduction of additional degrees of freedom, such approach results in certain benefits as well as disadvantages. The obvious drawback is the additional number of degrees of freedom and hence a larger resulting system of equations for the same number of domain basis functions. On the other hand, the element convexity requirement is completely relaxed, which makes the method applicable even for more complex domains.

From the obtained results it can be concluded that the quality of the approximated solution is determined by the number of basis functions included in both the domain displacement as well as in the boundary traction basis. Moreover, the required number boundary approximation functions strongly depends on the character of the target solution. The maximum order of the polynomial contained in the boundary traction basis needs to be high enough so that the shape of the true inter-element and boundary traction fields is well captured. If this condition is not fulfilled, even for increasing number of terms contained in the domain displacement basis the approximated displacement solution does not converge to the true one but rather to a different

artificial displacement shape. The theoretical convergence to the analytical solution is only reached when the number of terms contained in both bases tends to infinity.

Even though the efficiency of the method lies in coarse discretization with elements containing a large number of basis functions, for certain cases this approach yields non-converging results. The reason is that for large elements both domain and boundary bases need to contain many terms so that the fields are approximated accurately. As the high order Bessel functions of the first kind tend to get flatter near the origin, some components of the evaluated displacement basis are close to zero. As a consequence of the limited computer precision, the final system of equations turns out to be badly conditioned and therefore producing non-negligible numerical error. Such issue may be overcome by applying a mesh refinement strategy in order to decrease the number of required basis functions. Alternatively, scaling of the individual functions based on the dimensions of the element might improve the numerical stability.

The absorbing boundary condition strategy adopted for modelling of infinite domains implicitly results in an approximation, when enforced at finite distance from the source of excitation. The required distance for generation of acceptably accurate results depends on the dissipative nature of the true displacement shape. The advantage of the absorbing boundary condition approach lies in the non-restricted choice of the displacement basis functions, which may be constructed from any of the mentioned solutions of the Bessel equation. When e.g. infinite elements are used for analysis of unbounded media, the related approximation functions need to implicitly satisfy the radiation condition and hence their choice is limited.

Based on the comparison of the results with analytical solutions for both bounded and unbounded domains, the implemented code is considered to be validated. The results are also in a good agreement with those obtained with the wave based method, which was shown for the example of a loaded half-space. From the analysis of the error between the approximations acquired using both methods, it may be observed that the largest deviations occur near the absorbing boundary located in the closest distance to the loading. Such outcome implies that perhaps the radius at which the absorbing boundary is placed should be enlarged, in order to decrease the mismatch between both solutions.

Regarding the possibilities of future extensions of the implemented code, there are many potential generalizations which may be introduced. A simple and straightforward modification might be implementation of elements with an arbitrary number of edges, which would enable a user to model more complex domains without the need of mesh refinement. The second idea for generalization is to incorporate non-linear material models, since the so far included material law has only limited applicability. Another possible direction for the future work is the introduction of coupling of the method to other structural systems, such as Euler-Bernoulli beam. Such extension would enable to model e.g. wave propagation in the soil under a loaded foundation of a building more accurately. This idea could be generalized to coupling of the method with the finite element method. This way the parts of the structure with complex geometry could be analysed using FEM, while the hybrid-Trefftz method could be applied in large interior regions.

Overall, the hybrid-Trefftz method represents an efficient solution procedure of various engineering problems and offers some significant advantages compared to other deterministic approaches.

Nevertheless, one has to be aware of the limitations of its application, since for domains of complex shapes the preferable efficiency is compromised.

Bibliography

[Arfken et al 2013a] Arfken, George B. ; Weber, Hans J. ; Harris, Frank E.: Chapter 14 - Bessel Functions. In: Arfken, George B. (Editor.) ; Weber, Hans J. (Editor.) ; Harris, Frank E. (Editor.): *Mathematical Methods for Physicists (Seventh Edition)*. Seventh Edition. Boston : Academic Press, 2013, p. 643–713. – URL https://www.sciencedirect.com/science/article/pii/B9780123846549000141. – ISBN 978-0-12-384654-9

[Arfken et al 2013b] Arfken, George B. ; Weber, Hans J. ; Harris, Frank E.: Chapter 18 - More Special Functions. In: Arfken, George B. (Editor.) ; Weber, Hans J. (Editor.) ; Harris, Frank E. (Editor.): *Mathematical Methods for Physicists (Seventh Edition)*. Seventh Edition. Boston : Academic Press, 2013, p. 871–933. – URL https://www.sciencedirect.com/science/article/pii/B9780123846549000189. – ISBN 978-0-12-384654-9

[Arfken et al 2013c] Arfken, George B. ; Weber, Hans J. ; Harris, Frank E.: Chapter 3 - Vector Analysis. In: Arfken, George B. (Editor.) ; Weber, Hans J. (Editor.) ; Harris, Frank E. (Editor.): *Mathematical Methods for Physicists (Seventh Edition)*. Seventh Edition. Boston : Academic Press, 2013, p. 123–203. – URL https://www.sciencedirect.com/science/article/pii/B9780123846549000037. – ISBN 978-0-12-384654-9

[Arfken et al 2013d] Arfken, George B. ; Weber, Hans J. ; Harris, Frank E.: Chapter 9 - Partial Differential Equations. In: Arfken, George B. (Editor.) ; Weber, Hans J. (Editor.) ; Harris, Frank E. (Editor.): *Mathematical Methods for Physicists (Seventh Edition)*. Seventh Edition. Boston : Academic Press, 2013, p. 401–445. – URL https://www.sciencedirect.com/science/article/pii/B9780123846549000098. – ISBN 978-0-12-384654-9

[Bauchau and Craig 2009] Bauchau, Olivier A. ; Craig, James I.: *Structural analysis: with applications to aerospace structures*. Volume 163. Springer Science & Business Media, 2009

[Cismaşiu 2000] Cismaşiu, C.: *The hybrid-Trefftz Displacement Element for Static and Dynamic Structural Analysis Problems*, Universidade Técnica de Lisboa, Ph.D. thesis, 2000

[Cismaşiu and Freitast 1998] Cismaşiu, C. ; Freitast, J. A. T.: Hybrid-Trefftz finite element formulation for spectral elastodynamic analysis. In: *2nd Int. PhD Symposium in Civil Engineering. Budapest* Citeseer (Veranst.), 1998

[Clough and Penzien 2003] Clough, R. W. ; Penzien, J.: *Dynamics of structures*. Computers & Structures, Inc., 2003

[Deckers et al 2012] Deckers, Elke ; Hörlin, Nils-Erik ; Vandepitte, Dirk ; Desmet, Wim: A Wave Based Method for the efficient solution of the 2D poroelastic Biot equations. In: *Computer Methods in Applied Mechanics and Engineering* 201 (2012), p. 245–262

[Freitas 1997] Freitas, J. A. T.: Hybrid-Trefftz displacement and stress elements for elastodynamic analysis in the frequency domain. In: *Computer Assisted Mechanics and Engineering Sciences* 4 (1997), p. 345–368

[Freitas and Cismaşiu 2003] Freitas, J. A. T. ; Cismaşiu, C.: Hybrid-Trefftz displacement element for spectral analysis of bounded and unbounded media. In: *International journal of solids and structures* 40 (2003), Nr. 3, p. 671–699

[Golub and Welsch 1969] Golub, Gene H. ; Welsch, John H.: Calculation of Gauss quadrature rules. In: *Mathematics of computation* 23 (1969), Nr. 106, p. 221–230

[Gonzalez and Stuart 2008] Gonzalez, Oscar ; Stuart, Andrew M.: *A first course in continuum mechanics*. Cambridge University Press, 2008

[Gourgeon and Herrera 1981] Gourgeon, Hervé ; Herrera, Ismael: Boundary methods. C-complete systems for the biharmonic equations. In: *Boundary element methods*. Springer, 1981, p. 431–441

[Herrera 1980] Herrera, Ismael: Boundary methods: a criterion for completeness. In: *Proceedings of the National Academy of Sciences* 77 (1980), Nr. 8, p. 4395–4398

[Herrera and Gourgeon 1982] Herrera, Ismael ; Gourgeon, Hervé: Boundary methods, C-complete systems for Stokes problems. In: *Computer Methods in Applied Mechanics and Engineering* 30 (1982), Nr. 2, p. 225–241

[Jirousek 1978] Jirousek, Jaroslav: Basis for development of large finite elements locally satisfying all field equations. In: *Computer Methods in Applied Mechanics and Engineering* 14 (1978), Nr. 1, p. 65–92

[Keller and Givoli 1989] Keller, Joseph B. ; Givoli, Dan: Exact non-reflecting boundary conditions. In: *Journal of computational physics* 82 (1989), Nr. 1, p. 172–192

[Malvern 1969] Malvern, L.E.: *Introduction to the Mechanics of Continuous Medium*. Prentice-Hall, 1969

[Meyers and Chawla 2008] Meyers, Marc A. ; Chawla, Krishan K.: *Mechanical behavior of materials*. Cambridge university press, 2008

[Moldovan 2008] Moldovan, Ionut: *Hybrid-Trefftz Finite Elements for Elastodynamic Analysis of Saturated Porous Media*, Universidade Técnica de Lisboa, Ph.D. thesis, 2008

[Moldovan and Freitas 2006] Moldovan, Ionut ; Freitas, J. A. T.: Hybrid-Trefftz finite element models for bounded and unbounded elastodynamic problems. In: *Proceedings of Third European Conference on Computational Mechanics, Lisbon, Portugal. Springer*, 2006

[Poruchikov 2012] Poruchikov, Vladimir B.: *Methods of the classical theory of elastodynamics*. Springer Science & Business Media, 2012

[Qin 2005] Qin, Qing-Hua: Trefftz Finite Element Method and Its Applications. In: *ASME. Appl. Mech. Rev.* 58 (2005), p. 316–337

[Qin and Wang 2008] Qin, Qing-Hua ; Wang, Hui: *MATLAB and C Programming for Trefftz Finite Element Methods*. Taylor & Francis, 2008

[Serov et al 2017] Serov, Valery et al: *Fourier series, Fourier transform and their applications to mathematical physics*. Volume 197. Springer, 2017

[Sommerfeld 1912] Sommerfeld, Arnold: Die Greensche funktion der schwingungsgleichung. In: *J.-Ber. Deutsch Math.-Verein* 21 (1912), p. 309–353

[Sze and Cheung 2008] Sze, K. Y. ; Cheung, Y. K.: A hybrid-Trefftz finite element model for Helmholtz problem. In: *Communications in Numerical Methods in Engineering* 24 (2008), p. 2047–2060

[Sze et al 2010] Sze, K.Y. ; Liu, G.H. ; Fan, H.: Four- and eight-node hybrid-Trefftz quadrilateral finite element models for helmholtz problem. In: *Computer Methods in Applied Mechanics and Engineering* 199 (2010), p. 598–614

[Trefftz 1926] Trefftz, Erich: Ein gegenstuck zum ritzschen verfahren. In: *Proc. 2nd Int. Cong. Appl. Mech. Zurich*, 1926, p. 131–137

[Tsynkov 1998] Tsynkov, Semyon V.: Numerical solution of problems on unbounded domains. A review. In: *Applied Numerical Mathematics* 27 (1998), Nr. 4, p. 465–532

[Van Genechten et al 2010] Van Genechten, Bert ; Vergote, Karel ; Vandepitte, Dirk ; Desmet, Wim: A multi-level wave based numerical modelling framework for the steady-state dynamic analysis of bounded Helmholtz problems with multiple inclusions. In: *Computer Methods in Applied Mechanics and Engineering* 199 (2010), Nr. 29-32, p. 1881–1905